UNIVERSITÀ DI PARMA

UNIVERSITÀ DEGLI STUDI DI PARMA

Corso di Dottorato in

Scienze del Farmaco

Ciclo XXXV

Free-energy simulations applied to melatonin receptor ligands

Coordinatore

Chiar.mo Prof. Marco Mor

Tutor

Chiar.ma Prof.ssa Silvia Rivara

Dottorando

Gian Marco Elisi

Anni Accademici 2019/2020 – 2021/2022

Summary

Chapter 1. Introduction

1.1 AIM OF THE WORK AND STRUCTURE OF THE THESIS

The present work reports molecular modelling investigation performed for melatonergic ligands, aimed at the design of new compounds, definition of structure-activity relationships and investigation of the mechanism of action.

Some aspects of the binding mode of melatonergic ligands are studied for the first time exploiting three-dimensional structures of the two melatonin receptors, which were released just before the beginning of the Thesis. While providing a new starting point for structure-based drug design, experimental structures are representative of free-energy minima which are rarely escaped within unbiased molecular dynamics simulations. However, configurations far from these minima could hide important information for design of compounds of pharmaceutical interest. Therefore, free-energy differences must be assessed by either observing the probability of an alternative state to spontaneously occur in longer unbiased simulations or by introducing an external bias potential permitting the system to access new configurations in a shorter simulation time. A basic theoretical overview of such approaches, i.e., free-energy calculations, performed in the Thesis is provided in Chapter 3. While some events, such as most of the studies on ligand conformational space in Chapter 5, can spontaneously occur in unbiased molecular dynamics, most of the simulations require sampling of hidden degrees of freedom of the system, which are not immediately unveiled by crystal structures. Indeed, some states are inherently not observable in such experimental structures, remarking the importance of complex free-energy simulations in the context of drug discovery pipelines in lieu of routinary and simpler docking calculations, still useful to rationalize main structure-activity relationships. These techniques, while requiring more expensive calculations and an increasing complexity, are usually employed in projects of pharmaceutical interest beyond the hit discovery phase, when potent ligands and a richer occurrence of structure-activity relationships are available.

In the Thesis, multiple aspects of melatonergic ligands activity have been investigated, including: *i)* the unbinding route from the ligand binding site, *ii)* the conformational space of the ligands in bound and unbound states, *iii)* molecular determinants leading to MT_2 receptor subtype selectivity, *iv)* the impact of the ligand binding on the free-energy landscape of receptor activation. These aspects were analysed in the context of medicinal chemistry projects, in which molecular modelling simulations were performed to rationalize the structure-activity relationships of melatonergic ligands, additionally providing insights for the design of novel compounds.

A general introduction to melatonin receptors, with a particular focus on the most important classes of melatonergic ligands, is provided in the Chapter 2, introducing the medicinal chemistry framework in which this work is inserted.

In Chapter 4, simulations supporting the hypothesis that melatonergic ligands are recruited through a lipophilic pathway passing through TM helices IV and V are presented and discussed. The free-energy profile associated with the unbinding route of 2-iodomelatonin from the MT_1 receptor was characterized and a molecular determinant rationalizing a faster dissociation of the ligand from the MT_1 receptor is proposed. Additionally, simulations are commented in combination with experimental data provided by radioligand binding assays and mutagenesis experiments.

The impact of conformational equilibria on the binding of melatonergic ligands is extensively analysed in Chapter 5. In particular, the abundance of the bioactive conformation of chiral ligands in the solvent was related to the measure of stereoselectivity for different melatonergic ligands. This approach is generalizable to different classes of ligands, comprising both simplified derivatives of the indole ring and analogues, such as tetrahydroquinolines, in which the alkylamide chain is partially constrained into a ring, dramatically increasing the binding affinity.

In Chapter 6, different elements were considered regarding the ligand selectivity toward the MT_2 receptor subtype, for the optimization of two important classes of melatonergic ligands: 2-aryl substituted indole derivatives and N-anilinoethylamides. Such properties comprise the study of the size and the orientation of 2-aryl substituents of the indole scaffold for the optimal occupation of an aromatic subpocket, as well as the introduction on both scaffolds of more hydrophilic groups, enhancing the water solubility, while preserving the high binding affinity and selectivity toward the MT_2 receptor.

Finally, in Chapter 7, molecular determinants driving receptor activation are studied through metadynamics simulations of the MT_2 receptor in complex with a prototypical agonist or antagonist. While providing limited information, this study permitted an approximate dissection of structural motifs, scattered across the TM bundle, called *microswitches*, which are involved in structural changes related to receptor activation and inactivation.

1.2 PRODUCTS OF THE THESIS

The results discussed in the thesis have been reported in the following publications, according to the approximate order in which they are discussed:

1. **Elisi, G. M.**; Scalvini, L.; Lodola, A.; Mor, M.; Rivara, S. Free-energy simulations support a lipophilic binding route for melatonin receptors. *J. Chem. Inf. Model.* **2022**, 62, 1, 210-22.

2. **Elisi, G. M.**;† Bedini, A.;† Scalvini, L.; Carmi, C.; Bartolucci, S.; Lucini, V.; Scaglione, F.; Mor, M.; Rivara, S.; Spadoni, G. Chiral recognition of flexible melatonin receptor ligands induced by conformational equilibria. *Molecules*. **2020**, 4, 25, 4057.

3. Mari, M.;† **Elisi, G. M.**;† Bedini, A.; Lucarini, S.; Retini, M.; Lucini, V.; Scaglione, F.; Vincenzi, F.; Varani, K.; Castelli, R.; Mor, M.; Rivara, S.; Spadoni, G. Melatonin analogues probing the 2-phenyl-binding pocket reveal tolerance to hydrophilic groups. *Eur. J. Med. Chem.* **2022**, 243, 14762.

4. Ferlenghi, F.; Mari. M.; Gobbi, G.; **Elisi, G. M.**; Mor, M.; Rivara, S.; Vacondio, F.; Bartolucci, S.; Bedini, A.; Fanini, F.; Spadoni, G. "*N*-(anilinoethyl)amide melatonergic ligands with improved water solubility and metabolic stability" *ChemMedChem*. **2021**, 16, 19, 3071.

† Authors equally contributed.

A part of the theoretical background for *in silico* design and development of melatonergic ligands was reviewed in ref. 5.

5. **Elisi, G. M.**; Scalvini, L.; Lodola, A.; Bedini, A.; Spadoni, G.; Rivara, S. "In silico drug discovery of melatonin receptor ligands with therapeutic potential" *Expert Opin. Drug Discov.* **2022**, 17, 343-54.

The results reported in the text have also been object to the following oral communications:

1. "Molecular requirements driving subtype selectivity of melatonergic ligands", MYCS2022 - Rimini, November 21-23, **2022**.

2. "Free-energy simulations on melatonin receptors ligands", EUROPIN Application Retreat (EUROPIN Vienna Summer School on Drug Design), September 17, **2021**.

3. "Molecular dynamics characterization of a lipophilic pathway for the unbinding of melatonin receptors ligands", Nuove Prospettive in Chimica Farmaceutica (NPCF13) - Divisione di Chimica Farmaceutica della Società Chimica Italiana, April 27, **2021**.

LIST OF ABBREVIATIONS

4-P-PDOT	*N*-(4-phenyl-1,2,3,4-tetrahydronaphthalen-2-yl)propanamide
5-HEAT	(*N*-(2-(5-(2-hydroxyethoxy)-1*H*-indol-3-yl)ethyl)acetamide
AA-NAT	N-acetyltransferase [arylalkylamine N-acetyltransferase]
ABMD	Adiabatic-bias molecular dynamics
AFMK	N_1-acetyl-N_2-formyl-5-methoxykynuramine
AMK	N_1-acetyl-5-methoxykynuramine
cAMP/PKA	3',5'-cyclic adenosine monophosphate/protein kinase A (signalling pathway)
CHO	Chinese hamster ovary (cells)
CNS	Central Nervous System
COM	centre of mass
CoMFA	Comparative molecular field analysis
CV	Collective variable
ECL1/2/3	First/second/third extracellular loop
FAAH	Fatty acid amide hydrolase
FES	free-energy surface
GAFF	generalized AMBER force field
GCMC	Grand Canonical Monte Carlo (simulations)
GPCRs	G-protein coupled receptors
ICL1/2/3	First/second/third cellular loop
IUPHAR	International Union of Basic and Clinical Pharmacology
LINCS	LINear Constraint Solver (algorithm)
MEK/ERK	Mitogen-activated protein kinases - EC signal-regulated kinase (signalling pathway)
MD	Molecular dynamics (simulations)
MetaD	Metadynamics (simulations)
MLT	Melatonin
MM-GBSA	Molecular mechanics with generalised Born and surface area solvation
NEB	nudged elastic band (method)
NIH3T3	A type of mouse embryonic fibroblast cells
NOE	Nuclear Overhauser Effect
(N)REM	(Non-)Rapid Eye Movement
OPLS	Optimized Potentials for Liquid Simulations
PCVs	Path collective variables
PCV-SMD	Path-like Collective Variables-Steered Molecular Dynamics

PCV-US	Path-like Collective Variables-Umbrella Sampling
PDB	Protein Data Bank
PMF	Potential of Mean Force
POPC	1-palmitoyl-2-oleoyl-*sn*-phosphatidylcholine
QM-MM	quantum mechanics/molecular mechanics (simulations)
RMSD	Root Mean Square Deviation
RMSF	Root Mean Square Fluctuation
RESP	Restrained Electrostatic Potential-Derived (charges)
RESPA	reversible reference system propagator algorithms
ROS	reactive oxygen species
RT-PCR	Reverse transcription polymerase chain reaction
SMD	Steered Molecular Dynamics (simulations)
TI	Thermodynamic Integration (simulations)
TM	trans-membrane
UCM	Urbino Chimica Medicinale
US	Umbrella Sampling (simulations)
VSGB	Variable Dielectric Surface Generalized Born
WHAM	weighted histogram analysis method
wt-MetaD	Well-tempered Metadynamics (simulations)

Chapter 2. Melatonergic system and ligands

2.1 MELATONIN: BIOSYNTHESIS AND PHYSIOLOGICAL ROLE

Melatonin (5-methoxy-*N*-acetyltryptamine, Figure 1) is a tryptophan-derived neurohormone primarily secreted by pinealocytes, that are the main endocrine cells found in the pineal gland. [6] These cells receive signals from the suprachiasmatic nucleus of the hypothalamus to entrain circadian rhythms of the vertebrates to the daily and seasonal light-dark cycles. [7] Here, melatonin is produced at night starting from the neurotransmitter serotonin, obtained from *L*-tryptophan, which is in turn absorbed from the blood by pinealocytes; through acetylation of the ammino group and methylation of the 5-hydroxyl (Figure 1), melatonin is produced, resulting in a lipophilic substance able to easily cross through biological membranes. [8,9] Melatonin is also produced in other peripheral tissues, which include the retina, the gastrointestinal tract, the lymphocytes and different types of skin cells, [6] As well as in pinealocytes, a circadian clock seems responsible for the regulation of melatonin biosynthesis in retina, [10] while in other tissues melatonin production is not regulated by the light-dark cycle.

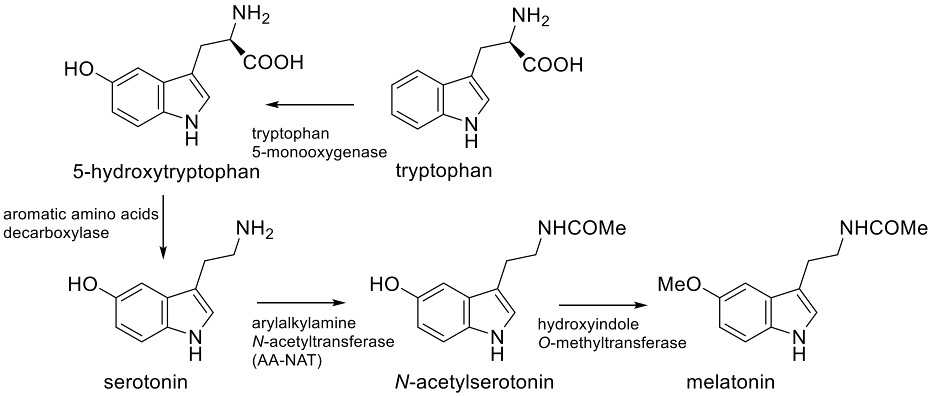

Figure 1. Melatonin biosynthetic pathway in pinealocytes.

Melatonin is a ubiquitous molecule, found in all living kingdoms, and it is believed that its original function was related to the action as a free radical scavenger. [11] In 1917, McCord and Allen reported that a substance extracted from bovine pineal glands was able to blanch the skin of tadpoles. [12] Later, in 1958, dermatologist A Lerner was the first scientist, to isolate melatonin, describing its skin-lightening effect as a consequence of the aggregation of pigment granule in dermal melanophore cells, [13] and was able to characterize the structure of the previously unknown compound in the following year. [14]

In the 1970s, Lynch et al. discovered that melatonin concentration follows daily rhythms by measuring the endogenous levels of neurohormone in the pineal gland [15] and observing concentration in rat urines periodically changing depending on the time of the day [16]. The effect on circadian rhythms due to melatonin is mostly mediated by negative feedback onto the suprachiasmatic nucleus, upon activation by light inputs (blue light, around 480 nm in the electromagnetic spectrum). Signals eventually reach the superior cervical ganglia through sympathetic neurons, inhibiting adrenaline release, which in turn leads to intracellular increase of cAMP/PKA-mediated serotonin N-acetyltransferase [arylalkylamine N-acetyltransferase] (AA-NAT, Figure 1) protein expression and activating phosphorylation [17,18,19]. Being the enzymatic conversion catalysed by AA-NAT the rate-limiting step to melatonin biosynthesis, the cascade prompts the release of the neurohormone by pinealocytes.

Circulating melatonin is primarily metabolized in the liver through 6-hydroxylation and subsequent sulphate conjugation, leading to increased water solubility (Figure 2). [20] For this reason, C6 halogenation is a strategy extensively utilised to increase the otherwise short half-life (~30 min). [21] Secondarily, demethylation of the methoxy group leads to *N*-acetylserotonin. Instead, extra-hepatic metabolism would be responsible for melatonin deacylation.

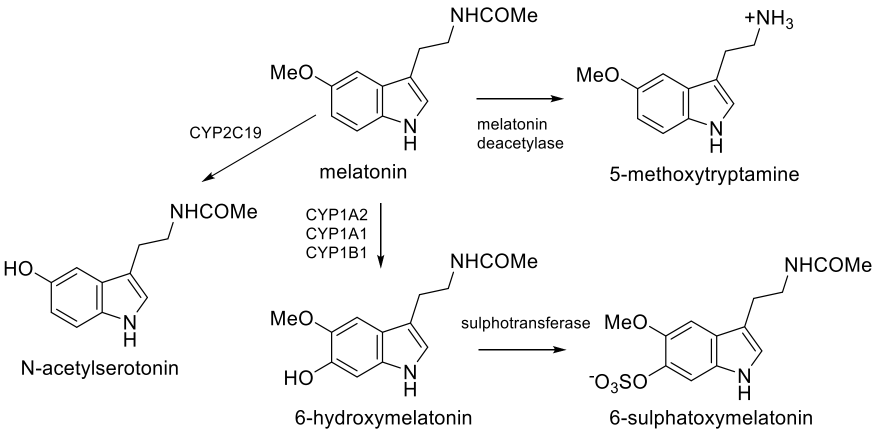

Figure 2. Melatonin catabolic pathway.

Melatonin activates melatonin receptors MT_1 and MT_2, GPCRs diffused in the central nervous system and in several peripheral tissues, [22,23] including different districts [24] with therapeutic importance.

The effect of melatonin on circadian rhythms is mostly mediated by feedback onto the suprachiasmatic nucleus, where melatonin activates MT_1 and MT_2 receptors. [17] As well, activation of the two receptor subtypes leads to different physiological outcomes, depending on the anatomical district at which the receptors are expressed.

Therefore, the role of melatonin receptors is not only limited to the entrainment of sleep/wake cycles, but extends to a variety of other physiological functions, comprising pressure regulation, immune system modulation, glucose homeostasis, bone remodelling and protection against cancer and neurodegenerative disorders. [23] However, melatonin is considered a pleiotropic substance for a manyfold of other activities evidenced in *in vitro* and *in vivo* experiments. For example, antioxidant and free radical scavenger properties of melatonin are extensively reported in the literature and are dependent on the indole ring reactivity with Fenton reactive species and through pyrrole oxidative ring cleavage (Figure 3). [25] In the brain, the cleavage leads to the formation of N_1-acetyl-N_2-formyl-5-methoxykynuramine (AFMK), which is then deformylated to N_1-acetyl-5-methoxykynuramine (AMK). [25] Melatonin antioxidant activity is usually observed at concentrations higher than those needed to activate its principal macromolecular targets. Radical quenching catabolites, including cyclic 3-hydroxymelatonin [26] and AMK, are then excreted through urine. [27]

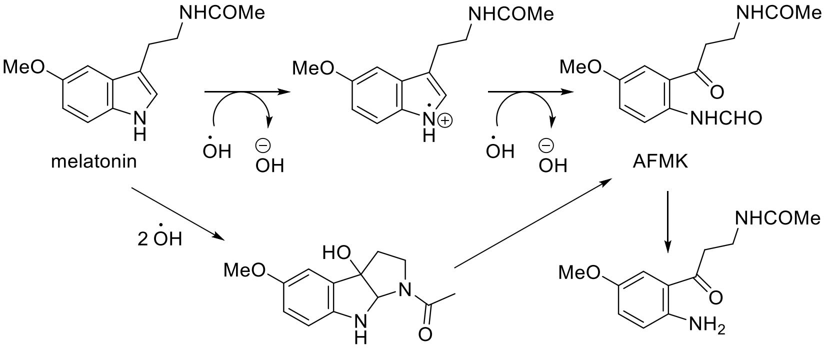

Figure 3. Melatonin antioxidant mechanism.

In humans, several targets (Figure 4) [28] are engaged by melatonin other than the mentioned GPCRs receptors, including low-affinity binding to the enzyme quinone oxidoreductase 2, the so-called MT_3 receptor, [29] in which melatonin appears co-crystalized in multiple orientations, [30] without possibly producing any apparent antioxidative effect. At nanomolar concentrations, melatonin can additionally bind calcium-binding proteins in the cytoplasm, such as calmodulin and calreticulin. [28]

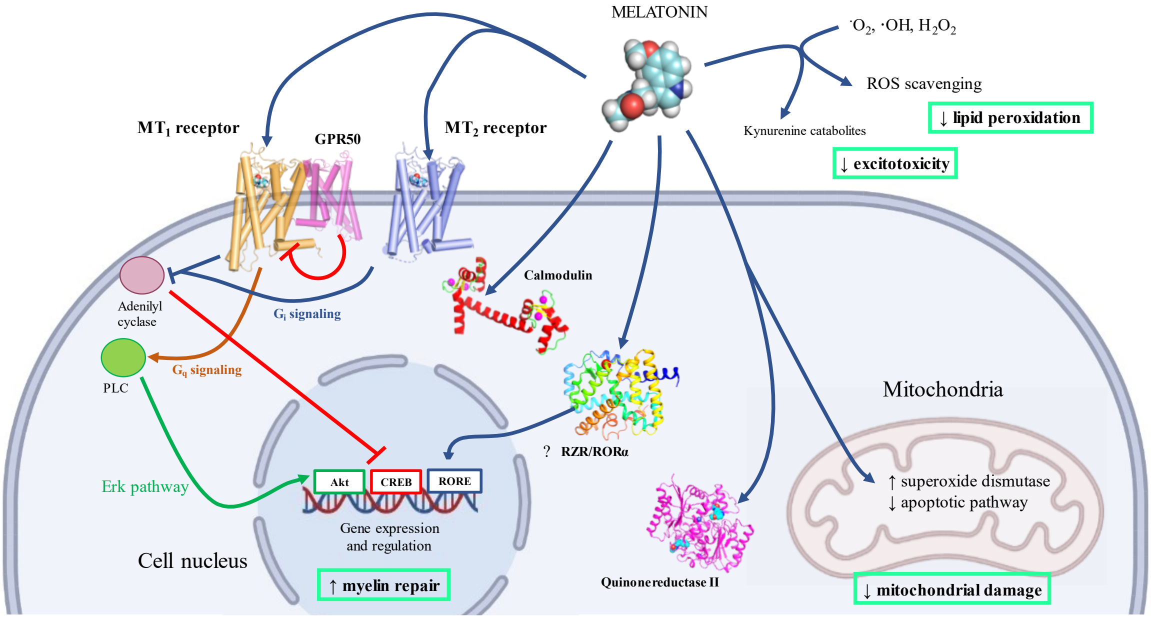

Figure 4. Melatonin pleiotropic activity in human cells: biological targets and gene expression and regulations involved in neuroprotection. Melatonin targets two GPCRs, MT_1 and MT_2, in turn activating G_i signalling and decreasing cAMP concentration in the cytoplasm. The MT_1 receptor also couples to G_q signalling, and subsequent increase of calcium ion concentration. [31] MT_1 and GPR50 receptor heterodimerization hampers signalling pathway elicited upon MT_1 receptor activation. [32] Melatonin binds calmodulin in the cytoplasm and quinone reductase II (also known as MT_3 receptor). [28] In the mitochondria, melatonin inhibits cytochrome C release and apoptosis initiation. [33] Controversial is the binding to the nuclear receptor RORα and the resulting gene expression regulation due to receptor translocation. [28] Melatonin can also act as antioxidant and scavenger for reactive oxygen species (ROS), additionally producing metabolites of the kynurenine pathway, [26] eliciting neuroprotective effects.

2.2 MELATONIN MEMBRANE RECEPTORS AND THEIR THERAPEUTIC ROLE

As previously mentioned, melatonin receptors are a family of GPCRs belonging to class A (i.e, the rhodopsin superfamily), [34,35] comprising in humans two receptor subtypes, MT_1 and MT_2, sharing a high sequence similarity, while evolutionarily distancing from other class A families. The nearest neighbour in the class A phylogenetic tree is the orphan receptor GPR50, which is reported as a regulatory melatonin coreceptor inhibiting the MT_1 receptor, when establishing heterodimeric complexes (Figure 4). [32] Besides the complex between the MT_1 and GPR50 receptors, other heterodimeric complexes have been reported between the MT_2 receptor and the MT_1 receptor, and with the serotonin receptor 5-HT2c and other orphan receptors, such as GPR61, GPR62 and GPR135. [36]

Melanophores represented the initial step in research on melatonin receptors, since from their study it was possible to obtain the first cloning of high-affinity melatonin receptor binding sites by isolating the corresponding cDNA from a dermal *X. laevis* melanophore library. [37] Three high affinity GPCRs were cloned during the following years, comprising MT_1 [38] and MT_2 receptors expressed in humans and other mammals in the mid-1990s. [39,40] The third receptor, originally cloned from melanophores, is an additional subtype, termed Mel1c receptor, expressed in amphibia, birds and in the platypus. [37] Seminal works initially elucidating SARs studies of melatonin and congeneric compounds relied on melanophore-based binding affinity assays. [41] Cloning of the two receptors with molecular biology techniques, including RT-PCR and *in situ* hybridization, permitted the expression in different human tissues, comprising both brain cell lines and peripheral tissues. [31] Then, MT_1 [42] and MT_2 [43] knock-out mice permitted the study of the physiological role of each of the two receptors. This was additionally possible through the identification of potent and selective MT_2 antagonists used as pharmacological tools. [44]

Melatonin receptors signalling is highly dependent on the cell and the tissue in which they are expressed, resulting in a system bias (Figure 4) that, as in other receptor signalling systems, influences the functional outcome of the receptor activation. [31] The two receptors preferentially couple to $G\alpha_i$ protein which in turn decreases the cAMP levels at the cytoplasmic levels, but other G-proteins can be contacted, such as $G_{q/11}$, which would eventually be activated by MT_1 and MT_2 receptors, MT_1/MT_2 homodimers and heterodimers or MT_2/5-HT_{2C} heterodimers, resulting in different activated pathways. [31,45] While some of the most important ligands targeting melatonin receptors were characterized with orthogonal functional assays, [46] biased ligands are still not clearly identified.

Although MT_1 and MT_2 receptors are typically coupled to $G_{i/o}$ type, they promote different effects on circadian rhythms regulation. MT_1 receptors are predominantly expressed in the suprachiasmatic nucleus. By preventing firing of the hypothalamo-pituitary-adrenal axis, the subtype promotes sleep onset. Instead, effects promoting a phase-shift of the circadian rhythm are mostly mediated by the MT_2 receptor. [17] For this reason, both receptors have been considered a target for drug intervention aiming to treat sleep disorders. [23,47] Moreover, MT_1 knock-out mice had an increase in Non-Rapid Eye Movement (NREM) sleep, while MT_2 knock-out a decrease, suggesting an opposite role, potentially involving the orexinergic system, which is in turn involved in arousal and wakefulness. [48]

MT_1 receptors are diffusely expressed in the brain, and in other peripheral tissues, comprising the cardiovascular system, the immune system, reproductive organs, skin, liver, kidney, adrenal cortex, retina, pancreas, breast, prostate and the spleen. [24] When considering the central nervous system, the receptor is primarily located in the hypothalamus, substantia nigra, cerebellum, hippocampus and ventral tegmental area. [49] Presence of the MT_1 receptor in districts like breast and prostate has prompted implications in cancer diseases affecting these tissues. [23] Decreased expression of the MT_1 receptor at the level of the suprachiasmatic nucleus could be a physiological determinant at the basis of the Alzheimer disease. [50]

Role of the MT_1 receptor has been deeply linked to neuroprotective activity, for example, contrasting hypoxic-ischemic brain injury, [51] neurodegeneration in transgenic mouse models of the Huntington’s disease [52] and eliciting an antioxidant activity in cisplatin-induced ovarian damage. [53] In fact, MT_1 receptors have been additionally found in stem cells, such as human amniotic epithelial cells, at which receptor stimulation led to cell proliferation and neuronal differentiation. [54] Furthermore, mitochondrial-synthetized melatonin activates MT_1 receptor via automitocrine signalling on the outer membrane by which would prevent neurodegeneration associated with mitochondrial cytochrome c release and downstream caspase activation (Figure 4). [33]

The MT_2 receptor is additionally spread outside the CNS, and it is found in the immune system, in retina, in pituitary glands, blood vessels, kidney, testes, mammary glands, in bones, adipose tissue and in the skin. [24] Specific involvement of the MT_2 receptor in physiological roles was proven through different selective antagonists, such as 4P-PDOT, luzindole or DH97. [44] Through MT_2 receptor-MEK/ERK signalling axis, melatonin enhances alkaline phosphatase activity in differentiating human adult mesenchymal stem cells grown in osteogenic medium [55] and promotes bones remineralization in mice in which the MT_2 was not knocked out. [56]

As well, knock out experiments showed that the MT_2 receptor is selectively involved in the regulation of neuropathic pain, [57] which is related to the presence of the receptors in glutamatergic neurons in the rostral ventrolateral periaqueductal grey modulating descending antinociceptive pathways, [58,59] which would in turn include opioid μ receptor activation in this mechanism. [60] MT_2 receptors are additionally selectively involved in the promotion of NREM phase [61] and of anxiolytic effects [62].

Interest has been elicited by common single nucleotide polymorphisms of MT_2 receptor, and subsequent receptor bias, increasing type 2 diabetes probability, which is associated to reduction in the activation of the $G\alpha_i$ proteins and of the spontaneous recruitment of β-arrestins. [63,64] Diabetes risks would be due to the increased fasting plasma glucose levels and impaired insulin secretion because of these defective signalling pathways. [65] Moreover, removal of MT_1 receptor in mice led to increased insulin resistance. [66]

Recently, the role of melatonin receptors was investigated for the treatment of gliomas and medulloblastomas. It was observed that MT_1 had an oncoprotective impact on the proliferation of human glioma and medulloblastoma cell lines, while MT_2 was over-expressed and promoting cell tumour growth, therefore presenting opposite effects on tumour progression. [67]

In rats, melatonin has acted as a vasorelaxant in the mesenteric artery and aorta [68]. Conversely, in the caudal artery, melatonin has also been found to be a vasoconstrictor [69,70]. Moreover, the two receptors were recently found to exhibit an opposite role in controlling the body temperature; during darkness, MT_1 receptor activation increased the body temperature, while MT_2 decreased it. [71]

2.3 STRUCTURES OF MELATONIN RECEPTORS

For decades, drug design of melatonergic ligands relied on either ligand-based studies or the use of homology modelling. [5,72] In 2019, MT_1 and MT_2 crystal structures were finally released, co-crystallized with nonselective agonists. In these structures, the receptors were captured in their inactive states due to the presence of several thermostabilizing mutations, which were known to promote the folding stability of the TM7 domain in class A GPCRs. [73] The structures including MT_1 receptor complexes with ramelteon (*6ME2*), 2-phenylmelatonin (*6ME3*), 2-iodomelatonin (*6ME4*) and agomelatine (*6ME5*), [74] and MT_2 receptor bound to ramelteon (*6ME9*) and to 2-phenylmelatonin (*6ME6*, including structures mutations H208$^{5.46}$A in 6ME7, and D86$^{2.50}$ restoration in *6ME8*) [75]. The numbers in superscripts stand for the Ballesteros-Weinstein numbering [76] used to indicate location of residues inside the TM domain with respect to the most conserved residue of class A in each helix n, to which n.50 numbering is assigned. An additional MT_1 receptor structure bound to 2-phenylmelatonin (*6PS8*) was obtained after ligand exchange and replacement of agomelatine in the binding site. [77] Serial femtosecond crystallography [78] has been used to obtain these structures in lipidic cubic phase, by using the X-ray free electron lasers (XFELs) technology, [79] which allows to study time-resolved events in the picosecond-timescale. To increase the receptor thermostability [73], mutations (Figure 5) have been introduced to the sequence (nine in the MT_1 receptor and eight in the MT_2 receptor), including D73/86$^{2.50}$N, L95/108^{ECL1}F, G104$^{3.29}$A (only at the MT_1 receptor), F116/129$^{3.41}$W, N124/137$^{3.49}$D, C127/140$^{3.52}$L, W251/264$^{6.48}$F, A292/305$^{7.50}$P and N299/312$^{8.47}$D. These mutations functionally inactivated the receptors leading to a 40- and 120-fold reduction of melatonin binding affinity at the MT_1 and MT_2 receptors, respectively. This low-affinity state is not probably existing *in vivo* since melatonin receptors are known to convert into a high-affinity complex with the G-protein immediately upon agonist binding. [80,81,82]

Some of these mutations actually abrogate the major differences distancing melatonin receptors from the other Class A GPCRs, e.g., the presence of NR$^{3.50}$Y and NA$^{7.50}$XIY motifs in lieu of the more conserved E/DR$^{3.50}$Y and NP$^{7.50}$XXY ones. Mutation A305$^{7.50}$P at the MT_2 receptor is known to functionally inactivates the receptor by possibly preventing G-protein binding. [83] Furthermore, even tryptophan of CWXP motif, residue deemed as the "*toogle switch*" [84] usually deemed related to the activation mechanism, has been mutated into a phenylalanine, as well as the D2.50 responsible for the binding of the sodium ion in an allosteric site inside the TM bundle. [85] However, crystal of the MT$_2$ receptor, in which mutation D86$^{2.50}$N was not performed, conserved the secondary structure and fold of the other ones, suggesting that this mutation alone did not significantly affect the receptor structure, [75] as previously reported for other GPCRs. [86]

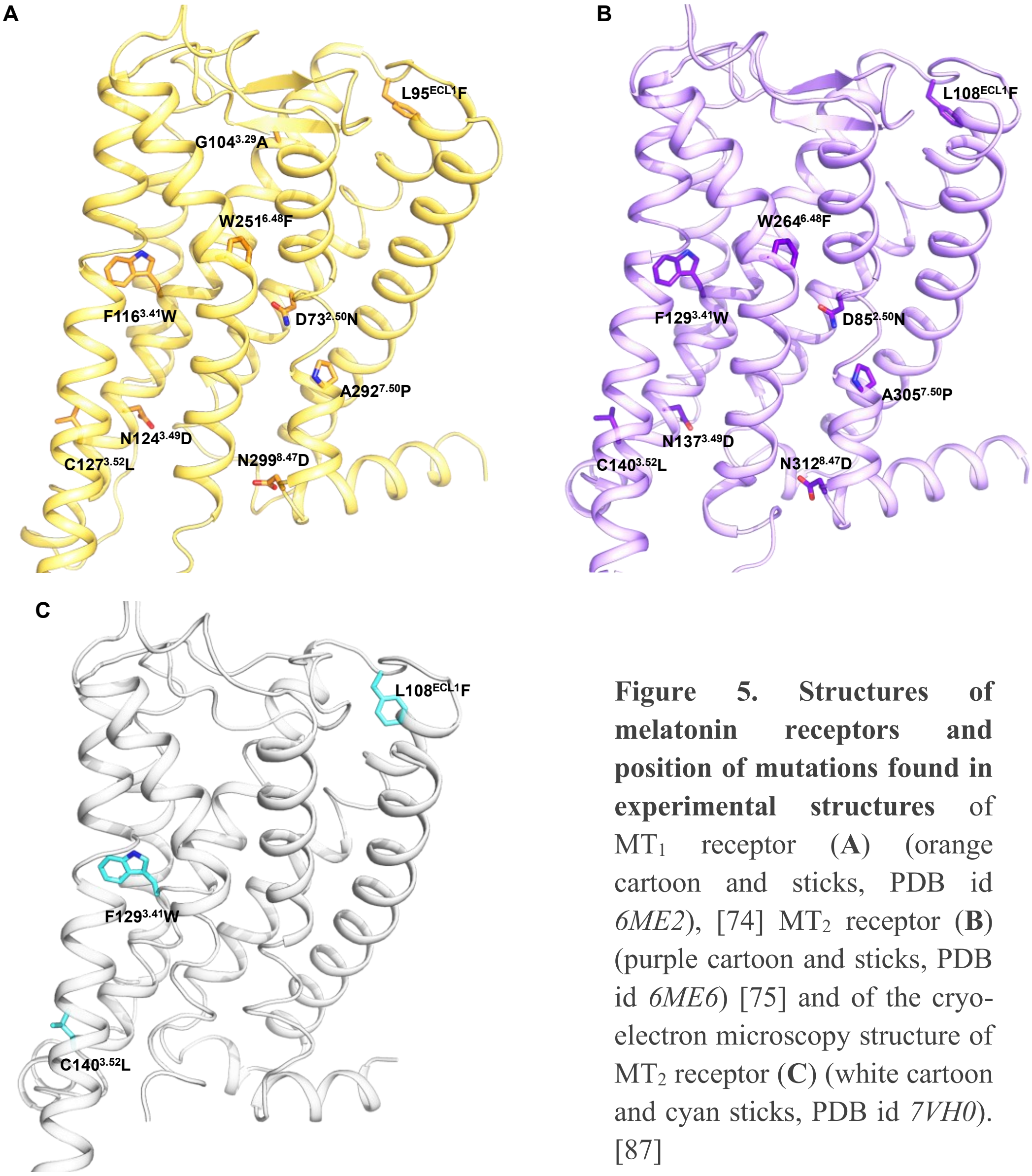

Figure 5. Structures of melatonin receptors and position of mutations found in experimental structures of MT$_1$ receptor (**A**) (orange cartoon and sticks, PDB id *6ME2*), [74] MT$_2$ receptor (**B**) (purple cartoon and sticks, PDB id *6ME6*) [75] and of the cryo-electron microscopy structure of MT$_2$ receptor (**C**) (white cartoon and cyan sticks, PDB id *7VH0*). [87]

Finally, G104$^{3.29}$A mutation was applied to the MT$_1$ receptor only, and it is the only residue, directly facing bound ligands at both receptors, to be different at the two subtypes. Excluding this difference, melatonin receptor binding sites are characterized by an extreme conservation of the residues. The MT$_2$ receptor is characterized by a wider binding site, around 60 Å^3 wider in the portion accommodating substituents in position 2 of the indole ring of melatonin, [75] which, depending on their size and shape, are known to increase the binding affinity and subtype selectivity for this receptor. [44]

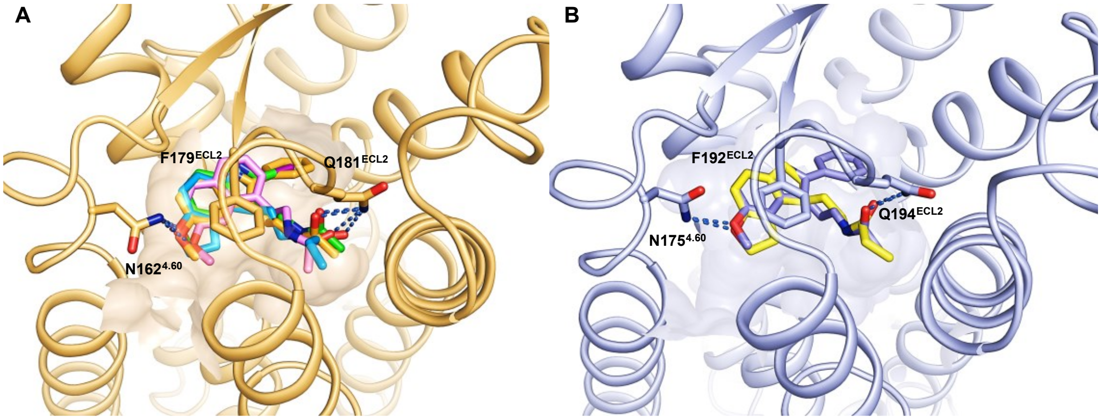

Figure 6. X-ray crystal structures of melatonin receptor binding sites and co-crystalized ligands. (**A**) MT$_1$ receptor (orange cartoon and sticks, PDB id *6ME3*) bound to 2-phenylmelatonin (orange sticks, PDB id *6ME3*), 2-iodomelatonin (green sticks, PDB id *6ME4*), ramelteon (light blue sticks, PDB id *6ME2*) and agomelatine (pink sticks, PDB id *6ME5*). [74] (**B**) MT$_2$ receptor (blue cartoon and sticks) bound to 2-phenylmelatonin (blue sticks, PDB id *6ME6*) and ramelteon (yellow sticks, PDB id *6ME9*). [75]

Bound ligands mostly engage in two hydrogen bonds via with their methoxy oxygen (or dihydrofuran oxygen in the case of ramelteon) and sidechain alkylamide oxygen groups with N162/175$^{4.60}$ and Q181/194^{ECL2}, respectively (Figure 6). Notably, the binding site lacks D3.32, which is replaced by M107/120$^{3.32}$, and no ionizable residue belongs to the binding site. Such an important conserved residue able to recognize protonated amines is conserved among many class A GPCRs, which have important physiological roles. The absence of the ionizable residue is one of the main reasons at the basis of the ligand selectivity with respect to serotonin receptors. Serotonin and melatonin, despite having a similar structure, are characterized by very different physicochemical properties which hamper binding of melatonin at serotonin receptors and vice versa. [74]

Another important structural peculiarity differentiating melatonin receptors by other Class A GPCRs, albeit with some notable exceptions comprising rhodopsin [88] and some of the lipid receptors, [89,90] is the sealing of the binding site from the extracellular environment, due to ECL2 acting as a lid with a 3:5 β-hairpin with a type I β-turn fold. The loop is deeply inserted in the TM bundle and it would strongly hamper ligand recruitment from the solvent, such as in the case of endocannabinoid receptors. [91] Moreover, the ECL2 is further stabilized by the canonical disulphide bridge with TM helix III (C100/C113$^{3.25}$ to C177/C190^{ECL2}). [74,75] Previous to X-ray structures, the importance of the ECL2 in ligand recognition was as well recognized through mutagenesis studies and chimeric receptors. A chimeric GPR$_{50}$ bearing from the MT$_1$ receptor a transplanted ECL2 portion recovered the ability to bind melatonin. [92] Given this structural architecture of the binding site and the high lipophilicity of their endogenous agonist, ligand recruitment from the aqueous extracellular environment was already pointed out as unlikely by crystallographers. [74,75] Therefore, a lateral ligand access has been proposed through a hydrophobic cleft between the TM helices IV and V. Docking calculations suggested that this opening can accommodate portions of bitopic and/or dimeric compounds, such as CTL 01-05-B-A05, an agomelatine dimer. [74,93] Removal of the TM IV kink, thus restricting the lipophilic channel via mutation of P174$^{4.59}$ to glycine or alanine, completely hampered the ability of the MT$_2$ receptor to bind melatonin or iodomelatonin. [83] Instead, the presence of a putative hydrophilic channel connecting the binding site to the extracellular environment, either present at the MT$_2$ receptor [93] or at both receptor subtypes [80] is still unclear. A different rotamer of Y281/294$^{7.39}$ in the MT$_1$ and MT$_2$ crystal structures would account for a slightly larger opening through the EC vestibular region at the MT$_2$ receptor. [75]

Finally, H195/208$^{5.46}$ is highly conserved in melatonin receptors; mutation in the MT$_1$ subtype reduces protein expression and decreases melatonin binding affinity [74,94], and reduces binding affinity at the MT$_2$ receptor. [95] Moreover, mutation to alanine is reported to reduce the width of the lipophilic entrance between the two TM helices and the volume of the orthosteric site by 50 Å^3. [75]

Later, structures of the active ternary complexes of MT_1 and MT_2 receptors bound to G_i protein were obtained via cryo-electron microscopy. MT_1 receptor was obtained bound to ramelteon by two different research groups and with different conformation of some key residues (*7DB6* [96] and *7VGZ* [87]) and to 2-iodomelatonin (*7VGY*) [87]. As well, a structure of the ternary complex of MT_2 bound to ramelteon was released (*7VH0*) [87]. In these structures there was no need for the introduction of thermostabilizing mutations, except for the MT_2 receptor one, for which mutations L108^{ECL1}F, F129$^{3.41}$W and C140$^{3.52}$L were still required [87].

One of the main structural differences in the binding sites is the entrance of H195/208$^{5.46}$ in the pocket at the MT_1 and MT_2 receptor active structures (Figure 7). [87] Due to the closeness to the P199/212$^{5.50}$I115/V128$^{3.40}$F247/260$^{6.44}$ motif (also called "connector region"), important for receptor activation and coupling of the orthosteric site to the intracytoplasmic region, [97] Wang et al. highlighted the importance of the residue for receptor activation. [87] Instead, in the MT_1-ramelteon complex reported by Okamoto et al. in ref. 96, this electron density is attributed to the inward packing of F196$^{5.47}$ inside the binding site.

Finally, in Johansson et al., [75] Y187/200$^{5.38}$ was described as a gatekeeper residue controlling ligand residence time, i.e., being in a closed conformation, near the TM bundle and interacting with residues of TM helix IV, at the MT_2 receptor and in an open one at the MT_1 receptor, pointing toward the lipid bilayer (Figure 7.A-B). In the active complex of MT_1 receptor from Okamoto et al. the tyrosine is in its closed conformation able to tighten the hydrophobic TM channel. In Wang et al., [87] an alternative conformation of Y187/200$^{5.38}$ is reported; in this case, the conformation of the residue is open at the MT_2 receptor and closed at the MT_1 receptor, as in the structure provided by Okamoto et al. (Figure 7.C-D). The closed conformation at the MT_1 receptor could be stabilized by N162$^{4.60}$, whose mutation to alanine would greatly affect the intrinsic activity at this receptor. [74,87]

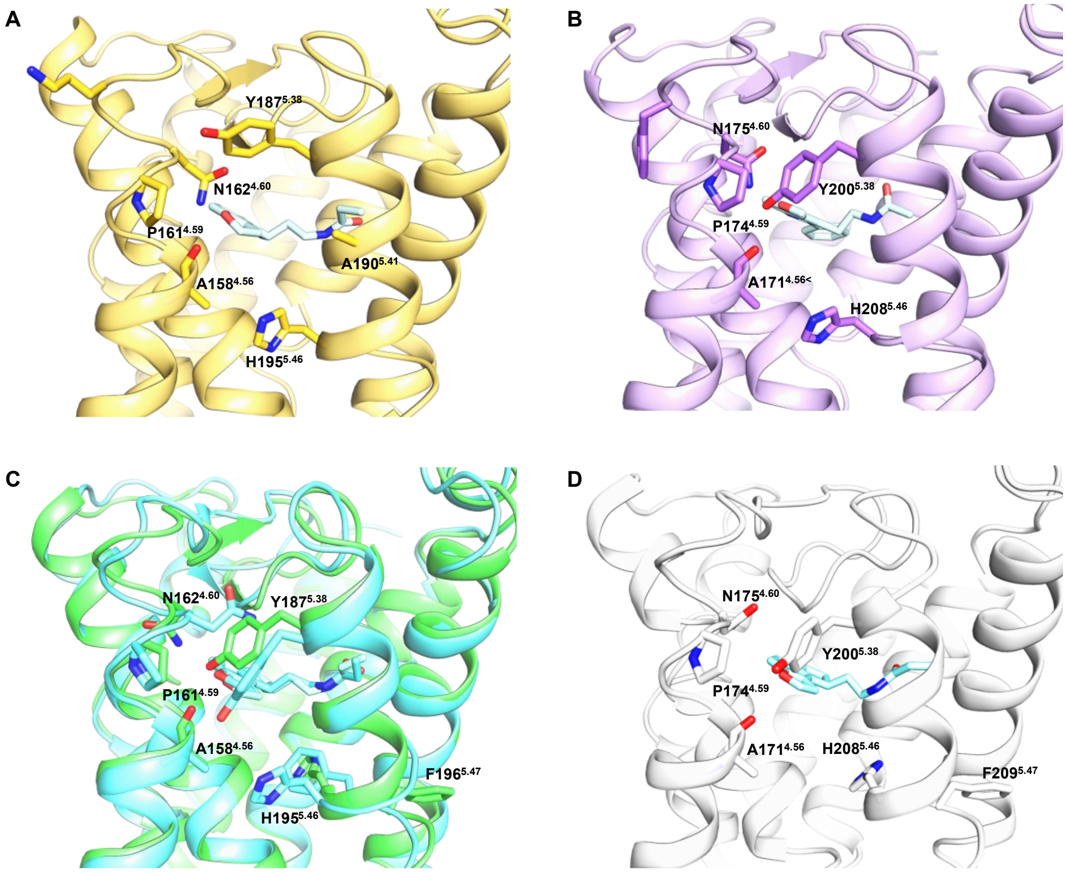

Figure 7. Residues bordering the hydrophobic channel between TM helices IV and V. MT$_1$ receptor inactive state (yellow cartoon and sticks, PDB id *6ME2*, **A**), MT$_2$ receptor inactive state (purple cartoon and sticks, PDB id *6ME6*, **B**), MT$_1$ receptor active state in two alternate conformations (cyan and green cartoon and sticks, PDB id *7DB6* and *7VGZ*, respectively, **C**) and MT$_2$ receptor active state (white cartoon and sticks, PDB *7VH0*, **D**).

However, the most prominent conformational changes between the cryo-electron microscopy structures of the ternary complexes and the previous crystal structures regard the 11-15 Å outward shift of the intracytoplasmic portion of the TM helix VI, consisting of around depending on the considered structure (Figure 8). [87,96] Packing of F245/258$^{6.41}$ with Y207/220$^{5.58}$ seems important to achieve such a pronounced displacement with respect to other GPCRs, stabilizing the active conformation of the receptors. Given that the selectivity toward G$_i$ protein coupling is usually given by a smaller tilt of the helix, the unexpected shift could be assisted by the presence of multiple hydrophobic residues in this portion of the receptor, while the coupling selectivity could be due to the relatively narrow cavity forming at the cytoplasmic side of the receptor. [96] G_i $\alpha5$ helix (C-terminus) establishes interactions with the hydrophobic core of the receptor, particularly with TM helices III and V-VII, while contacts with the ICL2 are minimal due to the shift of α_N helix. However, different residues of the ICL2 can possibly rationalize the promiscuous coupling of the MT_1 receptor with the G_q protein, offering a differenced binding surface. [87] Other important movements concerning TM helices on the intracytoplasmic side are further analyzed in Chapter 7, which focuses on the study of molecular determinants leading to receptor activation.

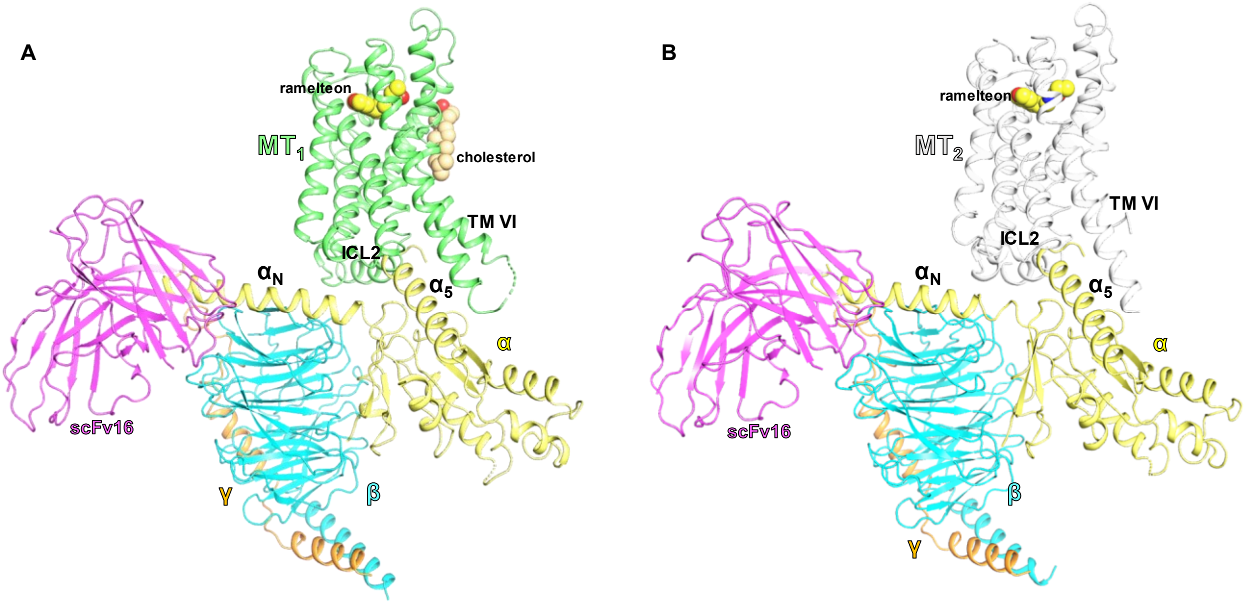

Figure 8. Cryo-electron microscopy structure of the ternary complexes of melatonin receptors. MT_1 (**A**, PDB id *7VGZ*) and MT_2 (**B**, PDB id *7VH0*) receptors in complex with ramelteon and bound to G_i protein heterotrimeric complex. [87]

2.5 MELATONIN RECEPTORS LIGANDS

As recently reviewed, [98] most of the ligands targeting the two melatonin receptors have been obtained via medicinal chemistry programs starting from direct structural analogues of melatonin. Nearly all the proposed scaffolds mainly recapitulate three fundamental elements: *i*) an aromatic ring, being the indole or bioisosteres, *ii*) the methoxy group on the aromatic nucleus, and *iii*) the (alkyl)amide side chain. In fact, for three decades, drug design was exclusively driven by ligand-based approaches, due to the lack of receptor three-dimensional structures. [5] Just recently, the release of crystal structures of melatonin receptors [74,75] led to extensive virtual screening campaigns consisting of docking calculations of rather large datasets eventually resulting in the discovery of novel chemotypes, [99,100] which could be further optimized to improve their pharmacological properties. Prior to release of crystal structures, rational efforts relied on different methodologies, such as 3D-QSAR and pharmacophore analysis. [5] Just a few compounds entered clinical practice or were evaluated in clinical trials and they mostly recapitulate melatonin structure, in which eventually the indole was replaced with a benzo-dihydrofuran (ramelteon) or a naphthalene (agomelatine) ring. The majority of melatonergic compounds do not achieve any subtype selectivity; compounds reaching a thousand-fold selectivity at the MT_2 receptor are available, mostly due to a reduced binding affinity at the MT_1 receptor, and substitutions providing this pharmacological behaviour have been understood for a while. [44] In fact, the presence of a substituent in position N1 or C2 of the indole scaffold of melatonin analogues and arranged in an out-of-plane position with respect to the indole plane, would account for MT_2 selectivity as well as for the loss of intrinsic activity. [101,102] Conversely, requirements to achieve selectivity at the MT_1 receptor are still not well understood and for this reason the design of compounds achieving the same level of subtype selectivity is not straightforward. [98,44]

2.5.1 Melatonergic compounds in clinical practice and trials

Melatonin is a popular remedy to sleep problems related to circadian rhythm disorders with different aetiologies. However, the short half-life, due to the presence of metabolically liable sites [21] leading to fast elimination, strongly limits its therapeutic efficacy. Therefore, a prolonged-release formulation, marketed as Circadin®, has been approved by the European Medicines Agency. Dietary use of melatonin is common as a sleep aid or to alleviate circadian disorders caused by jet lag. [44]

The other compounds reaching at least the clinical phase (Figure 9) were not characterized by any level of selectivity toward the two receptor subtypes. The first synthetic melatonergic ligand available in the clinical practice was ramelteon (Rozerem®), [103,104] developed by Takeda for insomnia and possessing a longer half-life than melatonin. Its major metabolite, obtained via ω-1 hydroxylation of the side chain is believed to significantly concur to the clinical outcome due to its high plasmatic levels. [21,44]

Approved for the treatment of non-24-hour sleep-wake disorder, which affects blind people, is tasimelteon (Hetlioz®), [105] developed by Vanda Pharmaceuticals and licensed from Brystol-Myers Squibb. Despite the absence of the kynurenine pathway and its extended half-life, tasimelteon metabolism is rather complex and needs further investigation. [21]

Agomelatine, consisting of a naphthalene scaffold, which closely relates to melatonin, was developed by Servier and is marketed as Valdoxan®. Being additionally a high-nanomolar 5-HT$_{2C}$ antagonist, it is characterized by a unique pharmacological profile allowing for its therapeutic use in depression. [106,107]

Furthermore, TIK301 (also known as PD-6735, β-methyl-6-chloromelatonin) [108] and Neu-P11 (also known as piromelatine) [109] have been advanced to phase II clinical trials. In particular, TIK-301 is functionalized with a 6-chlorine substituent, protecting from the detrimental 6-hydroxylation and achieving a receptor affinity similar to melatonin. [21] Piromelatine, which is additionally a serotonin 5-HT$_{1A/1D}$ receptor agonist, has been further investigated for Alzheimer's disease. [110]

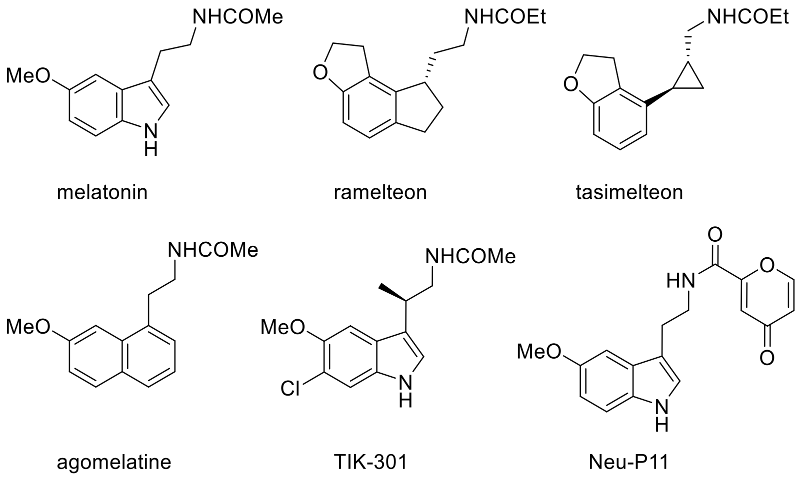

Figure 9. Melatonergic ligands used in the clinical practice or evaluated in clinical trials.

2.5.2 Melatonin receptors nonselective agonists

Most melatonergic ligands show an MT_1/MT_2 nonselective profile (Figure 10). These molecules included direct substitutions of melatonin, such as 2-iodo- [111] or 2-phenylmelatonin, leading to about ten-fold increase in the binding affinity. [112] In particular, 2-[^{125}I]-melatonin has become the reference radioligand for these receptors. [113] Other modifications of the indole scaffold, resulting in TIK-301 [108] and in the introduction of methyl-substitutions on the alkylamide chain [114] do not have any impact on the subtype selectivity. 6-Halogen derivatives do not change the binding affinity, while they increase the metabolic stability by protecting metabolically liable sites. [44]

To replace the indole with smaller aromatic rings leads to flexible analogues characterized by different alkylamide chains. Among them, phenylakylamide **1** [115] summarizes the three essential pharmacophore features of melatonin. While maintaining a hundred times lower binding affinity than the endogenous ligand, it displays the minimal requirements for target engagement. Bioisosteric substitution led to the phenoxyethylamide (**2**) and thiophenoxyethylamide (**3**) derivatives; chiral substitutions have been evaluated on the β-position, leading to the (*S*)-β-methyl enantiomers being the eutomers. [116] Similarly, the *N*-anilinoethylamide scaffold progenitor, UCM793, [117] in turn developed from N-(3,3-diphenylpropenyl)-alkanamides, [118] do not display any subtype selectivity, maintaining the nonselective agonist behaviour.

More often, the indole has been replaced with bioisosteric aromatic nuclei, comprising naphthalenes [19], indanes, [103] benzofurans, [119] 4-azaindoles, [120] 7-azaindoles, [121] tetralines, [122] tetrahydroquinolines, [123] quinolines, [124] tetrahydroisoquinolines, [125], benzoxazoles, [126] benzothiophenes. [127]

In a few cases, the aromatic system has been enlarged, resulting in tri- tetra- and a pair of penta-cyclic scaffolds. [98,128,129] Notably, the methoxy group has been enclosed in such rings in different occasions, as in the case of ramelteon and other tricyclic derivatives [103] developed by Takeda, in which a dihydrofuran has been condensed with the indane scaffold.

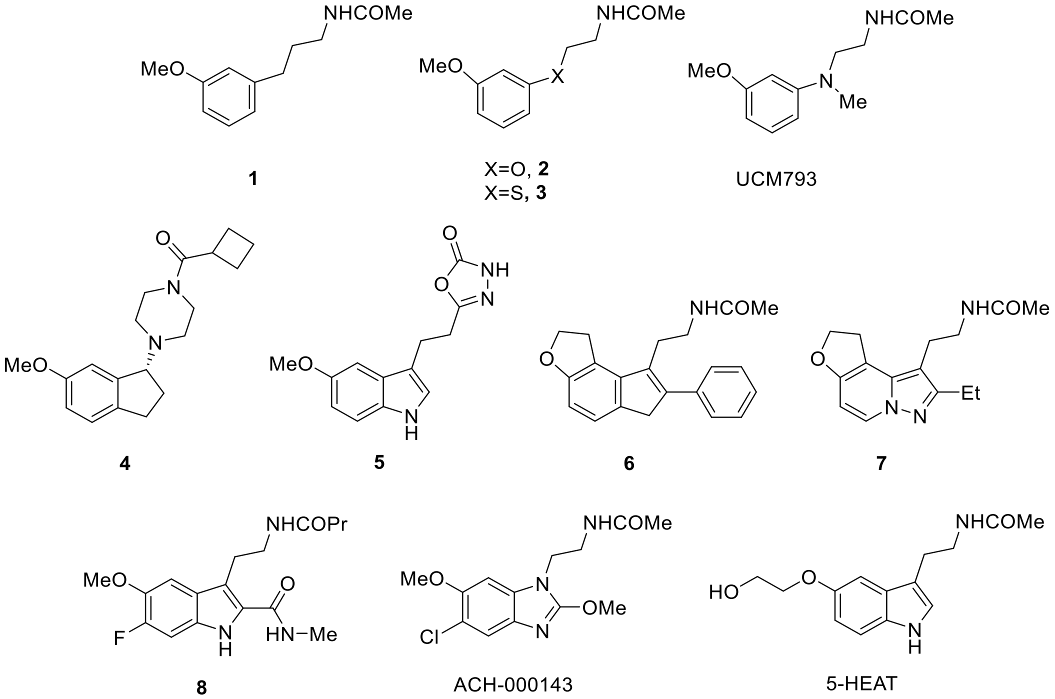

Figure 10. Non-selective MT_1/MT_2 melatonergic ligands

Alternatively, in the case of benzoxazole derivatives developed by Bristol Myers Squibb, the methoxy oxygen has been replaced with a bioisosteric nitrogen. [126] Other structural modifications led to the enclosure of the alkylamide chain into an additional cycle, such as cyclopropyl derivatives, [126,130] piperidine [111] or piperazine derivatives (such as compound **4**), [131] and fused tricyclic derivatives. [132,133] Some of the previous compounds helped to determine the bioactive conformation of melatonin prior to the release of receptor X-ray crystal structures. [5] Eventually, the alkylamide group was even replaced with heterocycles (e.g., compound **5**) . [134]

Enlargement of the indole scaffold through the incorporation of the 2-phenyl group, led to IIK7 (Figure 11) and many other derivatives, eventually achieving selectivity for the MT_2 receptor. [135] Incorporation of the fused dihydrofuran in the polycyclic scaffold led to dihydro-2*H*-indeno[5,4-b]furan derivatives, and 2-aryl substituents, such as compound **6**, achieved some of the highest affinities at both receptor subtypes. [136] Derivative **7**, designed to increase the metabolic stability, maintained the high affinity of melatonin, contemporarily increasing the oral bioavailability. [137]

Further modifications were made to reduce CNS penetration and, therefore, obtaining peripherally restricted agents. Indole-2-carboxamides (e.g., compound **8**), endowed with a preferential peripheral distribution, were patented for the treatment of the urinary incontinence. [138] Recently, 2-alkoxybenzimidazoles with increased water-solubility showed a preferential peripheral localization. Chronic administration of one of these derivatives (ACH-000143) lowered the levels of hepatic triglycerides and steatosis in diet-induced obese rats. [139]

Finally, a unique MT_1/MT_2 nonselective compound is represented by *N*-(2-(5-(2-hydroxyethoxy)-1*H*-indol-3-yl)ethyl)acetamide (5-HEAT), compound with a different functional profile at the two receptor subtypes, being an MT_1 agonist and MT_2 antagonist. [140]

2.5.3 MT_2-selective compounds

Nonselective antagonist luzindole and MT_2-selective antagonist/partial agonist 4-phenyl-2-propionamidotetralin (4-P-PDOT, Figure 11) have been the reference antagonists used as pharmacological tools to recognize subtype-specific activities. [111] The antagonist DH97 achieves a higher selectivity with respect to luzindole by having a longer acyl chain. [141] Instead, restoring the 5-methoxy substituent led to benzylmelatonin being an MT_2-selective partial agonist. [111] 4-P-PDOT is a racemic mixture composed of four stereoisomers, displaying a 330-fold MT_2 selectivity. [111] Among them, the (+)-(2*S*,4*S*) eutomer fulfills the requirements of a pharmacophore model developed for melatonin receptor agonists. [142]

Enclosure of the 2-phenyl group in a condensed scaffold led to tricyclic compounds, endowed with a non-planar dibenzocycloheptene structure, such as UCM549, in which the introduced aromatic ring is out-of-plane with respect to the one superimposed to the indole ring plane. [143] The derivatives exhibited a moderate MT_2 selectivity and a decreased intrinsic activity responsible for the identification of inverse agonists at the MT_2 receptor. [144]

Tetracyclic derivatives IIK7 and K185, characterized as well by a condensed phenyl ring, achieved 89- and 132-fold selectivity at the MT_2 receptor, respectively. [135] While IIK7 is a selective agonist, K185 behaves as an antagonist. Notably, the phenyl ring attached to the indole would be placed with an out-of-plane arrangement for the latter, similar to the position occupied by the phenyl ring of 4-P-PDOT and luzindole and consistent with the rationale leading to dibenzocycloheptene derivatives.

The introduction of a phenyl substituent on the aniline nitrogen of *N*-anilinoethylamide scaffold of UCM793 led to UCM765, being a partial agonist showing a 60-fold selectivity at the MT_2 receptor. [117] Protection of UCM765 metabolically liable positions with halogens led to the development of UCM924. [145] The compounds were characterized in *in vitro* and *in vivo* studies, to demonstrate their activity on the circadian rhythm. In particular, UCM765 increased duration of NREM sleep, without altering REM sleep and sleep architectures as happens with benzodiazepines. [61] Moreover, these compounds showed antinociceptive [58] and anxiolytic properties. [62]

The introduction of a bulkier substituent on the aniline nitrogen of *N*-anilinoethylamide melatonergic ligands, such as the β-naphthyl group, led to UCM800, being a highly MT_2-selective (1000-fold) and potent antagonist. [117] Eventually, the *N*-anilinoethylamide scaffold was rigidified and transformed into the tetrahydroquinoline ring, in which the introduction of a benzyl group on the tetrahydroquinoline nitrogen led to a highly selective full agonist. [123]

One among the few compounds characterized by a scaffold prescinding the indole and its bioisosteres is represented by DIV880, which scaffold was in turn retrieved via high-throughput screening campaigns performed by Servier industries. [146,147] The compound was used as a radiolabelled ligand and its activity appears confined to the MT_2 receptor subtype. [148]

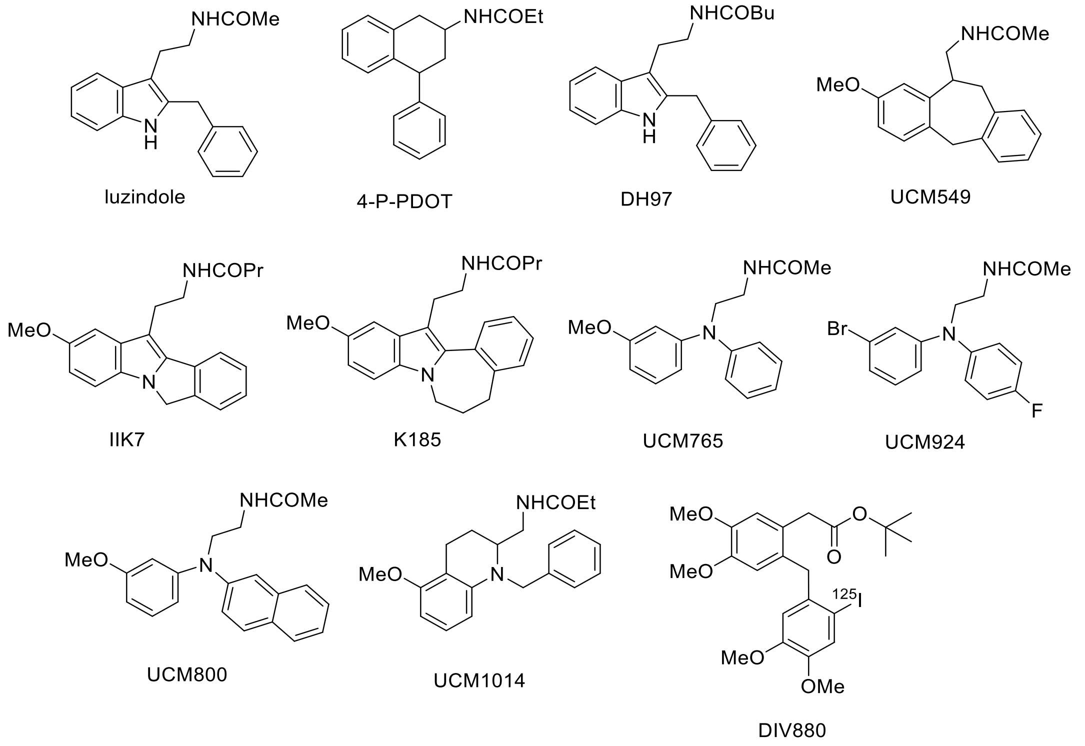

Figure 11. MT_2-selective melatonergic ligands

2.5.4 MT_1-selective compounds

As anticipated, the level of selectivity shown by MT_2-selective ligands is not matched by currently available MT_1-selective agonists (Figure 12). [98,44] While the former can reach a thousand-fold selectivity, MT_1-selective ligands rarely exceed a 50-fold selectivity, which is the minimum according to IUPHAR guidelines. [149] The most common structural element resulting in a limited MT_1 selectivity is a bulky, hydrophobic ether replacing the 5-methoxy substituent of melatonin. The first MT_1-selective agonists were dimeric compounds in which two agomelatine monomers were linked through a polymethylene spacer, obtaining the highest selectivity with three (compound **9**, Figure 11) or four methylene groups (compound **10**). [150] Monomeric compounds which bear a phenyl-butyl substituent on the benzoxazole scaffold (compound **11**) [126] or on the *N*-anilinoethylamide one (UCM871) [151] achieved a 35- and a 66-fold selectivity, respectively. Other agomelatine derivatives resulted in the most-selective MT_1 compounds to date, being a biphenylcarboxylic acid (compound **12**) and its corresponding methyl ester (compound **13**), reaching a 93-fold and 72-fold MT_1 selectivity, respectively. [152]

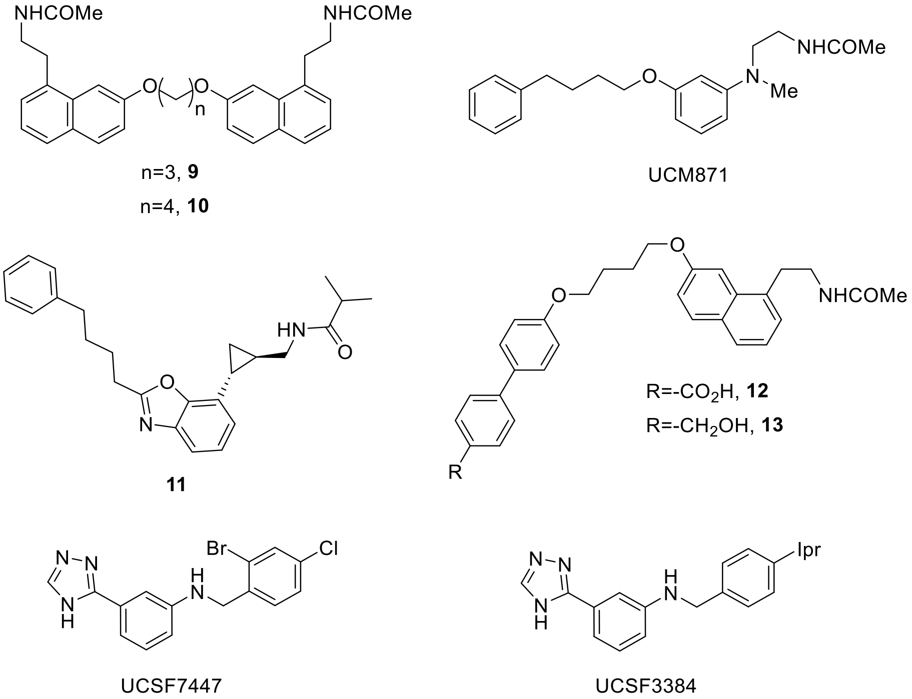

Figure 12. MT_1-selective melatonergic ligands

Even if they possess a lower affinity, selective inverse agonists, recently retrieved via a large structure-based virtual screening, [153] UCSF7447 and UCSF3384, are characterized by a benzylaminophenyl scaffold bearing a 2-(1,3,4-triazolyl) ring in the position meta of the aniline ring and act selectively at the MT_1 subtype in functional assays. They display unseen pharmacological properties due to the control of the MT_1 receptor on the suprachiasmatic nucleus. The compounds are able to decelerate circadian rhythm re-entrainment and, therefore, could be used for the treatment of the east-bound jet lag. [99] However, the elicited signalling pathways should be further characterized as the physiological effect could be related to biased agonism. [154]

Chapter 3. Methods and theory of free-energy simulations

3.1 UNBIASED SAMPLING

In this chapter, a short theoretical background to some of the most widely used free-energy methods employed in the Thesis is provided, after an initial introduction to statistical mechanics in the context of molecular simulations, such as classical molecular dynamics (MD).

In classical mechanics, a three-dimensional molecular system is represented by a set of coordinates $\{\vec{x}_i\}$ and a conjugate set of momenta $\{\vec{p}_i\}$ for each particle i. Together, these quantities define a *microstate*, i.e., a point of the phase space $\Gamma(\vec{x}_i, \vec{p}_i)$, each with its own coordinates and momenta. The time evolution of the system defines a trajectory, connecting the points in the phase space visited over time.

In statistical mechanics, each macroscopic property, which is time-independent at equilibrium conditions, is defined as the average of the microscopic operator, $\mathcal{O}(\vec{x}_i, \vec{p}_i)$, over all accessible states, weighted by the probability of visiting each state. Thus, in principle it is possible to define the time-independent probability density, $\mathrm{p}(\vec{x}_i, \vec{p}_i)$, characterizing each microstate. Experimental measurements provide the average of the same operator over the measured time and over a macroscopic number of atoms in the system.

From the point of view of statistical mechanics, for macroscopic systems (10^{23} atoms) it would be practically impossible to visit each point of the phase space to determine the ensemble average of the microscopic operator and extrapolate the corresponding time-independent macroscopic property or *macrostate*. However, at equilibrium, macroscopic properties can be derived from MD algorithms based on the assumption that the system of interest satisfies the ergodic hypothesis stating that for an isolated system (microcanonical ensemble or NVE ensemble) and infinite sampling time, the trajectory will visit all the microstates with equal probability. Meaning that time and ensemble averages coincide for an initial condition of the infinitely long trajectory.

In systems at equilibrium with a thermal bath, i.e., under the conditions of constant number of atoms, system's volume and temperature (NVT or canonical ensemble), such as the ones describing biomolecules and protein-drug interactions at a given temperature T, the probability density is defined as the Boltzmann factor,

$$p(\vec{x}_i, \vec{p}_i) = \frac{1}{Z} e^{-\frac{\mathcal{H}(\vec{x}_i, \vec{p}_i)}{k_B T}} \tag{3.1}$$

where $\mathcal{H}$ is the Hamiltonian describing the total energy of the system (i.e., the sum of kinetic and potential energy) and Z represents the partition function. The total energy given by the Hamiltonian is not conserved. Systems configurations following the probability density reported in eq. 3.1 are called Boltzmann distributed.

The partition function Z over the phase space Γ is defined as follows

$$Z = \int_{\Gamma} e^{-\frac{H(\vec{x}_i, \vec{p}_i)}{k_B T}} \tag{3.2}$$

In principle, once the partition function is known, all the macroscopic properties can be derived. First of all, the free energy of the system, which is given according to:

$$A = -k_B T \cdot \ln Z \tag{3.3}$$

Oftentimes, it is necessary to estimate the probability distributions of certain geometric properties of the systems, including the so-called collective variables (*CV*s), which are defined as suitable functions of the particle coordinates $\{\vec{x}_i\}$:

$$p(CV_0) = \sum_{CV(x) = CV_0} p(\vec{x}_i, \vec{p}_i) \tag{3.4}$$

or in the associated free-energy differences with respect to values of the *CV*:

$$A(CV_0) = -k_B T \cdot \ln p(CV_0) \tag{3.5}$$

However, in unbiased simulations, many biological events do not happen in a reachable timescale effectively making it impossible for the system to visit microstates for which it is needed to overcome free-energy barriers of more than a few $k_B T$ (at 300 K, the thermal fluctuations amount to around 0.597 kcal). To access these *rare events,* enhanced sampling methods, further discussed in the next pages, are needed.

The NVT ensemble discussed in the previous paragraphs is not the only one that can be considered in MD simulations. In most cases, the system is in equilibrium with a thermal bath with fixed temperature T and with a fixed number N of components. In addition, it can be either confined in a box of volume V (canonical ensemble or NVT ensemble) or kept at a fixed pressure P (isobaric-isothermal ensemble or NPT ensemble). In the latter case, the pressure can be differently exerted depending on the direction (i.e., semi-isotropic/anisotropic couplings usually applied to membrane systems such as the ones here treated). Occasionally, another set of conditions consists in keeping the temperature and the volume fixed, and allowing the number of molecules to fluctuate, while fixing the chemical potential (Grand Canonical ensemble or μVT ensemble). This approach has been used in Chapters 5, 6 and 7 during the preparation of the systems to hydrate buried sites within the protein structure in combination with the Monte Carlo algorithm (Grand Canonical Monte Carlo simulations) [155] in order to reduce the time required for the equilibration of internal waters. These waters are generally regarded as important to the function of Class A GPCRs. [156]

ENHANCED SAMPLING METHODS

In the case of rare events, different enhanced sampling algorithms [157,158,159] have been developed. These methods usually divide in algorithms adopting *CV*s and those that do not require a specific one. The former comprises most of the free-energy simulations used in the Thesis. In the enhanced sampling simulations requiring a *CV*, an additional bias potential is added to the unbiased Hamiltonian of molecular dynamics, as following

$$H_{biased}(\vec{x},\vec{p},t) = H_{MD}(\vec{x},\vec{p}) + V_{bias}(\vec{x},t) \qquad (3.6)$$

By knowing the impact of the added potential, *a priori* free-energy differences between different configurations of the system can be obtained.

3.2. STEERED MOLECULAR DYNAMICS

Steered molecular dynamics (SMD) simulation is a non-equilibrium method in which a collective variable (*CV*) is explored through the application of a bias potential, defined in the form of a harmonic restraint:

$$\Delta V = \frac{k}{2}(CV - CV_0(t))^2 \qquad (3.7)$$

where the position CV_0 in which the potential is applied is usually relocated at a constant velocity. From the application of this potential, a work or a force profile can be obtained, given by the exploration of a region of the *CV* phase space, usually not accessible in classical MD. The work profile is given by

$$W = \int_{0}^{t_{CV}} dt \frac{\partial H_{biased}(\vec{x}, \vec{p}, t)}{\partial t} \tag{3.8}$$

in which the Hamiltonian of the system (eq. 3.6), function of the microscopic coordinates of the system, is modified with respect to the one of the unbiased MD (H_{MD}), via the following:

$$H_{biased}(\vec{x}, \vec{p}, t) = H_{MD}(\vec{x}, \vec{p}) + \frac{k}{2}(CV(\vec{x}) - CV_0 - vt)^2 \tag{3.9}$$

where *v* is the velocity at which the position of application of the restraint along the *CV* is moved.

Grübmuller firstly adopted the technique in a work in which compared the computed force profile with the rupture force required in atomic force microscopy experiments to study the streptavidin-biotin complex. [160] Later, Jarzynski defined the following equality:

$$\Delta\mathrm{A} \leq -k_B T \cdot ln \langle e^{-\frac{W}{k_B T}} \rangle \tag{3.10}$$

The relationship relates the irreversible work to the reversible one (i.e., the free-energy difference $\Delta\mathrm{A} \leq \mathrm{W}$), given a certain number of simulations, permitting to compute potential of mean force (PMF) profiles. [161] Schulten and colleagues devised an equation using the cumulant expansion of the previous at the second order, a formulation valid with fewer replicas and holding in stiff-spring regime. [162] In unbinding simulations, the method is usually applied to discriminate strong inhibitors from weak binders by qualitatively comparing the peak of the forces or the PMF profiles. [163] In the Thesis, SMD is mostly used to generate input geometries for other techniques used to retrieve more accurate free-energy estimates.

3.3 ADIABATIC BIAS MOLECULAR DYNAMICS

With respect to SMD, this technique exploits the thermal fluctuations of the system to progress toward higher energy states of the *CV*. Therefore, the coordinate of application of the bias potential is not moving at a given rate, but it is governed by a time-dependent potential, called pawl-and-ratchet potential, [164] responsible for updating $CV_0(t)$ with the following stepwise condition:

$$V(\varrho(t)) = \begin{cases} \frac{k}{2}\left(\varrho(t) - \varrho_{min}(t)\right)^2, & if\ \varrho(t) > \varrho_{min}(t) \\ 0, & if\ \varrho(t) \leq \varrho_{min}(t) \end{cases} \tag{3.11}$$

in which k is the force constant, $\varrho(t)$ is the square difference between the instantaneous value CV_t and the target value CV_0, while $\varrho_{min}(t)$ is the minimum value explored at time t in the simulation.

$$\varrho(t) = (CV_t - CV_0)^2 \tag{3.12}$$

$$\varrho_{min}(t) = min_{0\leq\tau\leq t}(CV(\tau) + \eta(t)) \tag{3.13}$$

in which $\eta(t)$ is an additional white noise acting on the minimum position of the bias. For low force constant values, the system perturbation given by $V(\varrho(t))$ should be small enough when compared to the total energy, therefore the system would experiment an adiabatic transformation. However, a sufficiently high force constant should be set in order to avoid receding when the harmonic bias potential is not sufficient to force the system into overcoming the last visited $\varrho_{min}(t)$.

3.4 UMBRELLA SAMPLING SIMULATIONS

In umbrella sampling (US) simulations, differently from SMD simulations, the bias harmonic restraint is kept at a fixed coordinate, therefore sampling is conducted in an equilibrium regime and multiple parallelizable windows are required to obtain an adequate sampling. This method was first developed in 1997 by Torrie and Valleau. [165] An additional energy term is added to the simulation in order to ensure the exploration of the CV phase space in the vicinity of a certain value CV_0. From the biased distribution of an ith US window, the unbiased one can be found and, therefore, the free-energy content for a specific value CV_0 can be retrieved as:

$$A_i(CV_0) = -k_B T \cdot \ln p_i(CV_0) - \Delta V_i(CV_0) + F_i \tag{3.14}$$

The equation holds assuming the ergodicity of the system and an adequate sampling of the CV. [166] Here, F_i is a constant, which is typically not important if the free-energy differences of interest are inside the explored CV space.

Application of the WHAM algorithm

Usually, to reconstruct the global free-energy profile from US simulations, the weighted histogram analysis method (WHAM) [167] is employed (Figure 13). Given the free-energy content at a specific value of CV

$$A(CV_0) = -k_B T \cdot ln\, p_{0_j}(CV_0) + F_j \tag{3.15}$$

the *a priori* probability $p_{0_j}(CV_0)$ of unrestrained MD can be reconstructed by the algorithm.

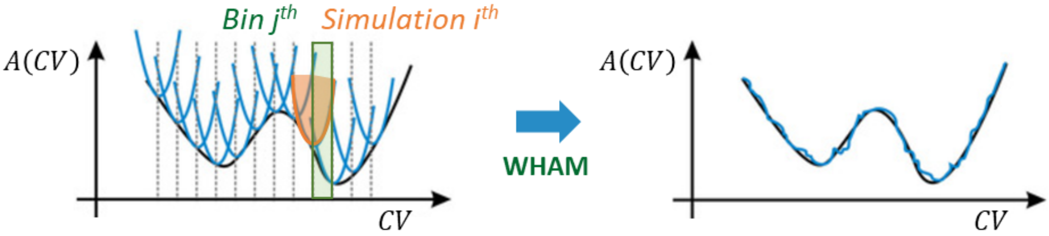

Figure 13. Pictorial representation of the application of the WHAM algorithm, in which local potentials (blue lines) of the US windows are merged into a unified PMF profile, through their overlap on a common energy scale.

The biased probability of a ith simulation to reside in specific jth bin is:

$$p_{ij} = p_{0_j} \cdot c_{ij} \cdot f_i \tag{3.16}$$

where c_{ij} is the probability distortion due to the bias potential ΔV and f_i is a normalization coeffcient. Therefore, the algorithm iteratively obtains the unbiased probability p_{0_j} by updating the value of the normalization coefficients, applying the following conditions:

$$\begin{cases} p_{0_j} = \dfrac{\sum_{i=1}^{M} n_{ij}}{\sum_{i=1}^{M}(N_i \cdot c_{ij} \cdot f_i)} \\ f_i = \dfrac{1}{\sum_{j=1}^{K}(p_{0_j} \cdot c_{ij})} \end{cases} \tag{3.17}$$

3.4.1 Path collective variables

In 2006, Branduardi et al. [168] developed a new set of *CV*s called path collective variables (PCVs), allowing for the description of complex transitions, which would be difficult to sample with simpler geometric *CV*s. This approach relies on the capability of the user to acquire a set of nodes or milestones, usually obtained via SMD in the present works. In principle, many metrics could be used for this approach. In this case, PCVs are defined via root mean square displacement (RMSD)-based variables. Therefore, as in the original implementation, two high-dimensional *CV*s ($\mathcal{S}$ and $\mathcal{Z}$) (Figure 14), defining the position of atoms included in the path with respect to a set of reference configurations ($\mathcal{R}$), are employed. The first *CV* describes the progress along the path:

$$\mathcal{S} = \frac{\sum_{i=1}^{P} i e^{-\lambda[\mathcal{R}(X-X_i)]^2}}{\sum_{i=1}^{P} e^{-\lambda[\mathcal{R}(X-X_i)]^2}} \tag{3.18}$$

The second and complementary *CV* provides the distance from the closest milestone:

$$\mathcal{Z} = -\lambda^{-1} \ln \sum_{i=1}^{P} e^{-\lambda[\mathcal{R}(X-X_i)]^2} \tag{3.19}$$

and, therefore, it is a variable that could be restrained with an upper wall potential to restrain the exploration of configurations of the system that are far from the chosen ones. $\mathcal{R}(X - X_i)$ is the RMSD between the instantaneous configuration of the atoms included in the path and the i$^{\text{th}}$ state of the frameset, and these quantities are summed over the discrete index from 1 to P.

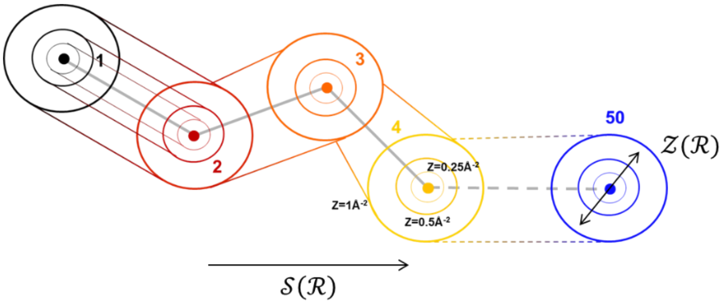

Figure 14. Pictorial representation of the path collective variables. The $\mathcal{S}$ describes the progress along a "tube reaction", while the $\mathcal{Z}$ represents the distance from the set of frames used for the definition of the path.

In both equations, the value of the *CV* is controlled by the tuneable parameter λ, which dramatically affects the definition of the PCVs phase space (Figure 15). As of rule of thumb, the λ parameter is chosen with the following relationships:

$$\lambda = \frac{2.3(P-1)}{\sum_{i=1}^{P-1}[\mathcal{R}(X_i - X_{i+1})]^2} \tag{3.20}$$

The λ value must be defined in order to ensure the smoothness over the entire path.

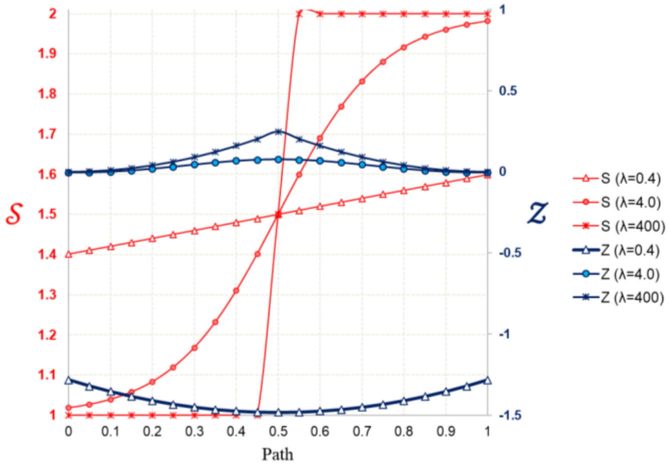

Figure 15. Impact of the λ parameter on the smoothness of path collective variables $\mathcal{S}$ and $\mathcal{Z}$ along a transition between two representative states.

With a lower λ value the definition of the *CV*s is less adherent to the frameset of the reference configurations, effectively reducing the range of explorable $\mathcal{S}$ values, while consenting the access to farther configurations on the $\mathcal{Z}$ *CV*. Instead, a λ value higher than the optimal one would lead to jumps in the exploration of the $\mathcal{S}$ *CV* and to a too restricted exploration of the $\mathcal{Z}$ *CV*.

3.4.2 PCV-US simulations

PCVs could be coupled with US simulations to increase the sampling on high energy states of the progress of a reaction or a complex conformational transition. PCV-US simulations have been used in QM-MM simulations [169,170,171], to obtain free-energy profiles combining in a single profile both products and reactants. In Chapter 4, the protocol will be proposed for unbinding simulations that are performed within classical MD regime.

3.5 METADYNAMICS SIMULATIONS

3.5.1 Metadynamics simulations: the classical implementation

Metadynamics (MetaD) is an enhanced sampling method, originally developed by Laio and Parrinello in 2002. In order to escape local free-energy minima, a history-dependent bias potential [172] is added at a constant time interval τ in the form of Gaussian potentials V with width(s) σ and height h. Each of the individual potential is centred on the coordinates in the *CV*s-space explored at the moment of the deposition. At the simulation time t and after j depositions (with $j\tau \leq t$), the total potential deposited in the point characterized by the vector *cv* in the n-dimensional space of the collective variables *CV* is represented by the following equation:

$$V(cv,t) = \sum_{j=1}^{j\tau\leq t} h_j \cdot exp\left(-\sum_{i=1}^{n} \frac{[CV_i(t) - CV_{i,j}]^2}{2\sigma_i^2}\right) \tag{3.21}$$

Therefore, the Hamiltonian of the system is changed in order to promote the transition between different free-energy minima, as represented in Figure 16. [173] This results in the flattening of the free-energy surface from which the original one is derivable by simply subtracting the deposited potential according to:

$$V(cv, t \to \infty) = -\mathrm{A}(CV) + \mathrm{C} \tag{3.22}$$

where C is an arbitrary additive constant.

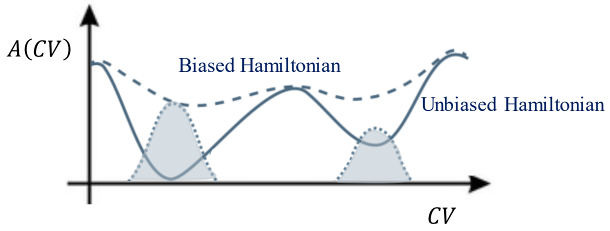

Figure 16. Representation of the MetaD repulsive potential given by the accumulation of Gaussian kernels in the sampled regions of the *CV*, resulting in a biased Hamiltonian and in the flattening of the free-energy surface, from which the unbiased Hamiltonian can be recovered.

However, the simulation could also drive the system toward non-physical high-energy configurations thus requiring the limitation of the accessible *CV*-space with restraining potentials. [173]

3.5.2 Metadynamics simulations: the well-tempered implementation

In the well-tempered implementation of metadynamics (*wt*-MetaD), [174] the height h_j in eq. 3.21 is rescaled from the initial height h_0 over time as a function of the previously deposited potential and visited coordinates with the following

$$h_j = h_0 \cdot exp\left(-\frac{V(cv, j\tau)}{k_B \Delta T}\right) \tag{3.23}$$

This adaptation of the algorithm is required to asymptotically converge toward an exact estimate of the free-energy surface, given by the following equation:

$$V(cv, t \to \infty) = -\left(1 - \frac{1}{\gamma}\right) \cdot \mathrm{A}(CV) + \mathrm{c(t)} \tag{3.24}$$

where γ is defined as the bias factor governing the Gaussian height rescaling and the convergence of the *wt*-MetaD and $\mathrm{c(t)}$ is a time-dependent constant. The bias factor γ controls the sampling temperature of the simulation in the *CV* phase space, defined by:

$$\gamma = \frac{T + \Delta T}{T} \tag{3.25}$$

for which $\Delta T \to \infty$ classical MetaD is recovered and $\Delta T = 0$ leads to unbiased sampling. If bias factor is too low, the height of the Gaussian potentials will become negligible compared to the barrier separating the free-energy basin to be explored. Instead, with a higher value, simulation will take more time to converge or would explore higher energy states, as in traditional MetaD (Figure 17).

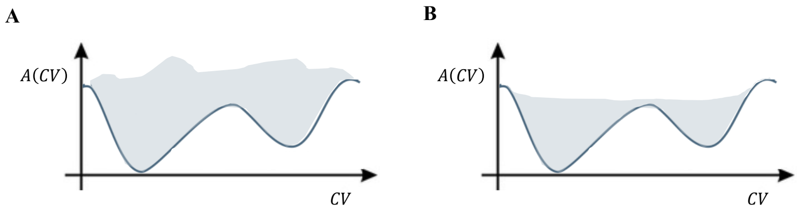

Figure 17. Comparison of MetaD in its classical (**A**) and well-tempered (**B**) schemes. The well-tempered implementation allows to avoid the overfilling of the free-energy minima, therefore smoothing the deposition of the Gaussian potentials and reducing the error.

Time-dependent criteria are used to assess the convergence of MetaD simulations [175]:

i) the *CV*(s) should be explored in a diffusive regime and with different recrossing between free-energy minima,
ii) in the well-tempered implementation, the height of the Gaussian hills should decrease over time,
iii) difference between the free-energy minima should become stationary.

3.5.3 Multiple-walker metadynamics

Multiple walker MetaD [176] consists of an implementation in which a number of replicas, sharing a common history-dependent bias, is exploring a free-energy surface characterized by the same *CV*-space and the same temperature (as opposed to the parallel tempering scheme). [177] Therefore, the bias potential deposited by all replicas concur to the calculation of the free-energy surface. The method was originally used to study the interaction of host-guest complexes and, later, for protein-ligand binding and complex protein conformational transitions. While the original algorithm employed the classical variant metadynamics, it was later expanded to the use of the *wt*-MetaD variation of the technique.

3.5.4 Free-energy reweighting

Free-energy reweighting is a technique permitting to reproject the probability distribution obtained via MetaD simulations onto any set of *CV*s without the need to perform additional simulations in which these *CV*s are biased. The approach adopted in the Thesis is the one defined by Tiwary and Parrinello in ref. 178 and applies to *wt*-MetaD. If the system reaches the equilibrium, the biased probability distribution over the system configurations x that is projected onto the CV-space is

$$P(x,t) = \frac{e^{-\frac{V(cv(x),t)-c(t)}{k_B T}}}{\int dCV\, e^{-\frac{U(x)+V(CV(x),t)}{k_B T}}} \tag{3.26}$$

where $U(\mathrm{x})$ is the system potential energy at a given configuration x and $V(CV(\mathrm{x}),t)$ is the MetaD potential deposited on the space $CV(\mathrm{x})$. The equation in turn leads to:

$$P(x,t) = P_0(x) \cdot e^{-\frac{V(cv(x),t)-c(t)}{k_B T}} \tag{3.27}$$

which relates the biased probability distribution to the unbiased Boltzmann probability density $P_0(\mathrm{x})$.

Moreover, the time-dependent constant c(t) from eq. 3.24 and 3.27 could be written as:

$$c(t) = -k_B T \cdot \ln \frac{\int dCV\, e^{-\frac{A(CV)}{k_B T}}}{\int dCV\, e^{-\frac{A(CV)+V(CV,t)}{k_B T}}} \tag{3.28}$$

where A(CV) is the projection of the free energy onto the collective variable of interest. Therefore, c(t) represents a time-dependent offset of the free-energy surface and it is interpreted as the reversible work performed by the bias potential during the simulation. However, it can be demonstrated that time-dependencies of this parameter cancel out giving a time-independent free-energy estimator. This quantity can be rewritten without any dependence on A(CV), as follows:

$$c(t) = -k_B T \cdot \ln \frac{\int dCV\, e^{\frac{\gamma}{\gamma-1} \cdot \frac{V(CV,t)}{k_B T}}}{\int dCV\, e^{\frac{1}{\gamma-1} \cdot \frac{V(CV,t)}{k_B T}}} \tag{3.29}$$

Therefore, by substituting this relationship in eq. 3.27, the unbiased distribution of the observable $\mathcal{O}(\mathrm{x})$ in MetaD simulations is recovered, as the following ensemble average:

$$\langle \mathcal{O}(x) \rangle_0 = \langle \mathcal{O}(x) \cdot e^{\frac{V(CV(x),t)-c(t)}{k_B T}} \rangle \tag{3.30}$$

3.6 ALCHEMICAL SIMULATIONS

In this type of free-energy simulations, free-energy differences are computed by producing an unphysical path connecting states A and B. At each intermediate step, the Hamiltonian will be perturbed and the introduction of multiple simulations, each one with intermediate potentials of states A and B, should increase the accuracy of the calculations, by improving the overlap in the sampling of the two phase spaces. [179] In relative binding free-energy calculations, usually free-energy differences estimators, such as thermodynamic integration, [180] are employed to compute a free-energy difference associated to a substitution of group A in group B in a ligand structure,

$$\Delta A_{BA} = A_B - A_A = -k_B T \cdot \ln \frac{Z_B}{Z_A} \tag{3.31}$$

By performing the alchemical transformation of the ligand when bound to a biological target and unbound in the solvent, a thermodynamic cycle is performed resulting in the free-energy change due to the relative binding free-energy.

3.6.1 Thermodynamic integration

Introduced by Kirkwood, [180] thermodynamic integration requires an unphysical path connecting A to B. In the approach adopted in the Amber software, the electrostatics and Van der Waals potentials, which are generally described in MD with the Coulomb and Lennard-Jones functions, are switched off and replaced with softcore potentials, [181] approximating alchemical intermediate steps in the unphysical path connecting state A to state B. These functions modelling the interaction between *i^th^* and *j^th^* particles account for:

i) replacement of the Van der Waals potentials of substituents A and B:

$$\begin{aligned} V_{\text{"}VdW\text{"}_\mathrm{A}} &= 4\varepsilon(1-\lambda)\left[\frac{1}{\left[\alpha\lambda + (\frac{\mathrm{r_{ij}}}{6})^6\right]^2} - \frac{1}{\alpha\lambda + (\frac{\mathrm{r_{ij}}}{6})^6}\right] \\ V_{\text{"}VdW\text{"}_\mathrm{B}} &= 4\varepsilon\lambda\left[\frac{1}{\left[\alpha(1-\lambda) + (\frac{\mathrm{r_{ij}}}{6})^6\right]^2} - \frac{1}{\alpha(1-\lambda) + (\frac{\mathrm{r_{ij}}}{6})^6}\right] \end{aligned} \tag{3.32}$$

ii) decharge and recharge of the atomic partial charges of substituents A and B, respectively:

$$
\begin{aligned}
V_{"Coul"_{\mathrm{A}}} &= (1-\lambda)\frac{q_1 q_j}{4\pi\varepsilon_0\sqrt{\beta\lambda + r_{ij}^2}} \\
V_{"Coul"_{\mathrm{B}}} &= \lambda\frac{q_1 q_j}{4\pi\varepsilon_0\sqrt{\beta(1-\lambda) + r_{ij}^2}}
\end{aligned}
\tag{3.33}
$$

The calculation would acquire the free-energy difference between states A and B through the modification of the Hamiltonian made by these softcore potentials in single step calculations [182]:

$$H_{biased}(\vec{x},\vec{p},t) = H_{MD}(\vec{x},\vec{p}) + V_{TI}(\vec{x},\lambda) \tag{3.34}$$

with a λ-dependent potential, represented by potentials in eqs. 3.32 and 3.33.

$$V_{TI}(\vec{x},\lambda) = \lambda V_A(\vec{x}) + (1-\lambda)V_B(\vec{x}) \tag{3.35}$$

Substituting the potential in the expression of the Helmholtz free-energy (eq. 3.3) and differentiating with respect to the coupling parameter, one obtains the following:

$$\frac{dA}{d\lambda} = \frac{1}{Z}\int e^{-\frac{H_{biased}}{k_B T}}\frac{\partial V_{TI}}{\partial\lambda}dpdq = \langle\frac{\partial V_{TI}(\vec{x},\lambda)}{\partial\lambda}\rangle_\lambda \tag{3.36}$$

since derivative with respect to the coupling parameter only affects V_{TI}. Therefore,

$$\Delta A = A(x,\lambda_B) - A(x,\lambda_A) = \int_{\lambda_A}^{\lambda_B}\langle\frac{\partial V_{TI}(\vec{x},\lambda)}{\partial\lambda}\rangle_\lambda\, d\lambda \tag{3.37}$$

which is the free-energy difference between the two alchemical states A and B, graphically represented in Figure 18.

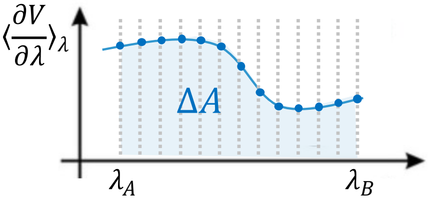

Figure 18. Graphical representation of the free-energy change depending on the coupling parameter λ.

The integral can be computed numerically by simulating the systems at different λ values in multiple simulations. In the study performed in Chapter 6, 12-point gaussian quadrature [183] was used for the numerical integration performed on $\frac{\partial V}{\partial\lambda}$ ensemble averages.

Chapter 4. Free-energy simulations investigating 2-iodomelatonin unbinding from MT_1 receptor through a lipophilic binding route

4.1 INTRODUCTION

4.1.1 Binding kinetic of melatonin receptor ligands

Radioligand binding assays, consisting in the displacement of a radiolabelled ligand by the compound under evaluation, are usually performed to obtain an estimation of binding affinity, but can also provide binding kinetic parameters of GPCRs ligands. [184] Such experiments have been performed by Servier industries [185] to assess the association and dissociation rate constants of [^{3}H]-melatonin and 2-[^{125}I]-melatonin at the two melatonin receptors. Measurements of the residence time of the two ligands at the MT$_1$ receptor quantitatively agreed with the ones reported by Takeda industries. [186] Moreover, it is reported for the two radiolabelled compounds that the residence time would be prolonged at the MT$_2$ receptor, [185] as observed for alternative radioligands analogously requiring a longer time to dissociate from the MT$_2$ receptor. [148] In the case of 2-[^{125}I]-melatonin, [113] which is the radioligand of election for the characterization of melatonergic ligands, no dissociation could be seen in 3-4 hours experiments performed at the MT$_2$ receptor. [185] While a quantitative measurement of the dissociation rate constant at the MT$_2$ receptor could not be provided, these experiments show that indeed ligands could dissociate with a slower rate from the MT$_2$ receptor. Given the impact of kinetic parameters on drug activity, [187] it is interesting to understand if the binding/unbinding pathways followed by ligands at the MT$_1$ and MT$_2$ receptors might influence their residence time which, in turn, could be the determinant of receptor subtype selectivity.

4.1.2 Impact of mutagenesis on binding affinity and residence time

Different amino acid mutations [75] have been introduced to study the impact of residues bordering the proposed channels through which melatonergic ligands would reach the binding site. Mutations to alanine of residues bordering the TM channel (see Figure 7, in the Introduction) would more greatly decrease the residence time of melatonin at the MT$_2$ receptor than at the MT$_1$ receptor. In particular, mutation of Y187/200$^{5.38}$ to alanine reduced the residence time of melatonin more at the MT$_2$ receptor. Conversely, mutation of A158/171$^{4.56}$ to methionine would in turn increase the residence time by preventing ligand exit from the orthosteric binding site, while leading to a reduction in the functional activity. [74]

Finally, removal of TM helix IV kink, potentially obstructing the lipophilic channel, through mutation of P174$^{4.59}$ to glycine or alanine would lead to abolition of affinity of melatonin at the MT$_2$ receptor. [83] Therefore, the influence of residues, bordering the TM channel between the helices IV and V, on binding affinity and residence time, has been shown by mutagenesis experiments. More subtle could be the role of a proposed hydrophilic gateway to the extracellular solvent, as mutations of T178/191^{ECL2}, Q181/194^{ECL2} and Y281/294$^{7.39}$ [75] would affect the binding site as well, even considering that the second residue is directly engaged to the amide group of melatonin with a hydrogen bond.

Given the lipophilic character of melatonin [188] and most of the melatonergic ligands, and the number of lipid GPCRs [90] presenting entryways to the orthosteric site through TM channels, simulations are run to explore the viability of such a lipophilic pathway for melatonin receptors. Unbinding trajectories, in which 2-iodomelatonin is pulled out from melatonin receptor binding sites, are produced with SMD simulations. Then, a low-energy path is sampled with a protocol based on PCV-US simulations in order to retrieve a reliable free-energy cost. The aim is to evaluate the viability of a lipophilic route describing the ligand entrance/exit, eventually comparing the results with the experimental data and possibly rationalizing the different binding kinetics at the two melatonin receptors.

4.2 COMPUTATIONAL PROTOCOLS

4.2.1 Molecular dynamics simulations

MT$_1$ and MT$_2$ receptor structures, obtained from X-ray crystal structures of complexes with 2-iodomelatonin and 2-phenylmelatonin (PDB id *6ME4* [74] and *6ME6* [75], respectively) were prepared according to the protocol reported in the Appendix I. 2-phenylmelatonin was replaced with 2-iodomelatonin at the MT$_2$ receptor. Complexes between MT$_1$ receptor and compound **12** (Figure 12) [152] and UCM1341 [189] were retrieved via docking calculations performed at the MT$_1$ receptor bound to 2-phenylmelatonin (PDB id *6ME3* [74]) with Glide 7.9 [190,191] and minimized with MacroModel 12.0, [192] using OPLS3e force field. [193] The three protein-ligand complexes were embedded in a 1-palmitoyl-2-oleyl-*sn*-glycerol-3-phosphocholine (POPC) bilayer via the Charmm-GUI server [194] and then solvated in a TIP3P water box [195] of about 81x81x107 Å. The systems were parametrized with ff14SB

Amber Force Field [196] and the ligands parameters were assigned from the general Amber force field (GAFF). [197] Lipid17 was employed to parametrize the lipid bilayer. Neutrality for each system was achieved by adding 16 and 10 chloride ions to the MT_1 and MT_2 boxes, respectively, assigning parameters from ref. 198. Partial atomic charges of 2-iodomelatonin were computed with Jaguar 10.0 [199,200] through a RESP calculation [201] at the Hartree-Fock level in gas-phase using LACV3P* basis set, while the 6-31G* basis set was employed for compound **12**.

Molecular dynamics (MD) simulations were performed using Gromacs 2019.2. [202] Biased simulations were conducted by patching the MD code with Plumed 2.5.4. [203] Long-range electrostatics were computed with the Particle Mesh Ewald method [204] with a Fourier scheme adopting fourth order interpolation and 1.6 Å grid spacing, while short-range and Lennard-Jones interactions were computed with a 10 Å cutoff. Bond lengths of hydrogens with heavy atoms were restrained to their equilibrium values through the LINCS algorithm [205] to permit an integration timestep of 2 fs. MD simulations were performed in canonical ensemble at 298 K, controlled under the Nosé-Hoover thermostat [206,207] with a coupling constant of 0.5 ps. An isotropic force constant of 0.1 $\text{kcal}\cdot\text{mol}^{-1}\cdot\text{Å}^{-2}$ was applied to a set of 89 backbone carbons restrained to their position in the crystal structures to preserve the TM bundle far from the binding site, while consenting the flexibility of the upper portion of TM helices during ligand unbinding. The list of the restrained backbone atoms included five carbons at the truncated *N*-terminus and the α carbons located in the three innermost turns of every TM helix.

4.2.2 Preliminary unbinding simulations via SMD simulations

Twenty simulations were performed for each receptor complex to evaluate the unbinding process through the opening between TM helices IV and V. A *CV* was designed to describe the distance of the centre of mass (COM) of the indole heavy atoms of 2-iodomelatonin from the η plane defined by the three COMs obtained from selected α carbons of TM helices IV and V (H1, H2 and H3 in Figure 19), according to the following eq.:

$$d(COM_{indole}, \eta) = \frac{a \cdot X_{COM_{indole}} + b \cdot Y_{COM_{indole}} + c \cdot Z_{COM_{indole}} + d}{\sqrt{a^2 + b^2 + c^2}} \tag{4.1}$$

where a, b, c and d are the coefficients of the implicit equation of the η plane.

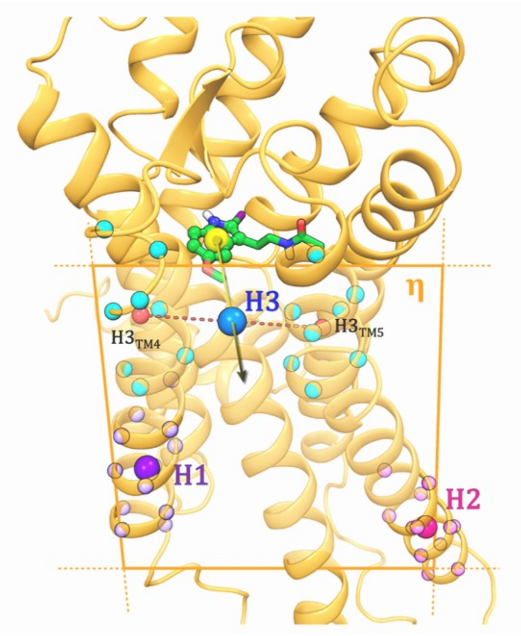

Figure 19. Definition of 2-iodomelatonin (green sticks, indole heavy atoms are visualized as spheres) **unbinding *CV* $\mathbf{d(COM_{indole},\eta)}$**, (represented by the black arrow) **from the $\mathbf{MT_1}$ receptor** (orange cartoon) **binding site**. The motion of the center of mass of the indole heavy atoms (yellow sphere) is described with respect to the η plane, which is defined through three COMs: H1 (purple sphere) is the center of the restrained α carbons of the TM IV, H2 (pink sphere) is the center of the restrained α carbons of the TM V and H3 accounts for unrestrained α carbons belonging to the extracellular sides of both TM IV and V helices. The distance showed in red between the two COMs of the α carbons used for the definition of H3 and belonging to the two different TM helices is used to monitor the flexibility of the TM channel.

During the first 100 ps of simulation, the moving harmonic restraint was linearly increased to 50 kcal·mol^{-1}·Å^{-2} on $d(COM_{indole},\eta)$ = -8 Å, which is the unitary value of the *CV* closest to the equilibrium position of the centre of mass of the indole observed during 100 ns of MD simulation, in which all the α carbons were restrained. After this initial phase, the harmonic restraint was moved in stiff-spring approximation regime from $d(COM_{indole},\eta)$ = -8 to 12 Å during 30.0 ns.

4.2.3 Path optimization procedure

Path optimization [169] procedure was performed through four iterative 30 ns-long SMD simulations [160] in which a restraint of 50 kcal·mol^{-1} was applied along the $\mathcal{S}$ *CV*. An additional upper wall with a force constant of 1,000 kcal·mol^{-1}·Å^{-4} was placed at $\mathcal{Z}$=1 Å^2 to restrict the exploration of configurations of the system distant from the iteratively updated reference framesets. Each frameset included atoms, represented in Figure 20, accounting for the movement of the ligand and of the upper portions of TM helices IV and V, and aligned according to optimal alignment matrix, calculated through the Kearsley algorithm. [208] In these simulations, λ was tuned to assure a smoother transition between values of the progress CV ($\mathcal{S}$=1-38) corresponding to configurations, in which the ligand is bound to the receptor, and considering the highest inter-frame distance between these pairs of frames.

Between each of the four PCV-SMD runs, the iterative update of the reference frameset was performed employing in-house scripts. A procedure applying the Catmull-Rom splines method [209] was utilized to generate additional configurations to refine the guess path, by interpolating the SMD trajectories through the insertion of ten intermediate graphs between each pair of consecutive SMD frames. The 50 reference configurations were then extracted by computing an RMSD-distance matrix of the frameset, through an operation based on the Nudged Elastic Band (NEB) algorithm; [210] in this protocol, Monte Carlo sampling was employed to obtain configurations optimally describing transition states regions. [211] Ten iterations of the procedure were performed using a Metropolis coefficient of 10,000, keeping the endpoint configurations fixed. After the four PCV-SMD runs, further optimization of the frameset was achieved through targeted dynamics simulations setting as a collective variable the RMSD difference between the configurations at the ends of each range, in the spirit of ref. 212.

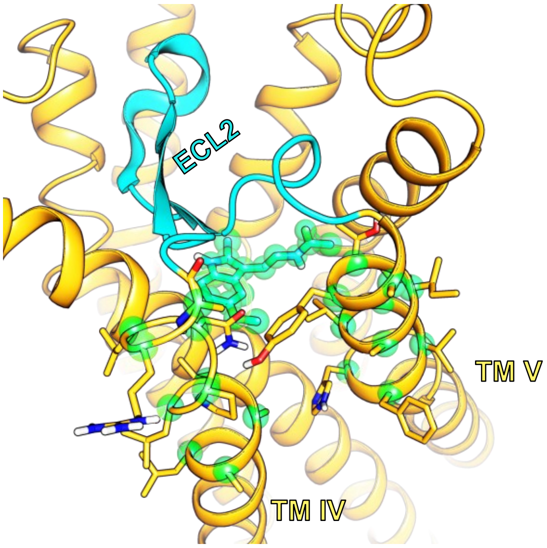

Figure 20. Representation of the atoms included in the PCVs definitions. MT_1 receptor is represented with orange cartoon, except for ECL2 in cyan, obstructing the entrance to the binding site from the top of the receptor. The selection of atoms (green spheres) for PCVs includes 2-iodomelatonin heavy atoms and select α carbons belonging to TM helices IV (L156$^{4.54}$-A165$^{4.63}$) and V (A186$^{5.37}$-H195$^{5.46}$).

4.2.4 PCV-US calculations

The final frameset obtained through four consecutive pulling simulations was retained, after the last three PCV-SMD runs giving similar work profiles, and used for PCV-US simulations. Before simulations, a restraint on the $\mathcal{Z}$ *CV* was placed at $\mathcal{Z} = 0.25$ Å^2 applying a force constant linearly increasing from 5 to 1,000 kcal·mol^{-1}·Å^{-4} in a 1 ns simulation, while the force constants at unitary values of $\mathcal{S}$ were linearly reduced from 50 kcal·mol^{-1} to 5 kcal·mol^{-1}. The Weighted Histogram Analysis Method (WHAM) [167] was used to reconstruct the free-energy values at binned intervals of the $\mathcal{S}$ *CV*. A harmonic restraint with a spring of 5 kcal·mol^{-1} was kept for 50 ns for each of the $\mathcal{S}$ unitary values, using a smoothing parameter λ=6.936 Å^{-2}. To ensure the overlap of neighbouring US windows in which a high free-energy derivative was found, simulations with $\mathcal{S}$=2-5,8 were rerun twice, once with a spring constant of 5 kcal·mol^{-1}, as the other US windows, and once with a spring constant of 10 kcal·mol^{-1}. Convergence of simulations is checked with different criteria, reported in Appendix II.

4.2.5 Metadynamics simulations protocols

Opening of Tyr187/200$^{5.38}$

MetaD simulations adopting the well-tempered implementation [174] have been performed sampling χ_1 dihedral angle. The bias potential was deposited with a rate of 3 ps using Gaussians set with a width of 3° and an initial height of 0.2 kcal·mol^{-1}. The bias factor, controlling height rescaling, was set to 15.

Additionally, 2D MetaD simulations were performed on χ_1 and χ_2 dihedral angles. To avoid the sampling of symmetric degrees of freedom, χ_2 dihedral angle was compactified in a $[0,\pi]$ interval through a Heaviside function. In this case, all the protein α carbons were restrained, instead of the previous list of 89 backbone atoms. The Gaussian were deposited every 5 ps and widths were set in the two dimensions to 5° and 10°. The initial height was maintained fixed to 0.2 kcal·mol^{-1}, while the γ parameter was doubled with respect to 1D MetaD simulations.

4.3 RESULTS AND DISCUSSION

4.3.1 Free-energy simulations support a lipophilic binding route for melatonin receptors

Unbinding of 2-iodomelatonin from MT_1 and MT_2 receptors was initially studied through the use of multiple SMD simulations. The ligand was pulled out from the binding site in the direction of the hydrophobic cleft between the TM helices IV and V and toward the lipid bilayer, as described in Figure 19. Each SMD trajectory followed a slightly different unbinding path, despite the restraint over all protein α carbons, therefore hampering a direct comparison between the two receptor subtypes. The registered work profiles at the two receptors (Figure 21.A-B) led to unfeasible free-energy contents not compatible with the free-energy relatable to radiolabelled ligand residence times. Therefore, no energetic analysis of these trajectories was further considered to compare the two receptor subtypes.

However, these simulations provided geometries utilizable as starting points for US calculations in equilibrium conditions and permitted to draw initial hypothesis. In all SMD simulations, 2-iodomelatonin crossing the channel between TM helices IV and V caused an increase in the distance between the extracellular side of the same helices, as defined in Figure 19 and monitored in Figure 21.C-D. By the end of the simulations, the width of the TM cleft returned as the value of restrained plain MD simulation, which in turn is analogous to the one of X-ray crystal structures.

Given the unreliability of the free-energy estimate to access the lipophilic route via SMD simulations, a more reliable and accurate free-energy barrier for 2-iodomelatonin receptor unbinding was obtained using geometries extracted from a specific SMD trajectory and adopting equilibrium free-energy calculations. Therefore, one of the unbinding trajectories was selected for the MT_1-2-iodomelatonin complex (run #14, black line in Figure 21.A), according to the lowest average work (~28.1 kcal·mol^{-1}) measured at a CV value corresponding to the indole ring transiting outside of the cleft between the TM helices ($d(COM_{indole}, \eta)$ = 3 Å), a step of the unbinding process that is expected to require the highest free-energy change.

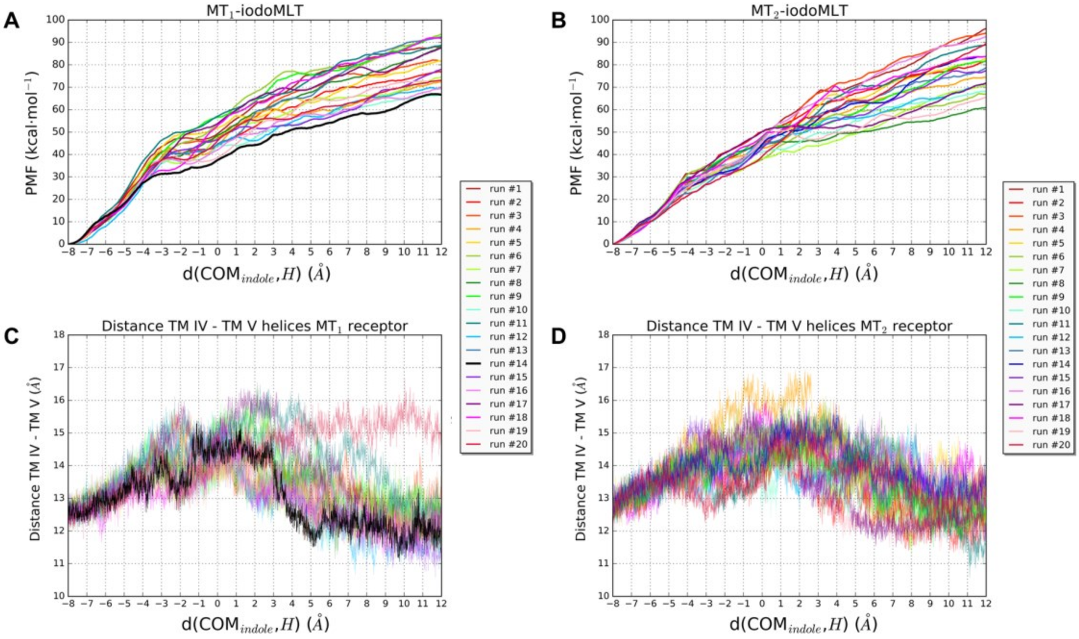

Figure 21. Work profiles obtained as potential of mean force (PMF) curves from SMD simulations and time series registering the distance between TM IV and V helices. PMF curves are reported for SMD simulations to model the unbinding of 2-iodomelatonin from the MT$_1$ receptor (**A**) and from the MT$_2$ receptor (**B**). Distance between TM helices IV and V is monitored over the *CV* describing the unbinding of 2-iodomelatonin from the MT$_1$ receptor (**C**) and from the MT$_2$ receptor (**D**). The COMs selected for the two TM helices are showed in *Figure 19* as red spheres. The run #14 for the MT$_1$ receptor, used for PCV-US simulations, is evidenced with a black wider curve on the left panels.

The selected SMD trajectory was utilized to extract fifty reference configurations of the frameset required for the definition of the PCVs, described in Paragraph 4.2.3, and accounting in its definition for the movement of both the protein and the ligand atoms (Figure 20). Four PCV-SMD runs were performed and the work profile was stabilized on similar values in the last pulling simulations (Figure 22). Therefore, the fourth run was used to extract new reference configurations for PCV-US simulations.

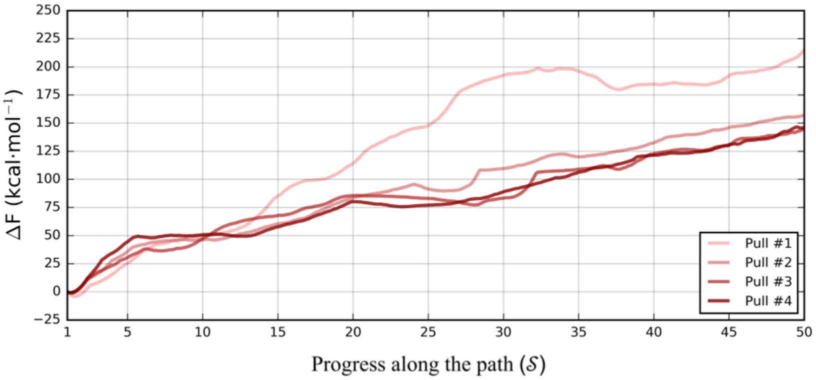

Figure 22. Work profiles obtained through PCV-SMD runs. Iterative pulling simulations are performed on the $\mathcal{S}$ variable. while restricting the access to configurations with a high $\mathcal{Z}$ value.

To estimate the unbinding free energy, PCV-US simulations were performed, consisting of 50 ns of MD simulations restrained at each $\mathcal{S}$ unitary value. In total, counting US windows repeated with a higher constant, the simulation time amounts to 2.75 μs. The reliability of the obtained free-energy profile is assessed through different criteria that are reported in Appendix II.

The highest free-energy barrier encountered by the ligand consists of ~23 kcal·mol^{-1} and it represents the transition from the bound state ($\mathcal{S}$=1, Figure 23.A) to a high-energy state in which 2-iodomelatonin is inserting between the two TM helices ($\mathcal{S}$=5, Figure 23.B), while still undertaking the hydrogen bond with Q181$^{\mathrm{ECL2}}$. After that, the ligand indole ring passes between TM helices IV and V, in a configuration characterized by a free energy decrease ($\mathcal{S}$=9-14). The indole nitrogen could interact via hydrogen bonds with V159$^{4.57}$ ($\mathcal{S}$=10, Figure 23.C) and A158$^{4.56}$ ($\mathcal{S}$=13, Figure 23.D), favouring the egress and the subsequent rotation of the indole ring inside the TM channel.

A more prominent free-energy minimum is located at $\mathcal{S}$=26 (Figure 23.E), in which the ligand resides at the protein-membrane interface with the indole ring outside of the cleft, in which the alkylamide chain still resides. Near the indole, the aromatic side chain of Y187$^{5.38}$ assumed an open conformation, possibly concurring to ligand stabilization. A plateau region follows, corresponding to the unbound ligand in the membrane lipid bilayer ($\mathcal{S}$=50, Figure 23.F).

The calculated barrier of around 23 kcal·mol^{-1} for 2-iodomelatonin dissociation from the MT$_1$ receptor is similar to ~25 kcal·mol^{-1} obtained from the experimental $k_{\mathrm{off}} = 2.41 \cdot 10^{-4} s^{-1}$ of 2-[^{125}I]-iodomelatonin at 25 °C [185], derived from an application of the Eyring equation of transition-state. [213] According to the theory, the free-energy difference would depend on the kinetic constant with the following:

$$\Delta A^{\ddagger}_{\mathrm{off}} = RT \ln \frac{k_B T}{h k_{\mathrm{off}}} \qquad (4.2)$$

where T is the absolute temperature and h is the Planck's constant.

Although this estimate corresponds to the free-energy cost for one out of many possible unbinding trajectories, our simulation supports the viability of a lipophilic route for melatonergic ligands, indicating at least one low-energy path connecting the bound conformation of 2-iodomelatonin to the unbound conformation in the lipid bilayer. Besides, PCV-US simulations have underlined two aspects of the unbinding process deserving further investigation, involving the free-energy minimum located at $\mathcal{S}$=26 and the role of Y187$^{5.38}$ into assisting ligand egress and recognition.

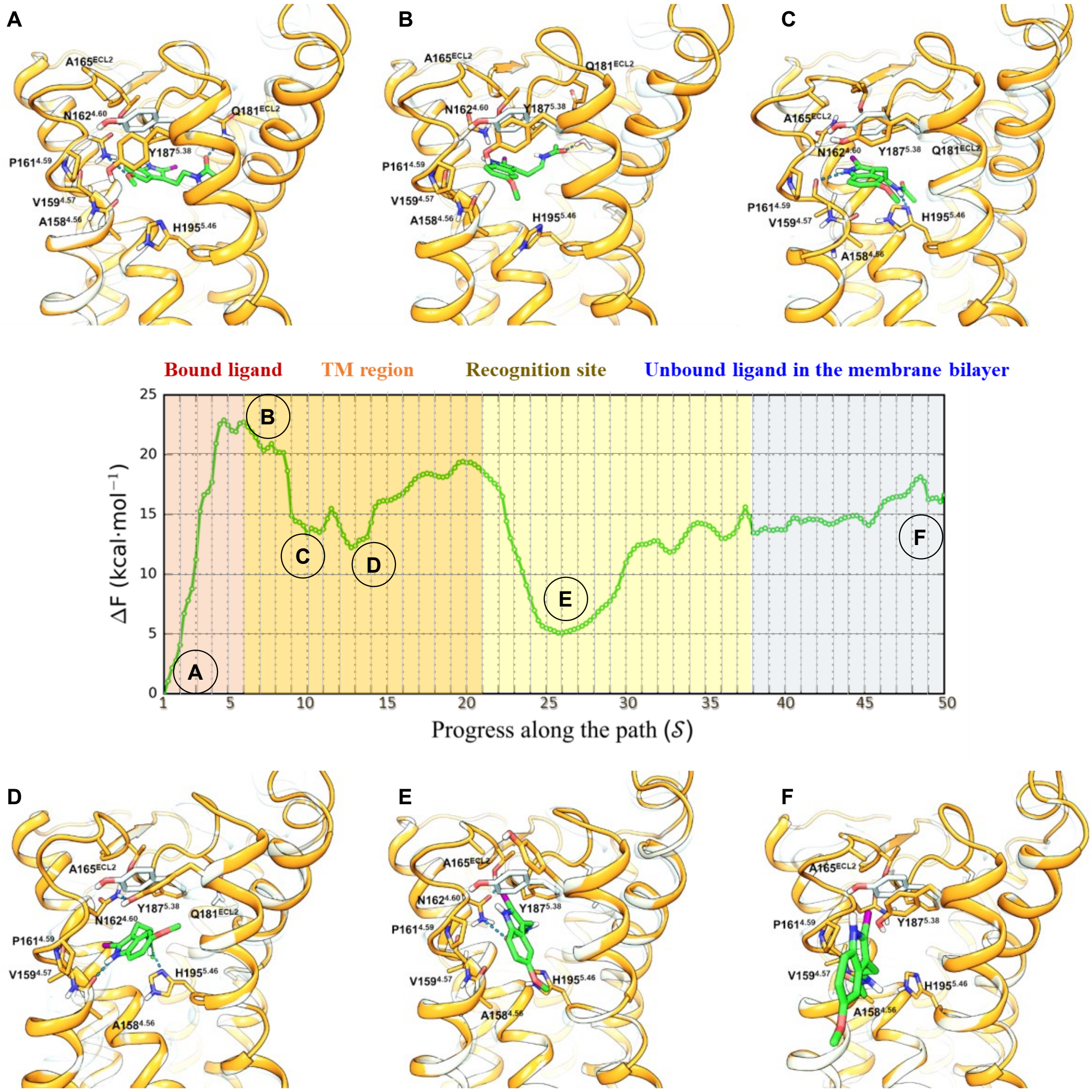

Figure 23. Free-energy profile of 2-iodomelatonin unbinding from the MT$_1$ receptor from PCV-US simulations. The different stages are reported with different colours. Snapshots retrieved from PCV-US simulations evidence the ligand unbinding process at different values of $\mathcal{S}$: (**A**) at $\mathcal{S}$=1, bound ligand; (**B**) at $\mathcal{S}$=5, the ligand exiting the binding site; the ligand inserted in the lipophilic channel between TM helices IV and V, with the indole interacting with (**C**) V159$^{4.56}$ ($\mathcal{S}$=10) and (**D**) A158$^{4.56}$ ($\mathcal{S}$=13); (**E**) at $\mathcal{S}$=26, the ligand with the ethylamide chain bound in the recognition site; and, (**F**) at ($\mathcal{S}$=50), the ligand unbound in the membrane bilayer. Protein white cartoon and sticks representing Y185$^{5.38}$ are shown to compare the snapshots with the X-ray crystal structure (PDB id *6ME4*). Hydrogen bonds are shown with blue dashes.

4.3.2 Characterization of a recognition site for melatonergic ligands

The free-energy minimum located at S=26 (Figure 23.C) could be interpreted as a site for the recognition event, promoting ligand recruitment from the membrane prior to the binding process through the TM channel. Starting from the PCV-US window restrained at this S value, an unbiased MD simulation lasting 200 ns was performed, in which 2-iodomelatonin could stably interact through the amide group with polar residues surrounding the hydrophobic channel (Figure 24), namely N162$^{4.60}$, responsible for the hydrogen bond with the methoxy group when the ligand is bound in the crystal's conformation, and H195$^{5.46}$. The last residue is conserved at both receptors and might be important for receptor activation [52] and ligand binding affinity [94,95]. During the unrestrained simulation, the 2-iodo substituent was located near the aromatic ring of Y187$^{5.38}$ in its open conformation.

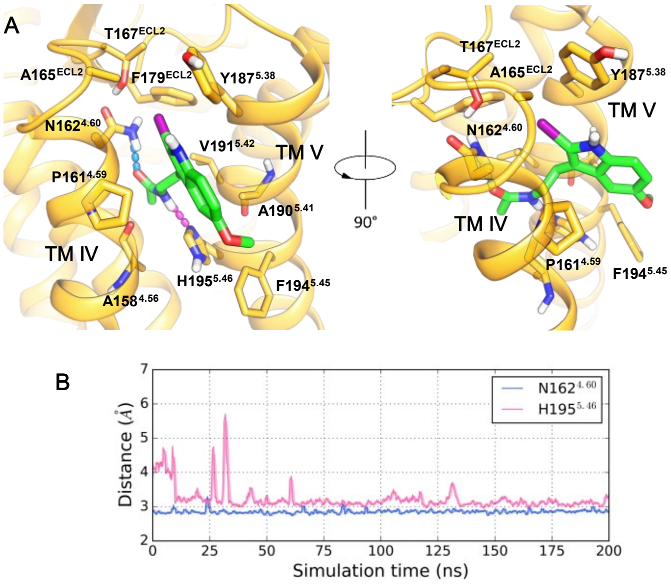

Figure 24. Recognition site of 2-iodomelatonin at the MT$_1$ receptor (**A**) in the crevice between the TM helices IV and V. Stability in MD of the polar interactions (**B**) between the receptor (N162$^{4.60}$ and H195$^{5.46}$) and 2-iodomelatonin.

Evidence offered by spectroscopic measurements [188] and results provided by MD [214] and MetaD simulations [215] had shown that, due to its physicochemical properties, melatonin would be concentrated within the membrane in the proximity of the boundary between polar heads and the lipophilic core composed by the acyl chains. Thus, adsorption on the surface of TM helices IV and V could favour the access of a ligand to the orthosteric binding site through the channel between these helices. This can account for the potency gain observed for more lipophilic melatonin receptor ligands and, within this hypothesis, the design of novel ligands should consider physicochemical properties accounting for the partition of the compounds in the lipid phase. Concentration at the interface of the membrane would enhance ligand recognition by turning the diffusion into a 2D-process increasing the probability of target engagement. [216] Moreover, as seen in ref. 215 and later in Chapter 5, the interface could enrich the bioactive conformation of the flexible alkylamide chain of melatonergic ligands.

4.3.3 A gatekeeper residue as a determinant for the residence time of melatonergic ligands

In SMD trajectories, an important qualitative difference emerged between 2-iodomelatonin unbinding at the two receptors. The sidechain of Y187/200$^{5.38}$ had a different behaviour during simulations and it could access more frequently the "open state" (χ_1~300°, cyan background in Figure 25.A) in the MT$_1$ receptor than in the MT$_2$ receptor, in which a "closed state" (χ_1~180°, red background in Figure 25.B) was generally preferred. In fact, while in half of SMD simulations at the MT$_1$ receptor the tyrosine opened upon the crossing of 2-iodomelatonin in the TM channel, in just three out of twenty simulations at the MT$_2$ receptor, the tyrosine could access the open state.

In experimental structures of melatonin receptors, Y187/200$^{5.38}$ has been observed in both conformations at both receptors, [74,75,96,87] as described in Paragraph 2.3 (see Figure 7). Since simulations were started from X-ray crystal structures, the initial conformations corresponded to the "open state" at the MT$_1$ receptor and the "closed" one at the MT$_2$ receptor. However, oftentimes, in unbiased MD simulations, including the one used to retrieve the structure input for SMD simulations, Y187$^{5.38}$ adopted a close conformation at the MT$_1$ receptor, even if starting from the open one. Indeed, the conformational landscape of this residue could be independent from the functional state of the receptor, since the wide conformational changes between active and inactive states are mostly concentrated on the intracellular portions of TM helices VI and VII, as a consequence of the interaction with the G_i protein. Moreover, superposition of the extracellular portions of the structures evidence the similarity between the inactive agonist-bound and active conformations, as previously seen for other class A GPCRs. [217]

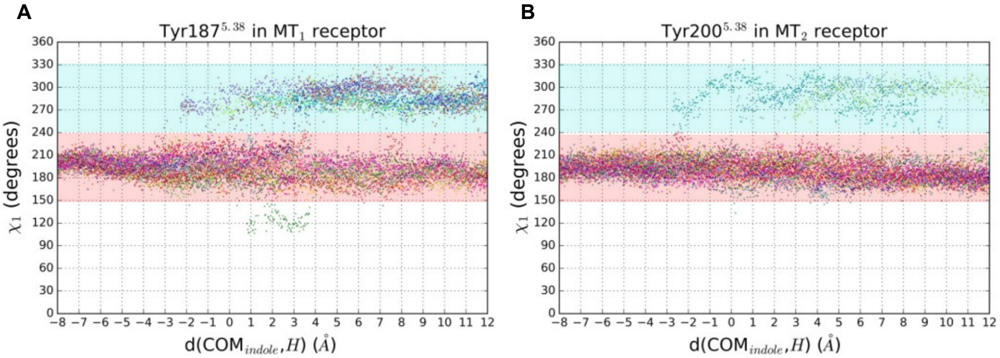

Figure 25. Analysis of Y187/200$^{5.38}$ χ_1 dihedral angle during SMD simulations at the MT$_1$ (**A**) and MT$_2$ (**B**) receptors, respectively. The dihedral angle is monitored as a function of the unbinding *CV*. The "closed state" is represented by the area highlighted in red, while the "open state" is highlighted in cyan. Each dot colour represents a different SMD run.

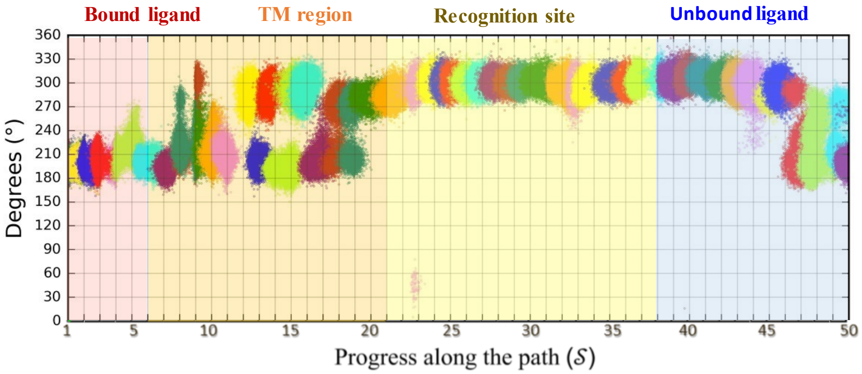

Figure 26. Conformation of Y187$^{5.38}$ χ_1 dihedral angle in PCV-US simulations, describing the unbinding of 2-iodomelatonin from the MT$_1$ receptor. The dihedral angle is registered every 2 ps and each colour represents a different PCV-US window.

In our model, the reference frameset, adopted for PCV-US simulations, was retrieved from an SMD trajectory with Tyr187$^{5.38}$ able to access the open state. As a matter of fact, during ligand unbinding, the side chain was steadily kept open during the PCV-SMD optimization as well as in PCV-US simulations, at S coordinates in which the ligand is exiting through the lipophilic channel (Figure 26), until the very end of the unbinding path when the residue returned to a closed conformation.

Finally, the conformational preference of Y187/200$^{5.38}$ at the two receptors was evaluated via *wt*-MetaD simulations [174] in which the χ_1 dihedral angle was used as the *CV*. Since simulations resulted in highly variable results, for each receptor subtype twenty runs were simulated and average free-energy profiles were obtained (Figure 27). Probability distributions of twenty independent free-energy surfaces were averaged and, therefore, the normalized probability P_{ij} for the system during the i^{th} simulation to be found in the 3°-wide j^{th} bin was obtained from the corresponding free-energy profile via:

$$P_{ij} = \frac{e^{-\frac{A_{ij}}{k_B T}}}{\sum_{j=1} e^{-\frac{A_{ij}}{k_B T}}} \qquad (4.3)$$

where A_{ij} is the free energy calculated in MetaD simulations for the centre of the j^{th} bin and a normalization condition was applied to every centre of the bin. The averaged free energy associated to this coordinate is computed with the following:

$$A_j = -k_B T \cdot \ln \overline{P_j} \pm k_B T \cdot \frac{\sigma_{\overline{P_j}}}{\overline{P_j}} \qquad (4.4)$$

where $\overline{P_j}$ is the average of the normalized probability distributions of all the simulations and the term $\pm k_B T \cdot \frac{\sigma_{\overline{P_j}}}{\overline{P_j}}$ represents the free-energy uncertainty, computed as the S.E.M. of the different probability-averaged free-energy profiles.

Focusing on the MT$_1$ receptor, the open (χ_1~300°) and closed (χ_1~180°) states have comparable free-energy values, with the closed state slightly favoured by ~1 kcal·mol^{-1}. This state is characterized by the TM channel being restricted through the formation of hydrogen bonds (Figure 27.A) between the tyrosine hydroxyl group and either the carbonyl backbone of A158/171$^{4.56}$ or the amide sidechain of Q162/175$^{4.60}$. At the MT$_2$ receptor, simulations evidenced that the closed state is clearly preferred due to a free-energy difference of ~4 kcal·mol^{-1} (Figure 27.B-C).

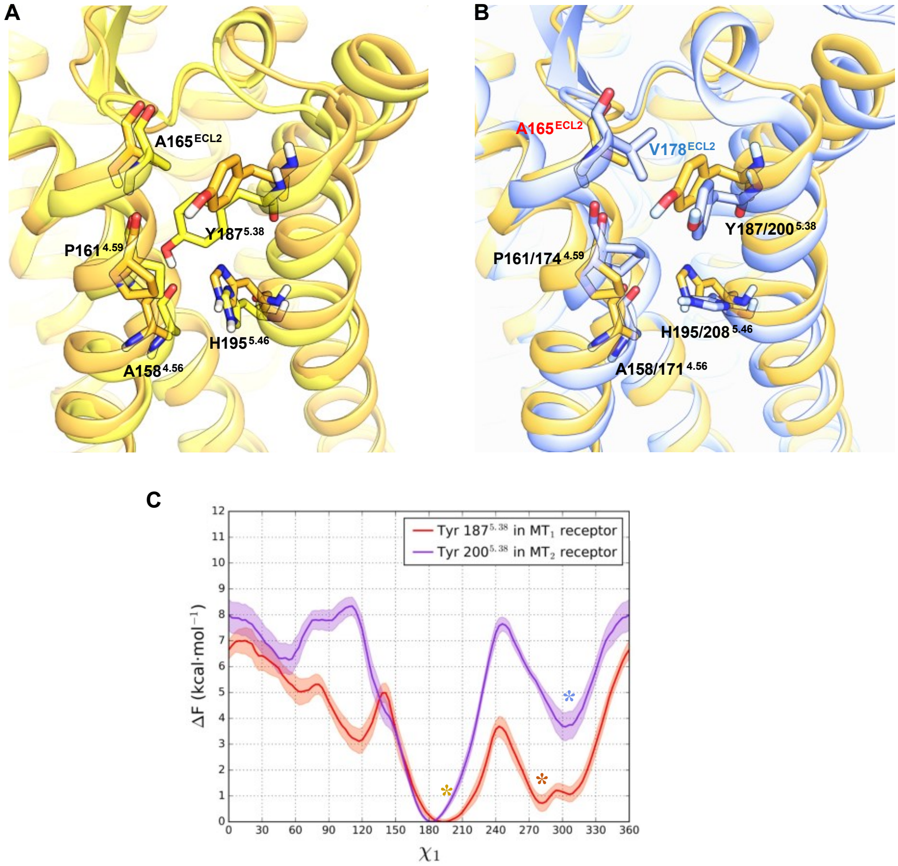

Figure 27. Analysis of MetaD simulations sampling the conformation of Y187/200$^{5.38}$. Representative conformations of the "closed state" (yellow ribbons and sticks) and the "open state" (orange ribbons and sticks) of the tyrosine at the MT$_1$ receptor are extracted from *wt*-MetaD simulations (**A**). The conformation of the two "open state" at the two receptors are compared (**B**, MT$_1$ receptor in orange and MT$_2$ receptor in blue) and the residues A165/V178 are evidenced on the extracellular tip of the TM helix IV. Free-energy profiles due to χ_1 dihedral rotation in *wt*-MetaD simulations (**C**, orange for the MT$_1$ receptor and purple for the MT$_2$ receptor). The shaded region represents the uncertainty of the FES given by ±S.E.M. Asterisks represent the values of χ_1 for the Y187/200$^{5.38}$ conformations presented in the panel.

Structural comparison of the two receptor subtypes in snapshots extracted from MetaD simulations and with Y5.38 being in the open conformation (Figure 27.B) evidence that the presence of a different residue belonging to the ECL2 might hamper the opening of the residue at each system. A165 at the MT_1 receptor is substituted by the bulker V178 at the MT_2 receptor, resulting in a higher free-energy content for the open conformation. These results are coherent with mutagenesis performed on $Y187/200^{5.38}$ since mutation to alanine causes a more evident reduction of [^{3}H]-melatonin residence time at the MT_2 receptor (30-fold vs 4-fold decrease, observed for the MT_1 receptor). [75]

To support these results, additional simulations were performed to enhance the rotation of the phenol group of $Y187/200^{5.38}$ by biasing another *CV*, and the higher free-energy content of the open state at the MT_2 receptor was as well confirmed (Figure 28).

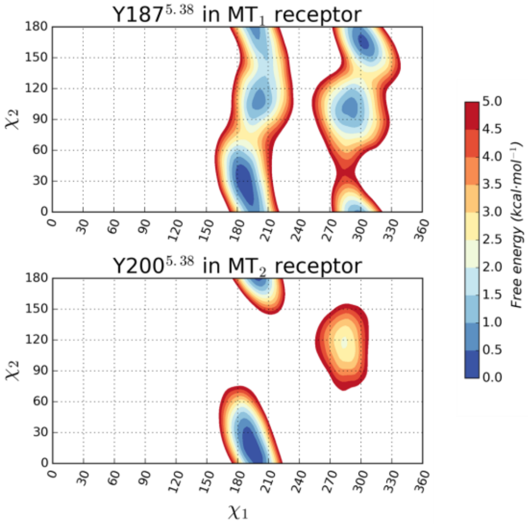

Figure 28. FES obtained via 2D *wt*-MetaD simulations sampling the conformation of $Y187/200^{5.38}$. Opening of the tyrosine at the MT_2 receptor is more impeded than at the MT_1 receptor, at which the open state is located at a lower free-energy value compared to MT_2 receptor.

Less clear is the role of $N162/175^{4.60}$, that would be stabilized in the binding site by the closed state of $Y187/200^{5.38}$, therefore increasing ligand binding mode stability and the residence time. Mutagenesis experiments alternatively showed a greater importance of the residue for MT_1 functional activity with respect to the other receptor subtype [74,87] or a limited impact on the G-protein dissociation. [96]

4.3.4 The recognition site can accommodate substituents leading to mild MT_1 subtype selectivity or dual-target activity

While many compounds with selectivity for the MT_2 receptor have been devised, and structural requirements to achieve MT_2 selectivity are more clarified (as reported in the Chapter 2 and as it will be discussed in Chapter 6), molecular determinants to achieve this level of selectivity at the MT_1 receptor are not well understood.

The highest probability associated in simulations to the open state of Y5.38 in the MT_1 receptor would allow for the generation of transient configurations able to facilitate ligand binding/unbinding and its interaction with the lipophilic TM channel. This hypothesis, in principle, would be relevant even for bitopic ligands that would be able to bind this allosteric region with their extended portions. [218] Such interactions would be particularly strong with aromatic substituents able to potentially engage Y5.38 aromatic ring through π-π interactions. The long alkyl substituents replacing the 5-methoxy group in MT_1-selective ligands, usually leading to mild MT_1-selectivity, could permit the harbouring of lipophilic groups at the receptor-membrane interface and the establishment of the stacking interactions with $Y187^{5.38}$.

Among MT_1-selective ligands, compound **12** (Figure 12) carries a peculiar feature, [152] being an agomelatine derivative functionalized with a biphenyl-carboxylate moiety at the end of the recurring alkyl chain. It achieved the highest selectivity to date at the MT_1 receptor ($K_i(MT_1)$=0.55 nM against $K_i(MT_2)$=51.30 nM). Due to the carboxylate group, the compound is characterized by an increased polarity with respect to the other ligands sharing the alkyl substituent replacing the methoxy group.

Docking studies at the MT_1 receptor place the biphenyl-carboxylate portion inside the membrane, protruding from the ligand binding site through the opening between the TM helices IV and V, as proposed for the docking of the agomelatine derivative CTL-01-05-B-A05 [74], therefore supporting these derivatives as bitopic compounds able to simultaneously occupy both the orthosteric site and this extended region in the TM cleft.

MD simulation, through the opening of Y187$^{5.38}$ (closed during system equilibration), allowed the accommodation of the biphenyl-carboxylate from the inner portion of the membrane bilayer, where it was placed by docking calculations, to the polar outer layer.

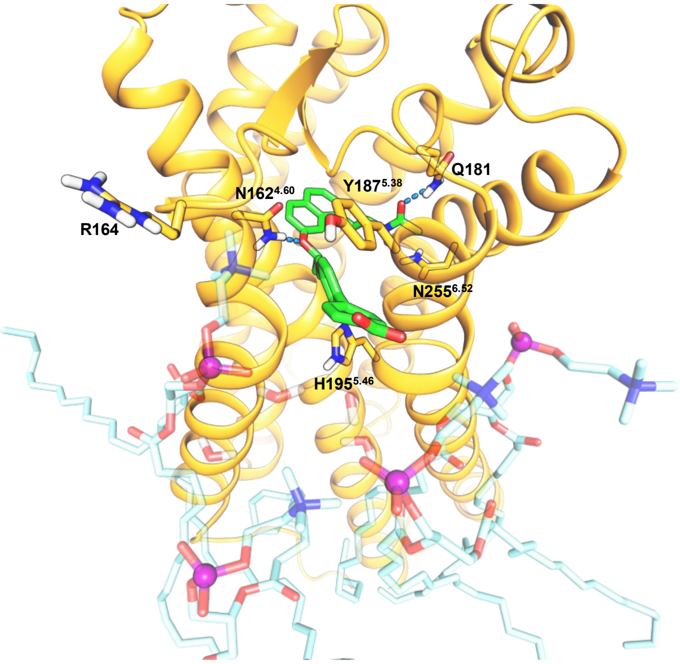

Figure 29. Interaction in MD simulation of the complex between the MT$_1$ receptor (orange cartoon and sticks) with biphenylcarboxylate group of compound **12** (green sticks) with polar component of the membrane.

Here, the carboxylate group could interact with the choline trimethylammonium heads, directly or through bridging water molecules placed at the membrane-solvent interface. Thus, interaction of the biphenyl-carboxylate with the polar components of the membrane (Figure 29) would be made viable by the open state of Y5.38, which is in turn more likely at the MT$_1$ receptor. Weak π-π interactions between the aromatic groups of MT$_1$-selective compounds and the tyrosine can still be found in MD simulations performed with all-atom force fields. [219] The interaction of the ligand with Y187$^{5.38}$ in its open state would account for the increased selectivity with respect to its neutral analogue, [152] by enabling the additional interaction with polar components of the membrane-solvent interface. Interestingly, the anionic portion of MT$_1$-selective ligands could possibly undertake a salt-bridge with R164 at the cytoplasmic tip of TM IV, replaced by F177 at the MT$_2$ receptor.

Favourable contacts of polar substituents with the membrane-solvent interface or with protein residues could be exploited to obtain peripherally restricted agents devoid of biological effects at the CNS.

The protein-membrane interface could also be useful to design dual-acting compounds, in which the pharmacophore for the second target can either interact with the recognition site or remain inside the membrane bilayer. This might be the case for compounds bearing a moiety for inhibition of FAAH enzymatic activity, [189] possibly eliciting neuroprotective effects. Docking of UCM1341 (Figure 30), a compound promoting inflammation resolution in rats, [220] at the MT_1 receptor shows that the *O*-biphenyl-carbamate moiety, [221] responsible for FAAH inhibition, would be accommodated at the recognition site, with the carbamate group interacting with $H195^{5.46}$, similarly to the proposed binding mode of CTL-01-05-B-A05. [74]

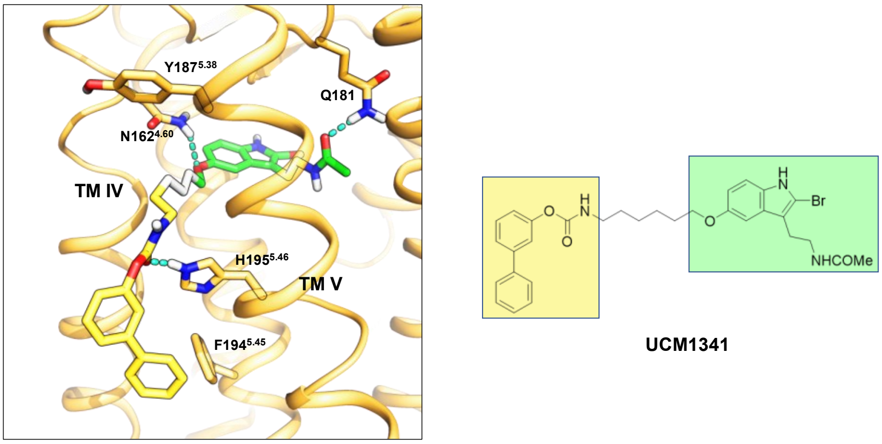

Figure 30. Docking of UCM1341 at the MT_1 receptor (orange cartoon and sticks, PDB id *6ME3*). 2-bromomelatonin scaffold is represented in green sticks, separated from *O*-biphenyl-carbamate (i.e., the portion inhibiting FAAH enzymatic activity, in the figure represented in yellow sticks) by an alkyl linker (white sticks), passing in the cleft between TM helices IV and V. Hydrogen bonds are represented with cyan dashed lines.

4.4 CONCLUSIONS AND FUTURE PERSPECTIVE

The likelihood of a lipophilic pathway for class A GPCRs ligands is supported by a number of currently available crystal structures, including sphingosine-1-phosphate receptor, [222] endocannabinoid receptors, [223] free fatty acid receptors [224] and even serotonin receptors, [225] in which crevices between the TM helices would account for the direct connection between the lipid bilayer and the orthosteric site, permitting the entrance of lipids acting as receptor agonists or modulators.

In this work, computational evidence that such lateral access is possible even for melatonin receptor ligands has been provided. In fact, through a lateral channel between TM helices IV and V, ligand unbinding from the orthosteric binding site, located in the 7-TM bundle, to the membrane is supported by free-energy simulations coupled to MD simulations. Simulation of the unbinding process for 2-iodomelatonin in complex with the MT_1 receptor provided a calculated energy barrier compatible with the experimental dissociation rate constant, [185] thus supporting the viability of the overall process. Convincing points emerging from these simulations include the presence of a recognition site and the (questionable) rationalization of mutagenesis experiments performed by different research groups, involving residues which have a substantial impact on melatonin residence time. [75]

The recognition site would be common to the two receptors, since it would be generated by conserved amino acids surrounding the lipophilic entrance, and with whom the ligand would be able to engage in energetically favourable transient arrangements, as previously proposed for other GPCRs ligands. [226,227] These additional binding sites, called metastable sites, have been suggested as targets for allosteric ligands. [228] In the case of the β_2-adrenergic receptor, the additional portions belonging to bitopic compounds interact with an extended portion of the orthosteric site toward the ECL2 and the upper portion of the receptor. [229] Recently, many compounds have been proposed to bind TM clefts, possibly acting as bitopic compounds as in the case of dual-steric CB_2 receptor agonists. [230,231] MetaD simulations at this receptor showed the binding of JWH-133 to the receptor through metastable states. [232] As well, simulations support this possibility for melatonin receptors, at which the region called “recognition site” could serve as an extension of the orthosteric binding site able to accommodate moieties belonging to bitopic compounds. Moreover, this additional interaction site would be preferential for MT_1-selective ligands. This difference would be, to a certain level, related to the conformational space of Y5.38 at the two receptors, being the access to the "open state" more hindered at the MT_2 receptor.

The tyrosine could be seen as a "gatekeeper" residue acting a critical role in discriminating kinetic binding parameters for melatonergic ligands. However, its importance as a residue leading to subtype selectivity could not be related to the modulation of kinetic parameters, since a conformational preference for the closed state would negatively impact on both association and dissociation rate constants, as well as the open state would equally promote ligand access and egress.

Instead, as in the case of compound **12**, the open state would enable additional interactions at the protein-lipid interface, eventually even with components of the membrane bilayer, [233] accounting for the (limited) selectivity of MT_1-selective agonists. While simulations gave interesting insights of the unbinding mechanism, additional biophysical experiments could still validate the hypothesis of the ligand entry through a TM channel. [234]

Structure-based drug design could be exploited to model docking hypothesis for bitopic ligands, as in the case of UCM1341. The moiety occupying the allosteric site would confer a second pharmacological activity, as multi-target compounds have been thoroughly considered for the treatment of CNS conditions. [235]

Chapter 5. Conformational selection driving the stereoselectivity of potent melatonergic agonists

5.1 INTRODUCTION

5.1.1 Alkylamide chain bioactive conformation of melatonergic ligands

Initial *in silico* approaches to drug discovery of melatonergic compounds consisted of ligand-based studies, including the use of pharmacophore models and/or 3D-QSAR CoMFA analysis. These models were exploited for the design of new compounds and, at the same time, provided hints of the bioactive conformation of melatonin. Two pharmacophore models provided by Jansen et al. [236] and Spadoni et al. [237] indicated a bioactive conformation of melatonin in which the acetylaminoethyl side chain was outside and perpendicular to the indole ring plane. Additionally, these models agreed on having an *anti* arrangement of the ethylene bond of the ethylamide chain, later confirmed by stereoselective analogues (Figure 31) in which the ethyl portion was constrained into a 1,2-trans cyclopropyl ring, as compound **14**. [130]

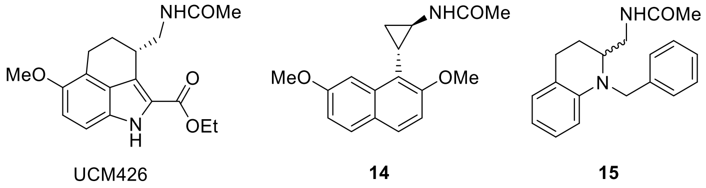

Figure 31. Compound in which the alkylamide chain has been rigidified or partially constrained into aliphatic cycles.

While agreeing on the orthogonal arrangement of the alkylamide chain with respect to the indole ring, the pharmacophore models could be satisfied by opposite arrangements of the alkylamide chain with respect to the aromatic nucleus. The availability of stereoselective chiral compounds allowed to define the orientation of the ethylamide chain in the bioactive conformation. Depicting the methoxy group on the left side, a below-the-plane arrangement was confirmed by superposition with the potent stereoselective tetrahydrobenzo-indole (*S*)-derivative, UCM426, in which the ethylamide chain was partially constrained and assumed an axial arrangement, confirmed by X-ray diffraction studies. [132] The refined pharmacophore model was also able to unambiguously match the arrangement of ramelteon, being the (*S*)-derivative.

This finding led to the development of tetrahydroquinoline derivatives, through the rigidification of the *N*-anilinoethylamide scaffold with a partial constraint of the alkylamide chain in the form of a ring closure. One of the most potent and MT_2-selective compound, UCM1014, belongs to this class. While UCM1014 was assayed as a racemic mixture, enantiomerically pure species (with unassigned chirality) of the de-methoxy acetylamino methyl derivative **15** (UCM936) were also tested, evidencing a stereoselective behaviour. Therefore, on the basis of the superimposition of the energetically favoured axial arrangement of the propionylaminomethyl side chain to the bioactive conformation of UCM426 (Figure 32), (*R*)-UCM1014 was predicted as the eutomer. [123]

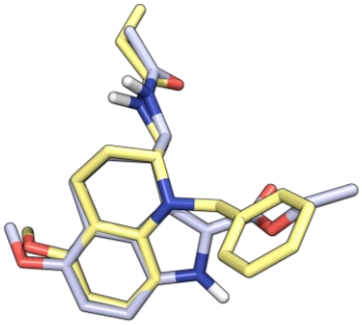

Figure 32. Superimposition of the constrained analogues UCM426 and (*R*)-UCM1014.

5.1.2 Role of chiral substitutions on the alkylamide chain

Different substitutions of the ethylamide chain were performed in initial studies including indole derivatives. [238] One of the most clinically advanced compounds is TIK-301, (*R*)-β-methyl-6-chloro-melatonin (Figure 33), which is characterized by a higher binding affinity, [108] and metabolic stability, than melatonin and was evaluated by Ely Lilly in trials for the treatment of circadian rhythm sleep disorders.

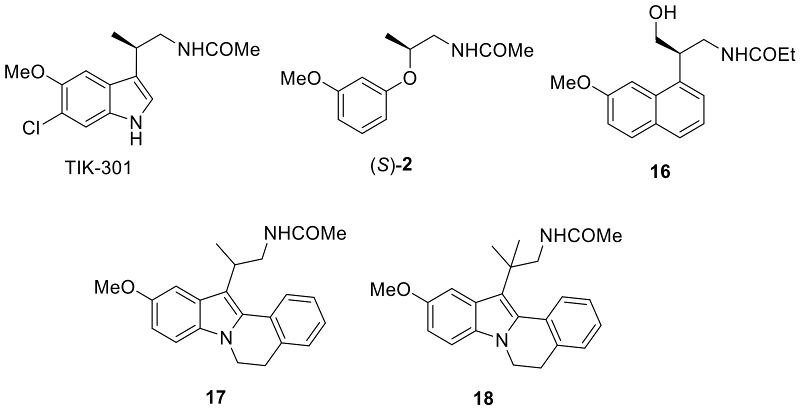

Figure 33. Compound in which the β-position of alkylamide chain has been modified through the insertion of different substituents.

The introduction of substituents at the β position of the acylaminoethyl chain was also evaluated by Servier industries on agomelatine derivatives. The methyl and the fluoromethyl groups led to an increase in the binding affinity [239] and introduction of the β-hydroxymethyl substituent gave compound **16**, for which the (*R*)-stereoisomer proved to be the eutomer. [240]

The positive effect on the binding affinity given by the insertion of the β-methyl substituent was additionally observed on other classes of compounds, in which the indole ring was replaced with bioisostere scaffolds, such as the *N*-[2-(3-methoxyphenoxy)ethyl]acetamides and their thio-analogues. For both series of compounds, as later discussed in Paragraph 5.2.5, the eutomer was found having an (*S*)-configuration. [116]

Given the conserved behaviour of mono-substituted compounds at the β-position, it could be speculated that the introduction of substituents on the alkylamide chain could result in stereoselective agonists due to an increase of the abundance of the bioactive conformation(s). In this Chapter, MD simulations, studying the interplay of the conformational equilibria in of the ligand in the solvent and bound to receptor, will be employed to understand enantioselectivity of β-methyl substituted compounds.

5.2 RESULTS AND DISCUSSION: β-METHYL-DERIVATIVES OF MELATONIN BIOISOSTERES

5.2.1 Biological activity of chiral N-anilinoethylamides

Chiral N-anilinoethylamides were evaluated for their binding affinity, in which the radiolabelled 2-iodomelatonin was displaced, and intrinsic activity, through GTPγS assay, on human melatonin receptors MT_1 and MT_2 stably expressed by NIH3T3 cells. [81,241] Results in Table 1 are obtained via the collaboration with University of Milano.

The α-methyl derivative **19** racemate revealed a considerable binding affinity decrease at both receptors compared to the parent compounds, UCM793. This drop in the affinity, similar to what has been previously seen for phenoxyethylamide derivatives [116], dissuaded from further introduction of substituents at this position. Conversely, the β-methyl derivative UCM1183 showed binding affinity and agonist activity at both receptors comparable to those of UCM793. Therefore, enantiomers of UCM1183 were separately prepared with a stereoselective synthesis [242] in collaboration with the University of Urbino and the (*S*)-derivative gave a binding affinity ten times higher than the (*R*)-derivative at both receptor subtypes.

Table 1. Biological activity of methyl-substituted chiral N-anilinoethylamides

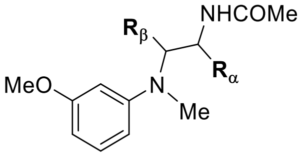

Compound	R_α	R_β	MT_1		MT_2	
			pK_i (±SD) [a]	IA (±SD) [b]	pK_i (±SD) [b]	IA (±SD) [b]
Melatonin	--	--	9.60 ± 0.18	1.00 ± 0.09	9.44 ± 0.12	1.00 ± 0.07
UCM793	H	H	8.76 ± 0.18	0.95 [c]	8.65 ± 0.01	1.06 [c]
UCM1183	H	Me	8.67 ± 0.01	0.98 ± 0.06	8.77 ± 0.02	1.01 ± 0.07
(*R*)-UCM1183	H	Me	7.59 ± 0.02	1.00 ± 0.07	7.91 ± 0.04	0.99 ± 0.08
(*S*)-UCM1183	H	Me	8.88 ± 0.08	0.98 ± 0.11	8.96 ± 0.11	1.01 ± 0.10
19	Me	H	8.17 ± 0.02	n.d.	7.98 ± 0.08	n.d.

[a] pK_i values were calculated from IC_{50} values, obtained from competition curves by the method of Cheng and Prusoff [243], and are the mean of at least three determinations performed in duplicate. [b] Relative intrinsic activity values were obtained by dividing the maximum analogue-induced G-protein activation by that of melatonin. Measurements were performed in triplicate. [c] Ref. 117.

5.2.2 Interactions of UCM793 β-methyl derivatives within the MT$_2$ receptor binding sites

Compounds (*S*)-UCM1183 and (*R*)-UCM1183 were docked into the crystal structure of the MT$_2$ receptor [75], given the slightly higher binding affinity for this subtype over MT$_1$. The best binding modes obtained for the two enantiomers, represented in Figure 34, had similar GScore values (-8.602 kcal·mol^{-1} for (*S*)-UCM1183 and -8.413 kcal·mol^{-1} for (*R*)-UCM1183), conserving polar interactions usually undertaken by melatonergic ligands. Both enantiomers had their methyl group positioned in a similar region of the binding pocket, surrounded by mainly hydrophobic amino acids, comprising V124$^{3.36}$, I125$^{3.37}$, V204$^{5.42}$ and W264$^{6.48}$, and a polar residue, i.e., N268$^{6.52}$.

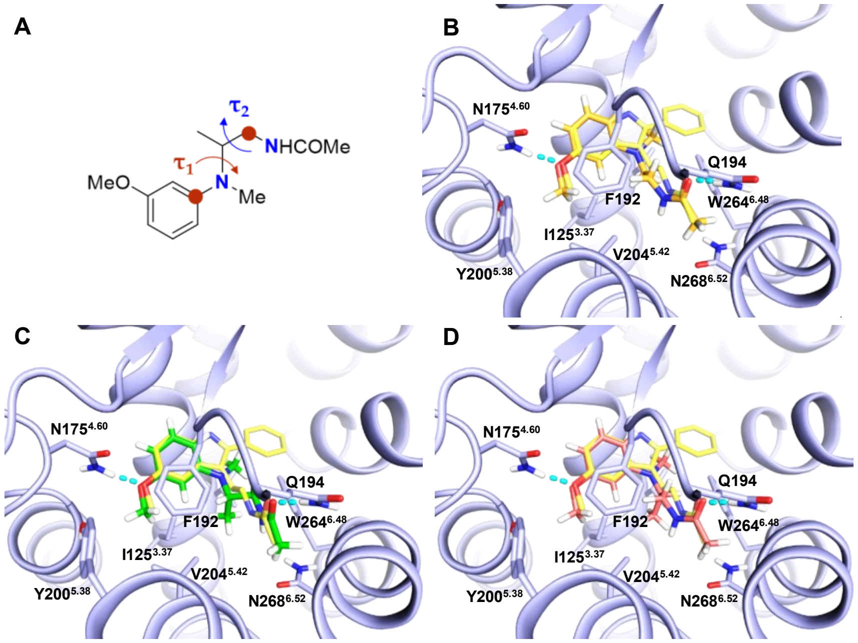

Figure 34. Representation of dihedral angles used to project FES of N-anilinoethylamides in solution (**A**). Docking poses within MT$_2$ receptor binding site (purple cartoon and sticks) of UCM793 (**B**), (*S*)-UCM1183 (**C**) and (*R*)-UCM1183 (**D**). 2-phenylmelatonin, co-crystalized in MT$_2$ receptor (PDB id *6ME6*), is shown with yellow sticks. Hydrogen bonds are represented with cyan dashes. A portion of the TM V and of the ECL2 has been omitted for clarity.

While the methoxy and the acetamide groups both kept similar interactions, the dihedral angles of the alkylamide chain (as defined in Figure 34) assumed different values in order to place the β-methyl group in the same position. MM-GBSA calculations were used to rescore docking poses, resulting in very similar values for the two enantiomers (−59.02 for (*S*)-UCM1183 and −57.76 kcal·mol^{-1} for (*R*)-UCM1183), indicating that slight gain of affinity of the (*R*)-compound is not driven by a better accommodation due to the favourable interaction with the surrounding residues. After energy minimization of the complexes obtained via docking calculations, dihedral angles τ_1 and τ_2 assumed for the eutomer, (*S*)-UCM1183, were τ_1=−135° and τ_2=177°, while (*R*)-UCM1183 had values τ_1 =−52° and τ_2=−174°.

The dynamic stability of the MT$_2$-ligand complexes was evaluated with 150 ns of MD simulations, in which the hydrogen bonds usually established by melatonergic ligands are maintained, i.e., the hydrogen bond between the methoxy group of the ligand and the amide group of N175$^{4.60}$ and between the amide of the flexible side chain and the amide sidechain of Q194^{ECL2}. While dihedral angle τ_1 oscillated around the value found in docking calculations of both enantiomers, τ_2 assumed two different values (Figure 35), both consenting the formation of the hydrogen bond between the amide group and Gln194^{ECL2}.

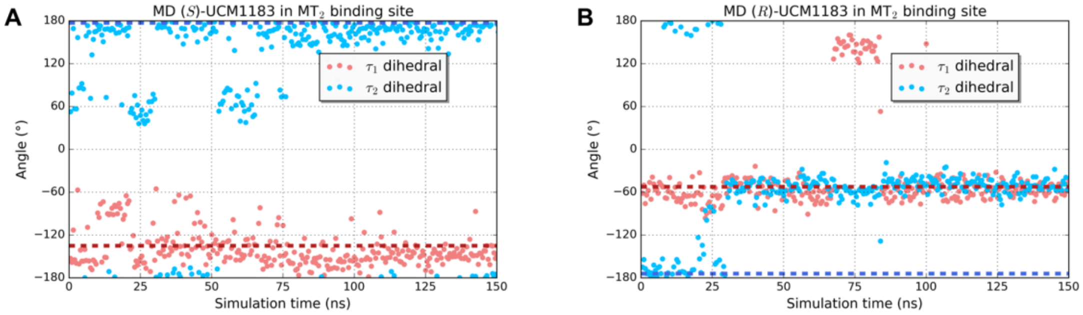

Figure 35. Time-series of dihedral angles τ_1 and τ_2 during MD simulations of (*S*)-UCM1183 (**A**) and (*R*)-UCM1183 (**B**) within the binding site of MT$_2$ receptor.

Thus, the evidence collected via docking simulations, free-energy endpoints calculations and unbiased MD within the receptor suggested that the slight gain of affinity could not be related to a better accommodation within the binding site. Therefore, MD simulations of the unbound UCM1183 enantiomers are done to assess if the conformational abundance of the bioactive conformer in the solvent is higher for one of the two compounds.

5.2.3 Impact of the β-methyl substituent on the conformational equilibria

To assess the conformational space of UCM1183 enantiomers in solution, a 2-μs-long MD simulation in a box of explicit chloroform was performed for each compound. The eutomer had a global free-energy minimum corresponding to $\tau_1=-150°$ and $\tau_2=60°$. Given the property of enantiomers, the same result, with specular angle values, was obtained with MD simulations for the distomer, with most populated conformations at $\tau_1=150°$ and $\tau_2=-60°$ (Figure 36). From the obtained probabilities and resulting free-energy values, it appeared that the introduction of the β-methyl substituent focalized the free-energy surface of the progenitor compound, UCM793, into two specular free-energy surfaces, in which values corresponding to the docking poses are placed on different free-energy levels. Docking conformation of the eutomer corresponds to a relatively low-energy point, obtaining a free-energy difference of ~3.0 $\text{kcal}\cdot\text{mol}^{-1}$ with respect to the global free-energy minimum, while for the distomer the bound conformations was not accessed at all in free MD simulation in solution.

Therefore, the insertion of the β-methyl group could alter the conformational equilibria of the unsubstituted precursor and induce a conformational selection, which could favour selected conformations.

The results of MD simulations for UCM1183 were consistent with those of experimental NMR studies performed at the University of Urbino. The spectrum of UCM1183 was obtained for the racemic mixture in $CDCl_3$ at 600 MHz and all peaks were assigned to protons.

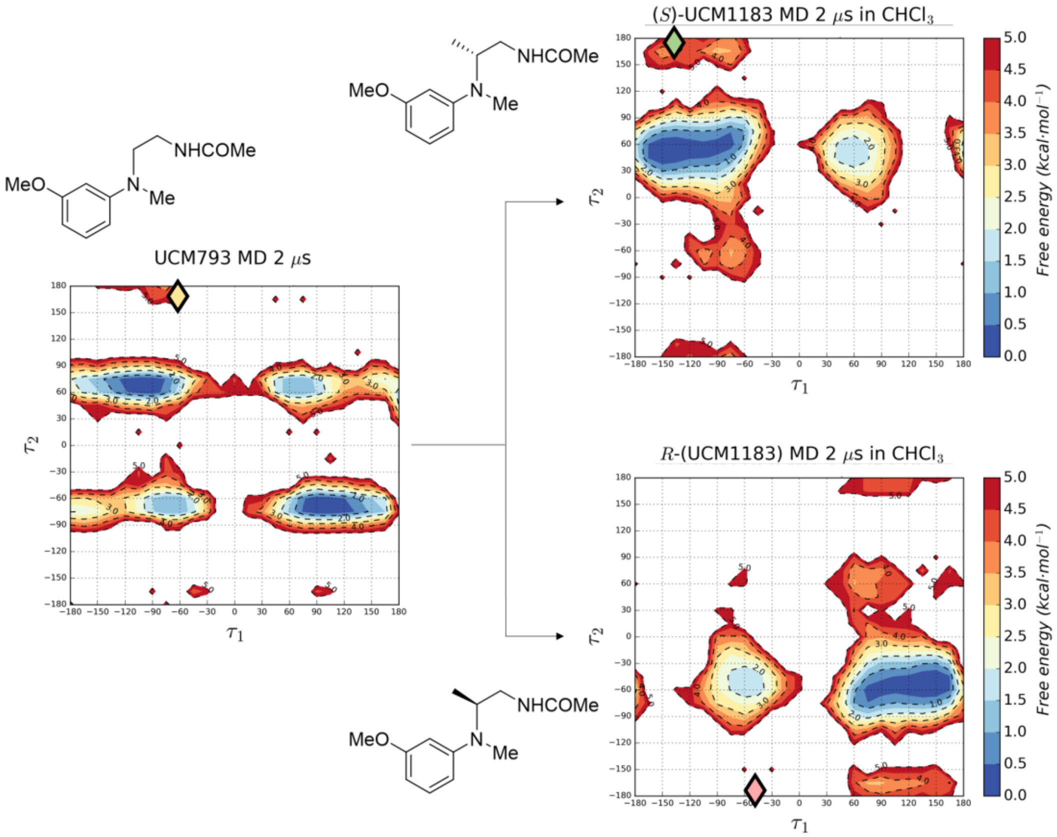

Figure 36. Free-energy surfaces of the unbound UCM793 and UCM1183 enantiomers are obtained via unbiased MD simulations performed in a box of explicit chloroform, lasting 2 µs. Energy-minimized docking poses (represented in Figure 34) are marked with a diamond on the τ_1-τ_2 surface.

Analysis of the coupling constants and of the Nuclear Overhauser Effect (NOE) signals showed a restricted conformational sampling of the ethylamide chain (Figure 37). The signal of the β carbon hydrogen has two coupling constants ($J_{H\beta,H\alpha1}$ = 4.9 Hz and $J_{H\beta,H\alpha2}$ = 10.7 Hz), indicating that τ_2 dihedral angle oscillates around values that position H_β in gauche arrangement with $H_{\alpha1}$ and antiperiplanar to $H_{\alpha2}$. A strong NOE signal between H_β and one of the two hydrogens on the carbon α, as well as the lack of NOE signal with the other one support this interpretation. Another NOE cross-peak reveals contact between the two methyl groups N-Me and CH_β-Me, while no contact is visible between the N-Me group and H_β. No contacts could be seen between CH_β-Me and aromatic protons, while H_β had NOE contacts with aromatic protons H2 and H6. Coherently, the presence or absence of NMR cross-peaks support the arrangement assigned to the global free-energy minimum in MD simulations in chloroform, in which H_β lies on the same plane as the aromatic ring and in the opposite direction of the N-Me protons. The CH_β-Me group would be placed roughly perpendicular to the aromatic ring and close to the N-Me group.

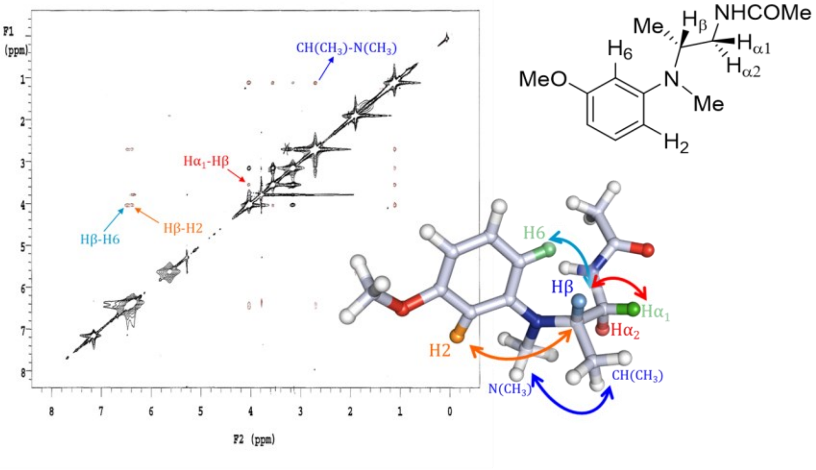

Figure 37. NOESY NMR spectrum performed in chloroform at 600 MHz and (*R*)-UCM1183 conformation consenting the assignment of all the cross-peaks.

Comparing the bound conformations of UCM1183 enantiomers with the conformational space in chloroform, it is possible to see that the τ_1 dihedral angle of -150° is preferred in solution for the (*S*)-derivative, and a *gauche* arrangement of the docked (*R*)-enantiomer is energetically discouraged. Moreover, the *anti*-arrangement of the τ_2 dihedral angle of the docked conformation, while not being the preferred conformation, is still compatible with the formation the hydrogen bond with Q194^{ECL2}. Therefore, chiral recognition at the receptor level could still alter the conformational equilibrium, favouring the bioactive conformation.

5.2.4 Impact of the membrane bilayer on the conformational abundance of (*S*)-UCM1183

Given the probability of melatonergic ligands to partition in the membrane, the impact of the medium on the conformational abundance of UCM1183 was evaluated (Figure 38). MD simulation in a TIP3P water box gave results to those obtained in chloroform, corroborating the minimum free-energy conformation validated by NMR spectra, in which the β-methyl group induces an asymmetry in the probability distribution for the τ_1 values, placing the amide group over or beneath the plane identified by the anilino scaffold.

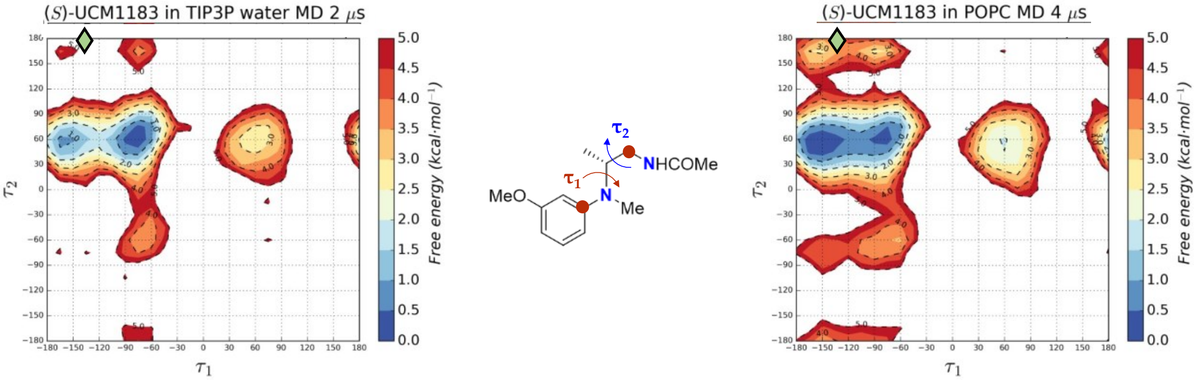

Figure 38. Free-energy surfaces of the unbound (*R*)-UCM1183 are obtained in two different explicit systems (TIP3P water and POPC membrane boxes). Energy-minimized docking pose is marked with a diamond on the τ_1-τ_2 surface.

As previously discussed in Chapter 4, melatonergic compounds would readily partition in the membrane bilayer. The interaction with the micro-environment [216] at the interface between the membrane and receptor could in theory affect the conformational space of τ_2, disfavouring the “folded” conformation preferred in water. While in water, the docking conformation of the bound (*S*)-derivative has a free-energy difference from the minimum energy one much higher than in the chloroform phase, this conformation would be more accessed in a membrane model box. The simulation performed in 1-palmitoyl-2-oleoyl-*sn*-phosphatidylcholine (POPC) evidenced a lower free-energy difference between the two free-energy basins (Figure 38). The variation in the conformational abundance of rotamers population in the alkylamide chain is, therefore, coherent with MD [214] and MetaD [215] simulations by Martì and colleagues.

5.2.5 Conformational selection drives stereoselectivity of O-phenoxyethylamides

Given that the stereoselectivity of N-anilinoethylamides is driven by the conformational equilibria in the solvent, the same behaviour could affect the binding affinities observed for other melatonergic ligands, such as derivatives reported in Table 2. Therefore, MD simulation of the eutomer (S)-**2**, within the series of phenoxyethylamides reported in Carocci et al. (116), was performed in a TIP3P water box. According to the data reported in the literature, the insertion of a methyl substituent at the β position of the (thio)phenoxyethylamide scaffold led to an affinity increase at both receptor subtypes, conserving the stereoselectivity seen in N-anilinoethylamides. The (*S*)-enantiomer is characterized by a higher binding affinity at both series, with (*S*)-**2** reaching a higher stereoselectivity by ~1.5 pK$_i$ units and its thioanalogue (*S*)-**3** by around 2 pK$_i$ units. [116]

Table 2. Biological activity of methyl-substituted phenoxy- and thiophenoxy- ethylamides.

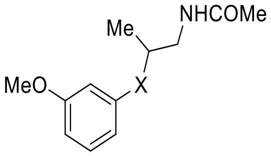

Compound	**X**	**MT$_1$**		**MT$_2$**	
		p*K*$_i$ (±SD) [a]	**IA (±SD)** [b]	**p*K*$_i$ (±SD)** [b]	**IA (±SD)** [b]
Melatonin	--	9.48 ± 0.06	1.00 ± 0.18	9.21 ± 0.09	1.00 ± 0.07
2	O	8.44 ± 0.41	1.01 ± 0.03	8.02 ± 0.71	1.01 ± 0.07
(*R*)-2	O	7.31 ± 0.37	0.79 ± 0.05	6.96 ± 0.38	0.93 ± 0.20
(*S*)-2	O	8.77 ± 0.43	1.01 ± 0.06	8.33 ± 0.49	1.09 ± 0.07
3	S	6.96 ± 0.05	n.d. [c]	6.58 ± 0.22	n.d. [c]
(*R*)-3	S	5.56 ± 0.23	n.d. [c]	6.18 ± 0.09	n.d. [c]
(*S*)-3	S	8.24 ± 0.08	n.d. [c]	8.15 ± 0.13	n.d. [c]

All data is reported in ref. 116. [a] p*K*$_i$ values were calculated from IC$_{50}$ values, obtained from competition curves by the method of Cheng and Prusoff [243], and are the mean of at least three determinations performed in duplicate. [b] Relative intrinsic activity values were obtained by dividing the maximum analogue-induced G-protein activation by that of melatonin. [c] *n.d.*: not determined

Docking of the two chiral methyl-substituted phenoxyethylamides at the MT$_2$ receptor (Figure 39) resulted in poses characterized by similar GScore values (-7.57 for the (*R*)-derivative and -7.75 kcal·mol^{-1} for the (*S*)-derivative). The compounds retained the hydrogen bond interactions common to the other melatonergic ligands.

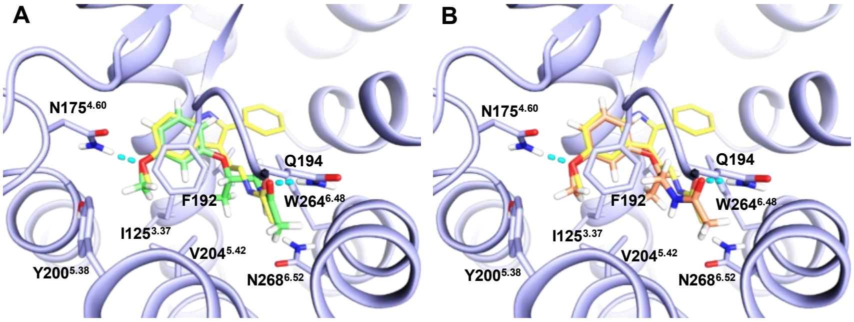

Figure 39. Docking poses within the MT_2 receptor binding site (purple cartoon and sticks) of (*S*)-**2** (**A**, green sticks) and (*R*)-**2** (**B**. orange sticks). 2-Phenylmelatonin, co-crystalized in *6ME6*, is shown with yellow sticks. Hydrogen bonds are represented with cyan dashed lines. A portion of the TM V and of the ECL2 has been omitted for clarity.

The methyl substituents are approximately superposed and occupy the same hydrophobic portion of the receptor bound by CH$_\beta$-Me group of chiral N-anilinoethylamides (Figure 34.C-D). While the phenoxy oxygen and the β carbons of both compounds are roughly within the plane of the aromatic ring, (*S*)-**2** is characterized by τ_1=-150.2° and τ_2 =174°, and (*R*)-**2** by τ_1=-59.4° and τ_2 =-169.4°.

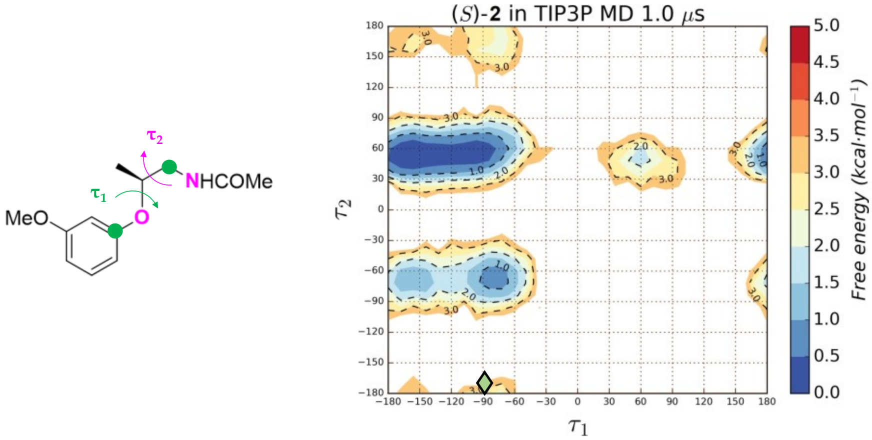

Figure 40. Left. Representation of dihedral angles used to project FES of (*S*)-**2** in solution**.** FES of the compounds . The green diamond marks the τ_1 and τ_2 values assumed by the docking pose of (*S*)-**2** at the MT_2 receptor (Figure 39.A).

MD simulation of compound (*S*)-**2** was performed for 1 μs in a box of explicit water molecules to assess the conformational abundance of the bioactive conformation. The free-energy basin with the highest probability corresponds to the conformation having τ_1~-150° and τ_2~60°, while the most populated conformation of (*R*)-**2** is characterized by specular values of the two dihedral angles (Figure 40). While the τ_1 value of eutomer in the docking pose is the one preferred in solution, the value of the (*R*)-**2** in the MT_2 receptor binding site is not accessed in MD simulations. τ_2 values observed in the docking complexes refer to *anti* arrangement lowly sampled in MD simulations in water. However, the interaction of alkylamide group with the receptor or the membrane-solvent interface could in theory modify the conformational equilibria favouring the bioactive conformation, as seen before.

5.3 RESULTS AND DISCUSSION: CONFORMATIONAL SELECTION OF TETRAHYDROQUINOLINES DERIVATIVES

Given the stereoselectivity observed for chiral β-methyl-substituted N-anilinoethylamides, it could be speculated that the same rationalization could be applied to tetrahydroquinolines being partially constrained derivatives of the former class. The most potent and MT_2-selective compound of the class, UCM1014, has been tested as a racemic mixture. Moreover, the unclear assignment of chirality of compound **15** (Figure 31) did not permit to clarify the enantioselectivity of these derivatives. However, MD simulations previously performed in water revealed (*R*)-**15** as the eutomer being its most abundant conformation in water. In turn, in such arrangement, the compound is superimposable to melatonin bioactive conformation. [123] To corroborate this finding, UCM1014 enantiomers were stereoselectively prepared and separately tested to assess which enantiomer achieved higher binding affinity. MD and *wt*-MetaD simulations have been performed to characterize the binding mode of the two enantiomers at the MT_2 receptor and these efforts rationalized their different activity.

5.3.1 Biological activity of UCM1014 enantiomers

For the first time, UCM1014 enantiomers were stereoselectively prepared via optical resolution with Evans chiral auxiliary reagent. [244] Pharmacology experiments were performed at the University of Ferrara. Binding affinity and functional activity assays were performed in CHO cells stably expressing the human MT_1 and MT_2 receptors and confirmed the subtype selectivity and full agonist activity (Table 3) of the racemic mixture.

Table 3. Biological activity of UCM1014 enantiomers.

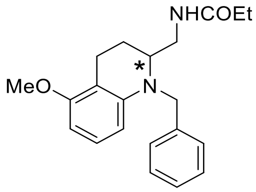

Compound	**MT₁**		**MT₂**	
	K_i (±SD) [a]	**EC_{50} (±SD)** [b]	**K_i (±SD)** [a]	**EC_{50} (±SD)** [b]
Melatonin	0.240 ± 0.016	0.277 ± 0.024	0.326 ± 0.022	0.975 ± 0.087
UCM1014	18.3 ± 1.6	31 ± 2	0.058 ± 0.004	0.436 ± 0.035
(*R*)-UCM1014	7.23 ± 0.61	12.4 ± 1.1	0.045 ± 0.004	0.245 ± 0.019
(*S*)-UCM1014	91 ± 8	290 ± 23	2.10 ± 0.17	9.32 ± 0.77

[a] K_i values were calculated from IC_{50} values, obtained from competition curves by the method of Cheng and Prusoff [243], and are the mean of at least three determinations performed in duplicate.
[b] EC_{50} values are obtained from forskolin-induced cAMP assays.

5.3.2 UCM1014 enantiomers display a different stability of their binding mode

MD simulations of UCM1014 enantiomers within MT_2 receptor binding site were run starting from the results of docking calculations (Figure 41.A-B). Docking results evaluated with GScore scoring function could not substantially discriminate the two enantiomers (-10.7 kcal·mol^{-1} for (*R*)-UCM1014 vs -10.8 kcal·mol^{-1} for (*S*)-UCM1014), while an increased difference was retrieved via MM-GBSA calculations (-80 kcal·mol^{-1} for (*R*)-UCM1014 vs -75.7 kcal·mol^{-1} for (*S*)-UCM1014), encompassing residue side chains facing the ligands, in part suggesting a better interaction of (*R*)-derivative within the binding site.

The docked pose of both enantiomers could establish a hydrogen bond between the alkylamide side chain and Q194^{ECL2}, assuming different values for the τ_1 dihedral angle (see Figure 42 for τ_1 definition), which resulted in different conformations of the tetrahydroquinoline nucleus and of the acylaminomethyl side chain. After energy minimization of the docking complexes, (*R*)-UCM1014 alkylamide chain was disposed with an axial arrangement (τ_1~-67.8°), while (*S*)-UCM1014 alkylamide had an equatorial one (τ_1~-60.5°).

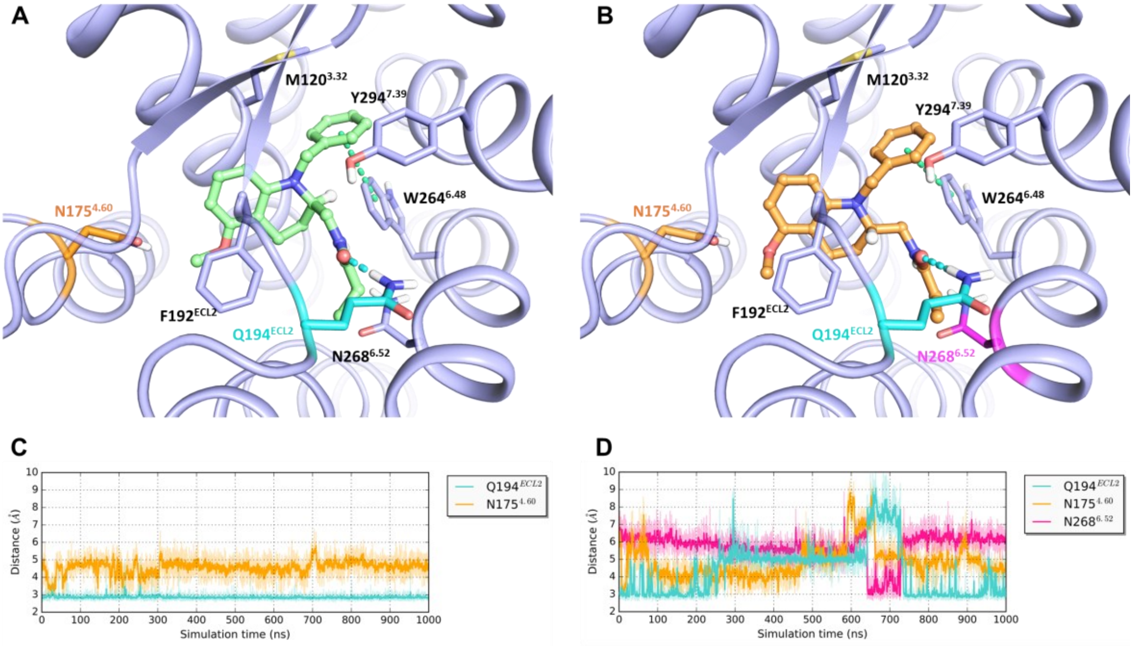

Figure 41. Docking poses within the MT$_2$ receptor binding site (purple cartoon and sticks) of (*R*)-UCM1014 (**A**, green sticks) and (*S*)-UCM1014 (**B**, orange sticks). Hydrogen bonds and π-π interactions are represented with cyan and green dashed lines, respectively. The proton on the chiral center is shown for clarity. Distances between groups engaged in polar interactions between residues of the binding site and the alkylamide and methoxy groups of (*R*)-UCM1014 (**C**) and (*S*)-UCM1014 (**D**), reported with the same colour in which the residue is illustrated in the docking complexes.

The stability of the binding poses of the two enantiomers was evaluated with μs-long MD simulations, during which the axial and equatorial arrangement of the side chain, differently assumed by the two enantiomers, was maintained. (*R*)-UCM1014 kept a stable hydrogen bond with Q194^{ECL2} (Figure 41.C). Conversely, the (*S*)-enantiomer underwent different conformational changes in the binding site, without maintaining the hydrogen bond interaction with Q194^{ECL2} during the entire trajectory. Moreover, both ligands could not stably interact via their methoxy group with N175$^{4.60}$. The (*S*)-derivative differently accommodated in the binding site during the trajectory (Figure 41.D), eventually interacting either still with Q194^{ECL2} via water-mediated interactions (~250-640 ns in Figure 41.D) or with N268$^{6.52}$ (~640-750 ns), another polar residue in the binding site near the alkylamide tail. These alternative binding modes explored by (*S*)-UCM1014 in the trajectory are coherent with the functional redundancy reported at the MT$_2$ receptor of the two polar residues in mutagenesis experiments. [75] Therefore, according to MD simulations, the docking pose of the eutomer is more stable, while the distomer would be destabilized in alternative configurations, which might partially be unproductive for the receptor engagement and activation and would be responsible for the around fifty-fold loss of affinity.

Since, the axial-equatorial conformational change of the acylaminomethyl side chain could not be explored within the receptor binding site with unbiased sampling of plain MD simulations, *wt*-MetaD simulations were performed to assess the conformational abundance associated to τ_1 rotamer populations (as defined in Figure 42). The resulting FES reveals that the axial arrangement (τ_1~-60°) is preferred by nearly 6 $kcal \cdot mol^{-1}$ (Figure 42.A) with respect to the equatorial one (τ_1~40°) within the MT_2 receptor for (*R*)-UCM1014. Shifting from the axial to the equatorial arrangement of the alkylamide chain, the ligand could maintain the hydrogen bond with $Q194^{ECL2}$ during all the simulation with both arrangements (see free-energy reweighting analysis in Figure 42).

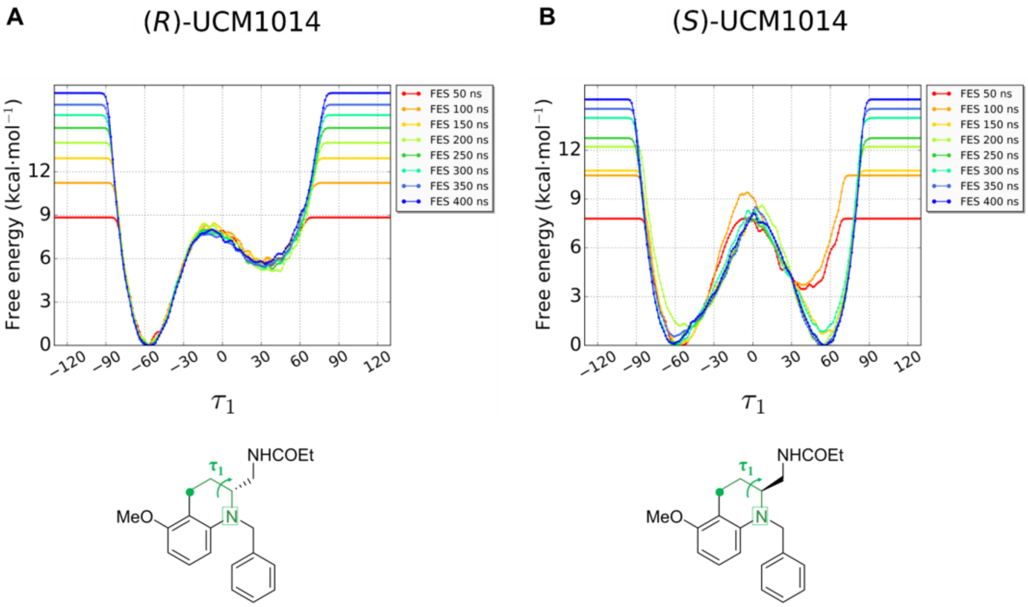

Figure 42. FES via *wt*-MetaD simulations show a different conformational abundance of τ_1 dihedral angle for UCM1014 enantiomers, bound within the MT_2 receptor orthosteric site. Time-evolution of the free-energy surface is shown along 400 ns for (*R*)-UCM1014 (**A**) and (*S*)-UCM1014 (**B**).

Previous simulations performed for compound **15** in a water box, revealed that the conformational equilibria in the solvent favour the axial arrangement by ~1.5 kcal·mol^{-1}. [123] Therefore, similarly to β-methyl substituted analogues discussed before, the conformational equilibria in the unbound phase would concur to the higher affinity of the eutomer.

The unstable binding mode shown by (*S*)-UCM1014 is still found in MetaD simulation, since in this case the axial conformation of the ligand is accessed on a free-energy level (Figure 42.B) comparable to the one of the docking pose, but without undertaking the hydrogen bond with Q194. Instead, such an arrangement allows interaction with the other polar residue facing the binding site (N268$^{6.52}$), and spontaneously contacted in MD simulations. Analysis through free-energy reweighting of the distances (Figure 43), which are associated to the two possible polar contacts of the alkylamide chain, evidenced such instability of the binding mode of the distomer.

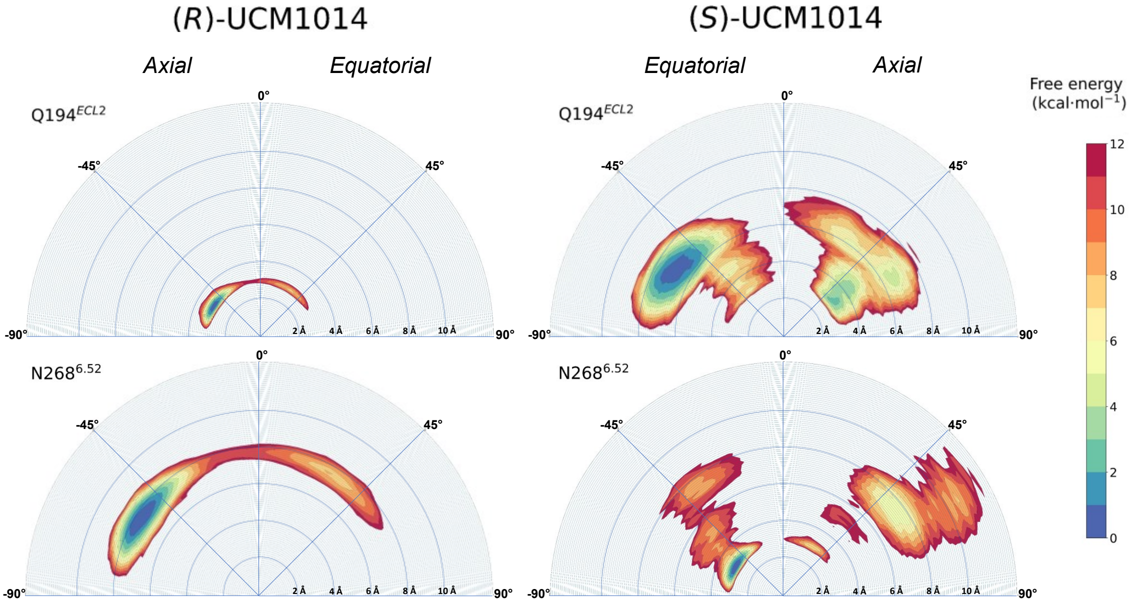

Figure 43. FES obtained via free-energy reweighting analysis shows the different stability of UCM1014 enantiomers within the MT$_2$ receptor binding site and the probability of interaction with residues Q194^{ECL2} and N268$^{6.52}$, with respect to τ_1 axial and equatorial conformations. Polar plot radius is defined based on the distance between the heteroatoms.

5.4 CONCLUSIONS AND PERSPECTIVES

The case offered by enantiomers of UCM1183 shows the important interplay between the conformational abundance in the solvent and the preferred conformation in the binding pocket. The slight gain of affinity caused by the insertion of the methyl group on the β-carbon of the alkylamide chain is rationalized by the conformational enrichment of the bioactive conformation of the eutomer. For both enantiomers, τ_2 dihedral is preferred in *gauche* arrangement, while the recognition within the receptor binding site (and the interaction with the membrane-solvent interface) could promote the *anti* conformation. Instead, in the case of τ_1 dihedral, the introduction of the methyl substituent promoted the conformational enrichment of the value observed in the docking pose, just for the eutomer. While the application for the introduction of substituents in this portion of the binding site is limited, [238,245] possibly for the involvement in the receptor activation mechanism, [87] small hydrophilic groups could still be accommodated within this region, as crystal structure could show electron density potentially attributed to propanol used as crystallization buffer. [93] Very recently, Tsotinis et al. [245] reported tetracyclic derivatives in which compound **17** (Figure 33) endowed with at β-methyl substituent conserved binding affinity and agonist activity, while the β,β-dimethyl-derivative **18** lost functional efficacy in GTPγS assay.

The relationship between the chiral substitution at the β position of the alkylamide and the abundance in the solvent is conserved among different classes of bioisosteric melatonergic ligands. This finding supports the bioisosterism between the indole and simplified scaffolds. Moreover, it partially rationalizes the high affinity obtained by tetrahydroquinoline derivatives, such as UCM1014, in which the *N*-anilinoethylamide scaffold has been rigidified with a partial constraint.

From a more general viewpoint, MD simulations have proven able to sample the conformational space of small molecules in a reasonable time. Therefore, the prediction of the most populated conformation in solution (and in the bound state) is a valid contribution to the drug design process. However, for an adequate sampling of the ligand bound conformation, biased simulations, such as MetaD, could be still required, as in the case of UCM1014 enantiomers within the MT_2 receptor binding site. Exploiting conformational analysis, medicinal chemists can prioritize the synthesis of novel compounds with affinity increases induced by the alteration of conformational equilibria.

5.5 COMPUTATIONAL PROTOCOLS

5.5.1 Ligand docking and MM-GBSA rescoring calculations

UCM793 and enantiomers of UCM1183, compound **2** and UCM1014 structures were built in Maestro 11.6 [246] and minimized with the OPLS3e force field [193] in the GB/SA implicit model [247] implemented in MacroModel 12.0 [192] to an energy gradient of 0.01 kJ·mol^{-1}·Å^{-1}. The prepared complex between the MT$_2$ receptor and 2-phenylmelatonin was used to run docking simulations (see Appendix I). The docking grid was obtained by imposing a cubic bounding box of 10 Å and an enclosing box of 20 Å, centred on the ligand. Docking calculations were executed through Glide 7.9 [190] in standard precision mode. MAXKEEP and MAXREF parameters, which control the number of poses to retain after the rough scoring stage and the number of poses to refine, were increased a tenfold. In the case of UCM1014 enantiomers, the scoring window cutoff was increased to 100 kJ·mol^{-1}. The pose with best GScore for each compound was selected. The obtained complexes were rescored through MM-GBSA calculations with Prime 5.2 [248], after energy minimization in the GB/SA continuum model [247] to a gradient of 0.1 kJ·mol^{-1}·Å^{-1}, including the ligand and the surrounding side chains in a sphere of 12 Å, similarly to ref. 249.

All docking poses were energy-minimized with MacroModel [192] to an energy gradient of 0.01 kJ·mol^{-1}·Å^{-1} using the Polak-Ribière conjugate gradient method [250] and including in the minimization the ligand and the receptor side chains within 5 Å.

5.5.2 Molecular dynamics simulations

MD simulations, including MT$_2$ receptor complexes with N-anilinoethylamides and phenoxyethylamides, were conducted with Desmond 5.4 [251] with OPLS3e force field. [193] Bond lengths to hydrogen atoms were constrained by applying the M-SHAKE algorithm [252]. Short-range electrostatic interactions were cut-off at 9 Å, whereas long-range electrostatic interactions were treated using the smooth Particle Mesh Ewald method

[253]. A RESPA integrator [254] was used with a double time-step regime, in which bonded and short-range non-bonded interactions were computed every 2 fs. Instead, long-range electrostatic interactions were computed every 6 fs. The same protocol was applied for the compounds in different phases, including TIP3P water, chloroform and POPC membrane.

Instead, MD simulations were performed for the complexes between the MT_2 receptor and UCM1014 enantiomers using Gromacs 2019.4. [202] The two systems were prepared and parametrized for the two enantiomers and MD simulations run with the same protocols reported in Paragraph 4.2.1. Prior to system preparation, the bound binding pocket of the two complexes were solvated via Gran Canonical Monte Carlo (GCMC) simulations performed with Desmond 5.4. [251] In these simulations, the binding pockets and all the buried cavities around 10 Å from the ligand are coupled to a bulk environment with fixed chemical potential. [155] After equilibration, protein α carbons were restrained for 100 ns with a force constant of $0.1\ \mathrm{kcal{\cdot}mol^{-1}{\cdot}Å^{-2}}$.

MD simulations of ligands in chloroform

UCM1183 enantiomers were solvated in a chloroform box surrounding the ligand for at least 12 Å in every direction. In turn, the box of chloroform, measuring 512 $Å^3$ and consisting of 2560 solvent molecules, was modelled with Maestro 11.6 [246] with OPLS3e force field [193] and equilibrated in NPT ensemble at 300 K for 1.5 ns. After a short equilibration, the production stage amounted to 2 μs in NVT ensemble at 300 K, a temperature enforced through Langevin thermostat. [255] Geometric parameters of interest were collected during the trajectories and their probabilities projected onto binned 2D plots. The relative free energy content for each bin i was calculated as follows:

$$A_i = -RT \ln \frac{N_i}{N_0} \tag{5.1}$$

where N_i is the number of snapshots collected in a single bin i and N_0 is the number of snapshots in the most populated bin, which, therefore, corresponds to the FES global free-energy minimum. The protocol was then applied to (*S*)-**2**.

MD simulations of receptor-UCM1183 enantiomers complexes

The energy minimized complexes were embedded in a pre-equilibrated POPC bilayer [256] in order to surround the receptor for at least 13 Å. Electroneutrality of the systems was obtained by adding 10 Cl^- ions. MD simulations were carried out for 150 ns in NPT ensemble at 300 K and 1.0 atm by applying a Langevin coupling scheme [255] with a relaxation time of 1 ps and a damping coefficient of 2 ps^{-1}. Protein α carbons were restrained with 0.1 $kcal \cdot mol^{-1} \cdot Å^{-2}$.

5.5.3 Well-tempered metadynamics simulations

After 1.0 µs-long unrestrained MD simulation, the complexes between MT_2 receptor and UCM1014 enantiomers are submitted to a *wt*-MetaD [174] lasting for 400 ns to sample the conformation of the tetrahydroquinoline nucleus and of the flexible alkylamide chain, using as *CV* the dihedral angle τ_1, as defined in Figure 42. Gromacs 2019.4 [202] was used in conjunction with Plumed 2.5.4 plugin. [203] The history-dependent bias potential is added in the form of Gaussian hills with the width fixed to 0.035 rad (~2°) and height was set to 0.15 $kcal \cdot mol^{-1}$. Gaussians were infrequently deposited every 50 ps. Hills height was rescaled over time by adopting a bias factor γ=10. Free-energy reweighting analysis is performed according to ref. 178.

Chapter 6. Molecular modelling requirements for the binding affinity and the subtype selectivity at the MT_2 receptor

6.1 INTRODUCTION

6.1.1 Occupation of an out-of-plane region at the MT$_2$ receptor drives ligand subtype selectivity

As reported in Chapter 2, the introduction of substituents in position 1 or 2 of the indole ring of melatonin and not coplanar with the indole, likely occupying an out-of-plane portion of the receptor binding pocket, is a molecular determinant providing MT$_2$ selectivity. The hypothesis was originally drawn through QSAR analysis [101,102] and was confirmed for bioisosteric scaffolds, including the tetrahydroquinoline ring (for substituents at position 2, i.e., UCM1014, Figure 11) [123] or the *N*-anilinoethylamide one (for substituents at the aniline nitrogen, i.e., UCM765 or UCM800, Figure 11). [117] Moreover, bulky substituents occupying this region of the receptor, possibly arranged on the opposite side of the indole ring with respect to the alkylamide chain, would eventually decrease the intrinsic activity. [102,142] The impact on intrinsic activity of substituents in this region mirrors the general paradigm shared by other class A GPCRs, linking receptor inactivation to contact of the ligand with the so-called “*aromatic cluster*”, which comprises the super-conserved W6.48 “*toogle switch*” of the CWxP motif. [257] In melatonin receptors, this region of the binding site consists of a hydrophobic subpocket, comprising mostly hydrophobic residues conserved at both receptor subtypes (i.e., Y81/94$^{2.58}$, M103/120$^{3.32}$, V107/124$^{3.36}$, W251/264$^{6.48}$, Y281/294$^{7.39}$, A284/297$^{7.42}$ and Y285/298$^{7.43}$).

X-ray crystal [74,75] and cryo-electron microscopy [96,87] structures of the receptors, while evidencing a wider subpocket at the MT$_2$ receptor, did not provide hints for an out-of-plane region. Indeed, in-plane substituents of co-crystalized ligands accommodated in this region, such as the 2-phenyl or the 2-iodine substituents increase binding affinity [112] but not the selectivity at the MT$_2$ receptor, as happens with other substituents (e.g., 2-benzyl, 2-phenethyl or 2-naphthyl) [101,111] projecting outside of the indole ring. No hint about the accommodation of the out-of-plane substituent is actually available. As a matter of fact, no conformational constraint is present in subtype-selective ligands. Moreover, receptor crystal structures do not show any difference in the availability of the binding pocket to ligands substituted at the aromatic subpocket. Therefore, the investigation of a series of 2-aryl substituted indoles endowed with different size and shape was pursued to gain information on the occupation of the aromatic subpocket. Simulations were performed to investigate the different tolerance to out-of-plane substituents at the two melatonin receptors. In particular, TI simulations provided a rationale for the reduced affinity at the MT_1 receptor of compounds carrying out-of-plane substituents.

6.1.2 Polar substituents at the aromatic subpocket maintain high MT_2 receptor binding affinity

Insertion of hydrophilic susbtituents in position 2 of the indole ring of melatonin, or in corresponding positions on other scaffolds, can be considered in order to reduce lipophilicity and to increase the water-solubility of melatonergic ligands. Molecular modelling studies could offer a rationale for the insertion of such substituents, that might also improve pharmacokinetic properties (e.g., oral bioavailability and metabolic liability), while preserving the high binding affinity offered by substituents occupying the aromatic subpocket. Different polar substituents have already been considered that are possibly accommodated in this region of the binding site (Figure 44), such as the 2-substituted benzofurans derivative **20**, [119] the dihydro-2*H*-indeno[5,4-*b*]furan derivative **21**, [136] the furochromene derivative **22**, [258] the 3-phenyl-naphthalene derivative **23**, [259] and other compounds synthetized by the group of Prof. Zlotos, harbouring groups with different levels of basicity. [260,261,262]

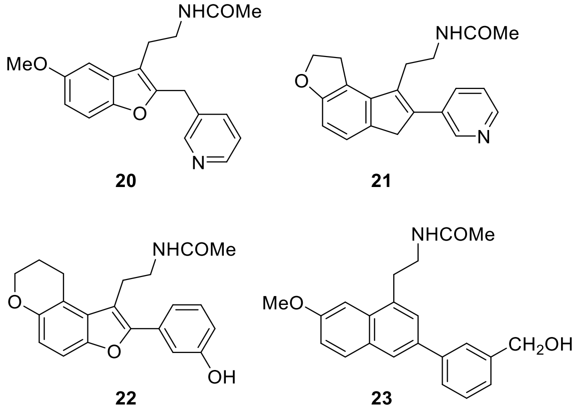

Figure 44. Compounds bearing hydrophilic substituents in positions corresponding to position 2 of the indole ring of melatonin.

Hydrophilic substituents that might be accommodated in this region do not necessarily abrogate the high binding affinity obtained by their lipophilic analogues. For example, compound **23** maintained nearly the same affinity at the MT_2 receptor as the derivative without the hydroxymethyl substituent. Moreover, compound **23** showed around seven-hundred times selectivity for the MT_2 receptor, likely due to the scaffold which is already selective at this receptor subtype. [259]

Being a valuable pharmacological tool for the characterization of the MT_2 receptor, UCM765 (Figure 11) achieves a partial agonist activity and selectivity for the MT_2 receptor. [117] However, metabolically liable sites at the *N*-anilinoethylamide scaffold and at the phenyl ring substituting the methoxy-aniline nitrogen are present, potentially limiting its pharmacological applications. Substitutions of these sites, i.e., by replacing the methoxy group with a bioisosteric bromine and protection of the para position of the *N*-phenyl substituent with a fluorine, resulted in UCM924 (Figure 11) characterized by a higher microsomal stability to cytochrome enzymes. [145] Unfortunately, both UCM765 and UCM924 have low water-solubility, prompting the necessity to design analogues endowed with more favourable physicochemical properties. Structure-activity relationships of series of 2-substituted indoles and N-anilinoethylamides are reported in this Chapter to address the issue, in order to introduce polar groups without losing the high binding affinity and selectivity at the MT_2 receptor. To this aim, MD simulations were used to rationalize the tolerance to hydrophilic groups occupying the aromatic subpocket, monitoring water distribution and the interaction with polar residues.

6.2 RESULTS AND DISCUSSION: 2-ARYL INDOLE DERIVATIVES

6.2.1 Biological activity and structure-activity relationships of 2-aryl-indole derivatives

2-Substituted indole derivatives (Table 4) were prepared through sequential C_2–H borylation and Pd-catalyzed coupling [263] at the University of Urbino with substituents characterized by different size, shape and physicochemical properties of the substituent replacing the phenyl group in position 2 of the indole ring.

Table 4. Binding affinity and intrinsic activity of 2-aryl substituted melatonin analogues

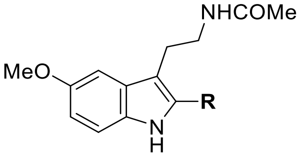

Compound	R	MT$_1$		MT$_2$	
		p*K*$_i$ (±SD) [a]	**IA (±SD)** [b]	**p*K*$_i$ (±SD)** [b]	**IA (±SD)** [b]
Melatonin	-H	9.74 ± 0.05	1.00 ± 0.02	9.80 ± 0.06	1.00 ± 0.01
2-PhMLT [c]	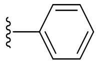	10.66	0.96	10.42	0.98
2-BnMLT [d]	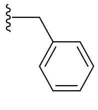	7.5	n.d	9.6	n.d.
24	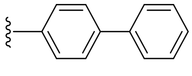	7.79 ± 0.08	1.07 ± 0.04	8.30 ± 0.15	0.84 ± 0.05
25	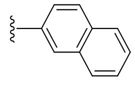	7.44 ± 0.08	0.59 ± 0.02	8.96 ± 0.28	0.48 ± 0.07
UCM1327, 26	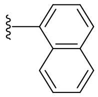	7.81 ± 0.08	0.67 ± 0.03	9.72 ± 0.05	0.44 ± 0.08
27	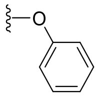	7.94 ± 0.15	0.54 ± 0.07	8.53 ± 0.07	0.50 ± 0.04
28	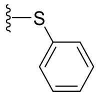	9.01 ± 0.05	0.26 ± 0.05	10.20 ± 0.13	0.29 ± 0.10
29	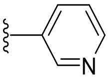	9.77 ± 0.08	0.97 ± 0.06	10.22 ± 0.09	0.55 ± 0.08
30	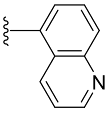	7.83 ± 0.13	0.46 ± 0.10	8.57 ± 0.03	0.38 ± 0.07
31	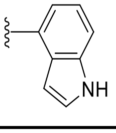	7.83 ± 0.06	0.96 ± 0.04	9.53 ± 0.07	0.39 ± 0.19

[a] pK_i values calculated from IC$_{50}$ values, obtained from competition curves by the method of Cheng and Prusoff [243] as the mean of at least three determinations performed in duplicate. [b] Relative intrinsic activity values were obtained by dividing the maximum analogue-induced G-protein activation by that of MLT, performed in triplicate. [c] Binding affinities obtained from NIH3T3 cell lysates and data from ref. 101. [d] Binding affinities obtained from COS-7 cell lysates. 2-BnMLT is described as a partial agonist in the [^{3}H]dopamine release assay from rabbit retina. [111]

The aim is to probe the steric properties of the subpocket occupied by the phenyl ring of 2-phenylmelatonin (2-PhMLT), in order to achieve a higher selectivity at the MT_2 receptor, and to insert hydrophilic groups that should permit an increase in water-solubility without loss of binding affinity.

Introduction of the aromatic substituents variously impacted on binding affinity, depending on their spatial arrangement with respect to the plane of the indole ring (Table 4). Compared to 2-PhMLT and MLT, the biphenyl derivative (compound **24**) scored a lower binding affinity at both subtypes, potentially reaching the boundary in the longitudinal extension of the aromatic subpocket. Albeit with reduced binding affinity, **24** conserved an agonist activity as 2-PhMLT. Instead, the β- and α-naphthyl derivatives **25** and **26** attained selectivity at the MT_2 receptor, while reducing the intrinsic activity in the $[^{35}S]GTP\gamma S$ assays, consistently with an out-of-plane arrangement of their substituent. [102] In fact, with respect to the biphenyl derivative **24**, compounds **25** and **26** had the same reduced affinity at the MT_1 receptor and higher affinity at the MT_2 receptor, leading to compound **26** obtaining nearly one-hundred-fold selectivity at the MT_2 receptor. Interestingly, in a series of C2-substitued furo[3,2-*b*]pyridines, the α-naphthyl derivative achieved a similar selectivity toward the MT_2 receptor. However, the β-naphthyl analogue of this series had a tenfold higher affinity at the receptor. [264] Compounds **27** and **28**, bearing a 2-phenyloxy and a 2-phenylthio group, respectively, being 2-BnMLT bioisosteres, obtained a partial agonist behaviour and MT_2 subtype-selectivity. In particular, the more lipophilic compound **28** achieved a notable affinity at both receptor subtypes and a pK_i value of 10.20 at the MT_2 receptor, nearly on par with the one of 2-PhMLT.

Taken together, intrinsic activity results support the previous studies, linking the presence of out-of-plane substituents in position 2 of the indole ring with a reduced intrinsic activity. A previous pharmacophore model based on stereoselective ligands postulated that the arrangement of such substituents would be on the opposite side of the indole ring plane with respect to the alkylamide chain. [142] To prove this hypothesis, *N*-methyl derivatives of compound **26** were stereoselectively prepared to obtain two atropisomers in which the rotation of the α-naphthyl group is hampered by the introduction of the methyl substituent on the indole ring nitrogen.

Atropisomers (R_a)-**32** and (S_a)-**32**, which were prepared through (-)-menthyl-derivatives diastereoisomers, achieved a comparable affinity at both receptors in assays performed on receptor expressed in two different cell lines (Table 5), suggesting no preference for the arrangement of the naphthyl group, located on either side of the indole ring.

Table 5. Binding affinity and intrinsic activity of 2-α-naphthyl-indoles atropisomers

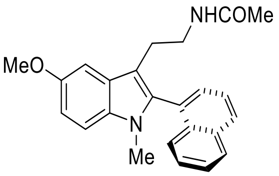

(R_a)-**32**

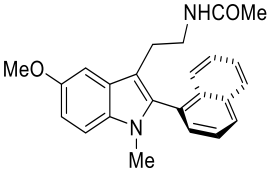

(S_a)-**32**

Compound		**MT$_1$**			**MT$_2$**	
	p*K*$_i$ (±SD) NIH3T3 [a]	**IA (±SD) NIH3T3 [b]**	**p*K*$_i$ (±SD) CHO [c]**	**p*K*$_i$ (±SD) NIH3T3 [b]**	**IA (±SD) NIH3T3 [b]**	**p*K*$_i$ (±SD) CHO [c]**
Melatonin	9.74 ± 0.05	1.00 ± 0.02	9.62 ± 0.05	9.80 ± 0.06	1.00 ± 0.01	9.49 ± 0.05
(R_a/S_a)-32	7.92 ± 0.04	0.24 ± 0.05	7.39 ± 0.06	9.51 ± 0.11	0.22 ± 0.03	9.52 ± 0.04
(R_a)-32	7.47 ± 0.10	0.25 ± 0.07	7.01 ± 0.05	9.24 ± 0.07	0.36 ± 0.09	9.42 ± 0.05
(S_a)-32	7.89 ± 0.03	0.18 ± 0.04	7.48 ± 0.05	9.90 ± 0.04	0.29 ± 0.04	9.54 ± 0.06

[a,c] pK_i values were calculated from IC_{50} values, obtained from competition curves by the method of Cheng and Prusoff [243], and are the mean of at least three determinations performed in duplicate. [b] Relative intrinsic activity values were obtained by dividing the maximum analogue-induced G-protein activation by that of MLT, performed in triplicate.

Moreover, a few compounds with more polar substituents were prepared to test the tolerance of the subpocket to more polar substituents. Different aza-heterocycles were inserted looking for additional polar interactions. The substitution with a 3-pyridyl group (**29**) led to high binding affinity at both receptor subtypes and in a very limited selectivity for the MT$_2$ receptor in analogy with derivatives sharing a 1,6-dihydro-2*H*-indeno[5,4-b]furan tricyclic scaffold substituted with a phenyl or 3-pyridyl substituent. [136] Instead, selectivity for the MT$_2$ receptor was enhanced by aza-bicyclic derivatives, analogously to what observed for compound **26** with respect to 2-PhMLT. While the 5-quinolinyl derivative **30** lost binding affinity for about one order of magnitude at the MT$_2$ receptor, the 4-indolyl analogue **31** nearly maintained the high affinity achieved by compound **26**.

6.2.2 Alchemical calculations rationalize requirements for the MT_2 selectivity

The new 2-substituted indole (Table 4) compounds gained a certain degree of selectivity for the MT_2 receptor, mostly due to a reduction of binding affinity at the MT_1 receptor with respect to melatonin and its derivative 2-PhMLT with increased affinity. Apparently, the out-of-plane region of the receptor previously postulated in MT_2 homology models [265] is not well defined in the X-ray crystal structures, probably due to the presence of nonselective agonists in the binding sites. Therefore, to find a determinant for the selectivity of compounds belonging to this series, thermodynamic integration simulations were performed to convert the nonselective co-crystalized 2-PhMLT into compound **26**, which is the most selective of the series, reaching around 80-fold selectivity for the MT_2 receptor. To investigate the steric tolerance of the aromatic subpocket, the 2-phenyl ring of the co-crystalized ligand was alchemically replaced with the α-naphthyl substituent of compound **26** within the MT_1 and MT_2 receptor binding sites and the free-energy difference between the two complexes was calculated by averaging four independent simulations carried out at both receptors (Figure 45.A), without the need to perform any simulation in the solvent.

In thermodynamic integration simulations, Coulomb and Van der Waals potentials of unique atoms (two hydrogens of 2-PhMLT, four aromatic carbon atoms and four hydrogens of compound **26**) are replaced with λ-dependent softcore potentials described in eqs. 3.32 and 3.33. [181] For each replica (see Appendix II), the integration of $\langle \partial V/\partial\lambda \rangle$ over the coupling parameter led to different averaged ΔG profiles at the two receptors (Figure 45.B). At windows with a lower λ, the average ΔG profile showed a favourable transformation at both receptors. However, progressing on higher λ values, the growth of the α-naphthyl substituent was tolerated at the MT_2 receptor subtype only, leading to an overall null free-energy variation for the alchemical transformation. Conversely, the transformation of the substituent at the MT_1 receptor required an additional ΔG cost. The resulting relative binding free energy ± S.E.M. consists in

$$\begin{aligned}\Delta\Delta G_{calc}\left(\Delta G_{MT_2} - \Delta G_{MT_1}\right) &= (-0.05 \pm 0.24) - (2.42 \pm 0.52) = \\ &= 2.47 \pm 0.57\ \mathrm{kcal{\cdot}mol^{-1}}\end{aligned} \qquad (6.1)$$

which is in line with the experimental $\Delta\Delta G_{exp}$= -2.71 kcal·mol^{-1} given by the ratio of affinity constants of compound **26** at the two receptors. Therefore, simulations highlight the reduced tolerance of the aromatic subpocket of the MT_1 receptor for out-of-plane substituents, such as the α-naphthyl group of compound **26**.

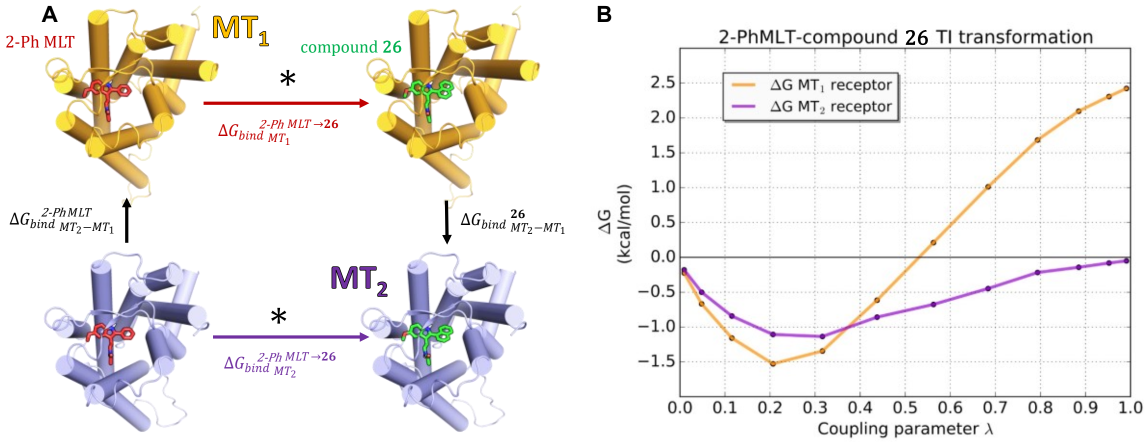

Figure 45. Representation of the thermodynamic cycle employed in TI simulations converting 2-PhMLT into compound **26** to obtain a relative binding free energy associated with receptor subtype selectivity. Alchemical transformations are marked with asterisks. (**A**) The free-energy change due to the transformation is shown as a function of the coupling parameter λ. (**B**)

Inspection of endpoint simulations in which the softcore potentials mostly resemble the Van der Waals and Coulomb functions for either the phenyl (λ=0.0092) or the naphthyl ring atoms (λ=0.9978), revealed interesting consideration regarding the distances between select aromatic residues belonging to the lipophilic subpocket. At λ=0.0092, i.e., the simulations in which softcore potentials mostly recall Van der Waals and Coulomb potentials of 2-PhMLT, the two distances defined in Figure 46.A, between residue in position 6.48 and those in positions 7.43 and 2.58 (according to Ballesteros numbering) [76], assume a lower value at the MT_1 receptor than at the MT_2 receptor. Conversely, at λ =0.9978, simulation in which unique atoms mostly resemble the ones of compound **26**, these two distances are more similar at the two receptor subtypes (Figure 46.B). Indeed, accommodation of the second aromatic ring of the naphthyl substituent would need an adaptation of the subpocket which is only required at MT_1 receptor, as evidenced by the increase in two monitored distances.

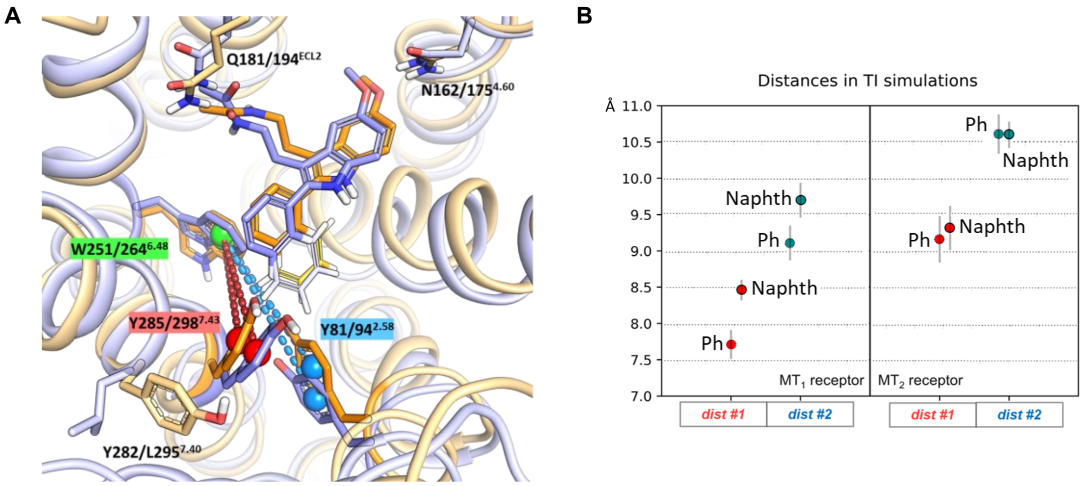

Figure 46. Representative snapshots of TI simulations performed with λ=0.0092 (**A**). MT_1 and MT_2 receptors with the bound alchemical ligands (2-PhMLT and compound **26**) are shown with orange and purple cartoons and sticks, respectively. Unique atoms, in which the Coulomb and Van der Waals potentials have been replaced with softcore potentials are depicted with lighter shades of the two colours. Distances between centroids of select aromatic residues within the subpocket are represented: *i*) dist #1 between the COMs of $W251/264^{6.48}$ indole carbocycle (green spheres) and of $Y285/298^{7.43}$ phenyl ring (red spheres) and *ii*) dist #2 between the first COM and another one defined on $Y81/94^{2.58}$ phenyl ring heavy atoms(cyan spheres). The two distances and their S.E.M. are monitored in the endpoint simulations (**B**), defined by λ=0.0092 (Ph) and λ=0.9978 (Naphth).

Instead, the subpocket at the MT_2 receptor would already be wide enough to be occupied by the α-naphthyl group without an additional energetic cost to adapt the binding site. This difference at the two receptor subtypes could be due to the presence of a nonconserved pair of residues belonging to TM helix VII, i.e., $Y282/L295^{7.40}$ (Figure 46.A). Crystal structures show that Y282 in the MT_1 receptor points toward TM helices I and II, restricting the space available to $Y81^{2.58}$ and $Y287^{7.43}$, which protrude inside the subpocket.

Conversely, in the MT_2 receptor, $L295^{7.40}$ is oriented toward the opposite side of the TM helix VII and the membrane lipid bilayer, allowing for the two residues $Y81^{2.58}$ and $Y287^{7.43}$ to be placed in a more retracted position consenting wider out-of-plane substituents in the subpocket.

The application of alchemical simulations here described, while being a limited case, might be employed to obtain free-energy differences related to receptor subtype selectivity of specific classes of ligands. Similarly, free-energy perturbation simulations have been used to distinguish between ligand selectivity for A_{2A} receptor active or inactive state. [266,267] Therefore, changing the thermodynamic cycle of such calculations can result in a flexible and useful physics-based scoring tool that can be employed in drug discovery pipelines, provided that other issues, including the lack of convergence, the low-quality of ligand force-field parameters and the unfeasibility of the transformation, would not arise.

6.2.3 Atropisomers reveal multiple arrangements inside the 2-phenyl binding pocket

The lack of stereoselectivity seen for the two atropisomers (R_a)-**32** and (S_a)-**32** (Table 5) points out to the α-naphthyl substituent being able to occupy the hydrophobic subsite with both arrangements perpendicular to the indole ring plane. Therefore, while atropisomers axial chirality usually has a strong impact on the biological activity and target engagement, this does not appear to be the case for α-naphthyl compounds within the series. In fact, both of them maintained a partial agonist activity of the derivative with unhindered rotation of the α-naphthyl substituent. To justify the similar binding affinity achieved by the two naphthyl derivatives, induced-fit docking (IFD) calculations are performed within the MT_2 receptor binding site.

Docking poses of the two compounds resulted in a similar IFD score (-564.6 and -563.5 kcal/mol for (R_a)-**32** and (S_a)-**32**, respectively), conserving the ethylamide chain geometry and the indole ring position of the co-crystalized 2-PhMLT (Figure 47.A). Both arrangements of the α-naphthyl group were allowed within the subpocket, minimally altering side chains of $M120^{3.32}$, $L267^{6.51}$ and $Y298^{7.43}$ to differently accommodate the substituent.

The naphthyl substituent of compound (R_a)-**32** points in the direction opposite to that of the ethylamide chain, as in pharmacophore model of ref. 142, extending toward the cytosolic side of the receptor, and close to $Y298^{7.43}$ and $M120^{3.32}$. Instead, (S_a)-**32** places the substituent toward the extracellular portion of the receptor, facing $L267^{6.51}$ and $Y294^{7.39}$.

The two complexes in 200 ns-long MD simulations confirmed the stability of the docking poses and of hydrogen bonds established by the two atropisomers (Figure 47.B). Analysis of α carbons root-mean-square fluctuations (RMSF) demonstrate the stability of the TM bundle and of the ECL2, which seals the top of the binding site (Figure 47.C). The simulations are consistent with the similar affinity of the two compounds, supporting the existence of multiple arrangements for the 2-aryl substituents occupying the 2-phenyl binding pocket.

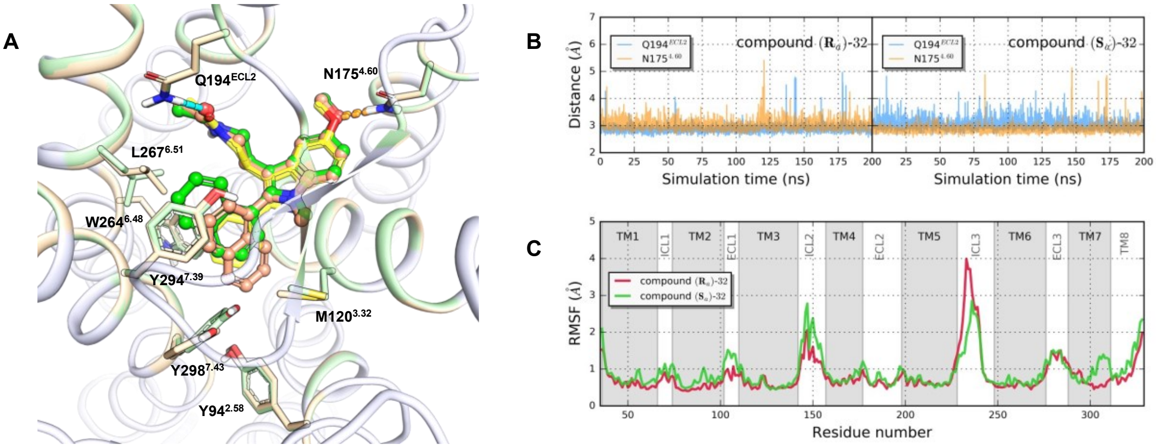

Figure 47. Energy-minimized induced-fit docking complexes of the MT_2 receptor (purple cartoon with red and green regions depending on the conformational changes caused by the IFD protocol) bound to atropisomers (R_a)-**32** (red carbons) and (S_a)-**32** (green carbons). Co-crystalized 2-PhMLT (PDB id *6ME6*) is represented with yellow carbons. Hydrogen bonds with $Q194^{ECL2}$ (cyan dashes) and $N175^{4.60}$ (orange dashes) are represented and monitored in MD simulations (**B**, lines with the same colour). Root-mean-square fluctuation (RMSF) of the protein alpha carbons during simulations shows stability of the TM bundle (**C**). The grey background identifies residues belonging to the TM bundle.

6.2.4 Water distribution inside the binding pocket rationalize binding affinity of aza-heterocycles substituents

Compounds **29**, **30** and **31**, having a 2-aza-heterocycle as a substituent occupying the 2-phenyl binding pocket, were docked within the MT_2 receptor binding site. The 3-pyridyl derivative **29** was the most potent ligand at both receptors, mirroring the activity achieved by bioisosteric 2-PhMLT. Compounds **30** and **31**, being substituted with bicyclic aryl rings, achieved a selectivity toward the MT_2 receptor, as expected on the basis of the analogy with compound **26** and of SARs of melatonergic ligands. [102] Interestingly, the 5-quinolyl derivative **30** achieved a ten-fold lower MT_2 binding affinity than its 4-indolyl analogue **31**. Docking score (Table 6) could not reproduce a ranking consistent with binding affinity data, nor any polar interaction undertaken by the three substituents could be seen in their binding poses. In particular, no reason for the loss of affinity of compound **30** with respect to compound **31** was apparent.

Table 6. Docking scores for 2-heteroaryl indole derivatives.

Compound	**GScore (kcal·mol^{-1})**
29	-10.95
30	-10.80
31	-10.51

To investigate the role of aza groups, the three complexes were submitted to MD simulations for 200 ns, in which no direct anchoring of the heteroaryl nitrogens to polar residues comprised in the binding pocket was observed. However, a different distribution of the water molecules within the binding site was observed. The 3-pyridyl substituent of compound **29** could rotate and interact with water molecules, either proceeding from the extracellular bulk or from the internal pockets of the TM domain (Figure 48.A). Instead, the quinoline nitrogen of compound **30** faced a hydrophobic portion of TM helix VII (Figure 48.B), resulting in no interaction with either protein residues or the water molecules within the binding site. In contrast, the indole nitrogen of compound **31** undertook a quite stable water-bridged interaction with the hydroxyl group of Y94$^{2.58}$ (Figure 48.C), likely leading to the higher binding affinity compared to compound **30**. Analysis of the distribution of water molecules within the binding pocket during MD simulation highlights the absence of solvent molecules within a shell of 4 Å from the nitrogen atom of compound **30** (Figure 48.D). This finding supports the ten-fold higher affinity of compound **31**, identifying a polar residue in the aromatic subpocket able to interact with hydrophilic groups.

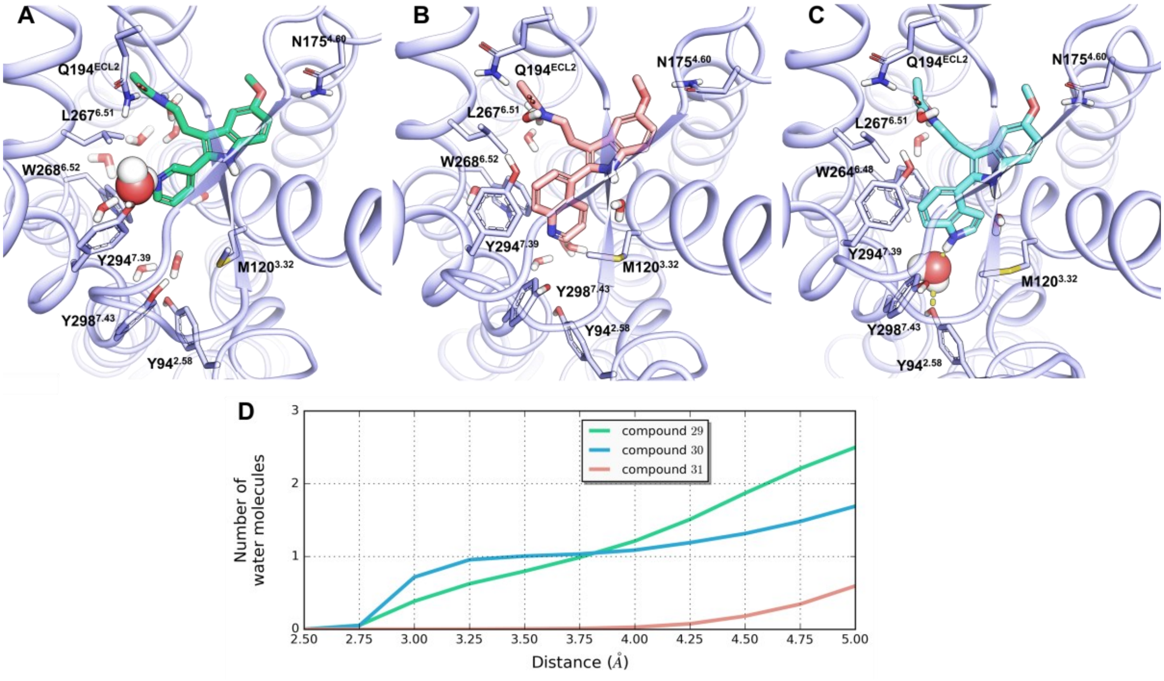

Figure 48. Binding modes achieved in MD simulations by 2-substituted indole derivatives **29** (**A**), **39** (**B**) and **31** (**C**). Water molecules directly contacting the heteroaryl nitrogens are represented with their Van der Waals radii and hydrogen bonds are represented with yellow dashed lines. Analysis of the water distribution along 200 ns is shown (**D**), by monitoring distances between heavy atoms.

6.3 RESULTS AND DISCUSSION: N-ANILINOETHYLAMIDES WITH INCREASED WATER SOLUBILITY

6.3.1 Biological activity and structure-activity relationships of N-anilinoethylamides with increased water-solubility

In a series of N-anilinoethylamides (Table 7), different strategies were pursued in order to enhance the water solubility with respect to UCM765 and UCM924:

i) insertion of 4-pyridil substituents in place of UCM765 phenyl ring in compound **38**,

ii) design and evaluation of the phenyl-alkylamide scaffold in lieu of the diphenyl-alkylamide one for compounds **40** and **41**. In compound **40** the scaffold was utterly changed, by moving the *N*-phenyl substituent on the anisole ring in the para position with respect to the methoxy group. In the case of compound **41**, the phenyl substituent was replaced with a bromine to increase the metabolic stability.

iii) insertion of hydrophilic groups on the phenyl ring potentially accommodated in the aromatic subpocket, such as the hydroxymethyl and hydroxyl groups in compound **42** and **43**, respectively.

In vitro pharmacology was conducted at Cerep (Celle-Lévescault, France), including binding affinity and efficacy assays. Binding affinities were determined displacing 2-[^{125}I]-iodomelatonin in competition experiments on human MT_1 and MT_2 receptors expressed in CHO cells. [268,269] Regarding the efficacy assays, agonist activity at MT_1 receptors was evaluated using a cell impedance assay exploiting cellular dielectric spectroscopy, [268] and at MT_2 receptors using a cAMP assay via a fluorometric method. [269]

Urea derivatives **33-35** (Table 7) had a reduced binding affinity, especially at the MT_1 receptor. The most potent compounds of the three was compound **34**, achieving a binding affinity at the MT_2 receptor similar to that of UCM765. The lower affinity of the urea analogues compared to the amide derivatives is comparable to the one of agomelatine and its structural analogues [270,271] or tetrahydroquinoline derivatives. [123]

Table 7. Binding affinity of *N*-anilinoethylamide melatonergic ligands

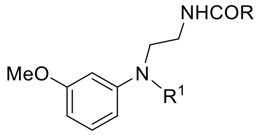
33-35, **37-39**, **42-43**

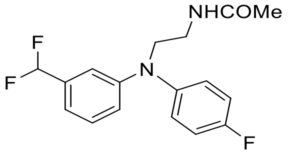
36

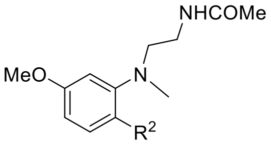
40-41

Compound	**R**	**R^1**	**R^2**	**MT$_1$ receptor K_i (±SD) [nM]**	**MT$_2$ receptor K_i (±SD) [nM]**
UCM765	-	-	-	1.6 ± 0.14	0.29 ± 0.10
UCM924	-	-	-	>100	1.4 ± 0.08
33	NH_2	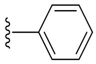	-	>100	10 ± 0.13
34	NHEt	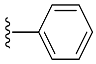	-	20 ± 0.45	0.65 ± 0.03
35	NHnPr	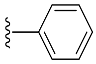	-	57 ± 0.10	1.7 ± 0.08
36	-	-	-	> 100	35 ± 0.35
37	Me	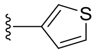	-	0.7 ± 0.1	0.07 ± 0.02
38	Me	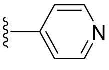	-	> 100	> 100
39	Me	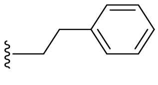	-	> 100	2.1 ± 0.15
UCM1094, 40	-	-	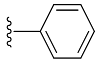	32 ± 0.80	1.7 ± 0.13
UCM1095, 41	-	-	Br	18 ± 0.70	2.4 ± 0.10
UCM1118, 42	Me	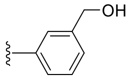	-	>100	3.5 ± 0.05
UCM1119, 43	Me	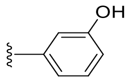	-	53 ± 1.6	1.4 ± 0.15

[a] K_i values are calculated from IC_{50} values obtained from competition curves by the method of Cheng and Prusoff [243] and are the mean ± S.D. of three determinations.

Instead, the replacement of the methoxy group in compound **36** led to a reduced binding affinity. The 3-thienyl group in compound **37** provided a good alternative to UCM765 phenyl substituent, resulting in the most potent compound of the series. Considering monophenyl-alkylamide derivatives, the phenethyl-substituted derivative **39** was only tolerated at the MT_2 receptor, while compounds **40** and **41** achieved a good binding activity at both receptors.

Compounds **38**, **42** and **43** bearing hydrophilic substituents were not tolerated at the MT_1 receptor, while the introduction of a hydroxy-methyl or of a hydroxyl group in meta position of the phenyl ring brought to a limited reduction of binding affinity at the MT_2 receptor. These more basic phenyl-alkylamide derivatives **40** and **41** and hydroxyl-substituted derivatives **42** and **43** attained an increased water solubility (Table 8) with respect to UCM765 and UCM942, while conserving a good binding affinity at the MT_2 receptor.

Table 8. Experimental lipophilicity and solubility measurements of N-anilinoethylamides reported in Table 7.

Compound	**Solubility pH 1.0 [µg/mL]**	**Solubility pH 7.4 [µg/mL]**	**Log $D_{oct,7.4}$** [b]
UCM765	125 ± 5	104 ± 5	2.93 ± 0.01
UCM924	6.9 ± 0.1	5.1 ± 0.2	3.84 ± 0.05
33	363.9 ± 3.7	311.4 ± 2.6	2.65 ± 0.02
34	14.9 ± 9.6	10.2 ± 1.7	3.30 ± 0.02
35	17.7 ± 0.9	14.3 ± 0.1	3.91 ± 0.02
36	54.9 ± 1.1	40.6 ± 0.1	3.45 ± 0.02
37	161.5 ± 4.4	92.5 ± 3.5	2.74 ± 0.01
38	> 1000 [a]	1019.6 ± 93.7	0.41 ± 0.01
39	> 1000 [a]	109.6 ± 6.9	3.44 ± 0.02
UCM1094, 40	> 1000 [a]	339.5 ± 9.7	3.11 ± 0.02
UCM1095, 41	> 1000 [a]	822.9 ± 34.7	1.85 ± 0.01
UCM1118, 42	> 1000 [a]	> 1000 [a]	2.04 ± 0.01
UCM1119, 43	95.9 ± 4.2	118.7 ± 2.8	2.42 ± 0.02

[a] Weighted compound completely dissolved in the chosen buffer at 1000 µg/mL. Experiments were performed in triplicate and values are reported as the mean ± S.D. Thermodynamic solubility values were measured in two different buffers (pH 1.0; pH 7.4) by the shake flask method. [272] [b] Reported log $D_{oct,7.4}$ values are the mean of three measurements ± S.D., at R.T.

The high binding affinity and selectivity for the MT_2 receptor shown by compounds in Tables 4 and 7 follows the general trend of other 2-substituted compounds, reported in Chapter 2.5.3. Compounds **40** (Figure 49) and **41** have the phenyl and bromine substituents superimposed to the phenyl ring of co-crystalized 2-PhMLT and docked UCM765 in docking calculations, highlighting their complementarity with the binding pocket.

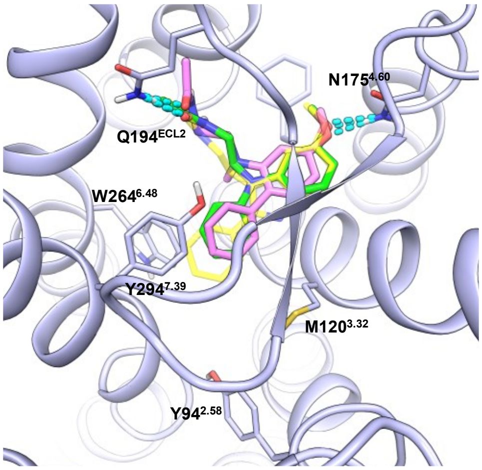

Figure 49. Ligand binding mode obtained via docking calculation within the MT_2 receptor binding site. UCM765 is represented with green carbons. Compound **40** (UCM1094) is represented with pink carbons. The phenyl substituents are superimposed to the one of co-crystalized 2-phenylmelatonin (PDB id *6ME6*), which is shown with shaded yellow carbons. Hydrogen bonds between receptor and docked ligands are shown as cyan dashed lines.

6.3.2. A TMII residue in the aromatic subpocket proposed as a putative polar contact for hydrophilic groups

Despite being a lipophilic region, the previous heteroaryl derivatives (Paragraph 6.2.4) show that the interaction with water molecules or polar groups of protein residues with hydrophilic substituents is tolerated and led to a reduced decrease of the ligand binding affinity at the MT_2 receptor with respect to MT_1 receptor. Like compound **23**, which bears a hydroxyl substituent on the 3-phenyl naphthalene scaffold, compounds **41** and **42** should accommodate hydroxyl groups in the aromatic subpocket. In particular, compound **42** had a strongly lowered binding affinity at the MT_1 receptor. Compound **42** was docked at the MT_2 receptor, reproducing the usual hydrogen bonds between the methoxy group and N175$^{4.60}$ and between the amide group and Q194^{ECL2}, while no interaction was observed for the hydroxymethyl substituent.

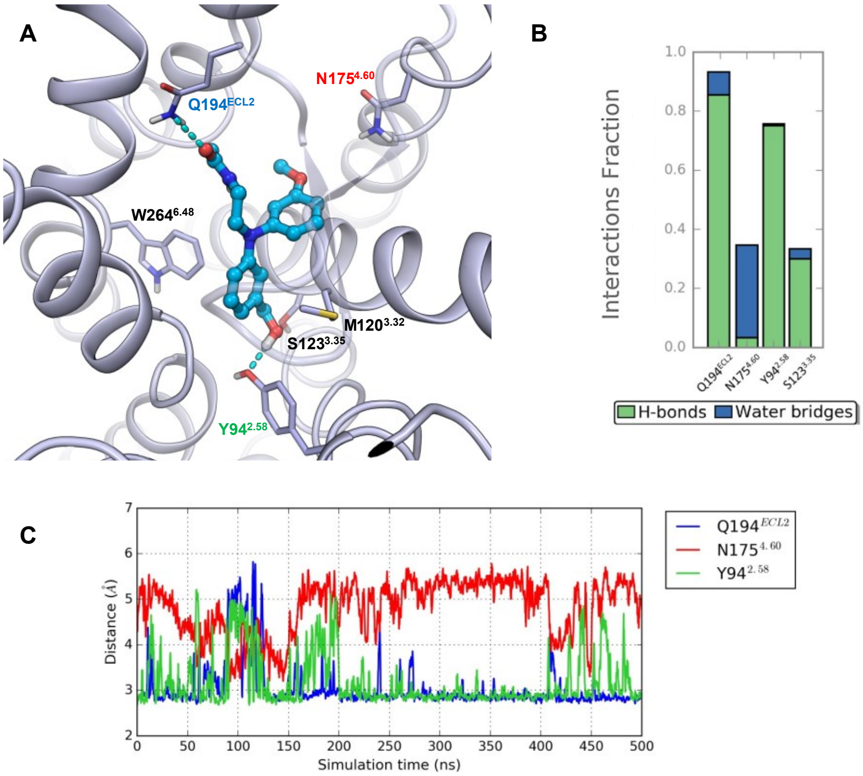

Figure 50. Binding mode of compound 42 within the MT$_2$ receptor achieved during a 500 ns-long MD simulation, evidencing the polar contact between the hydroxymethyl substituent and Y94$^{2.58}$ (**A**). Polar interactions of the ligands are considered analysing the frequency of direct and water-mediated hydrogen bonds (**B**) and the distance between heteroatoms of the amide side chain, the methoxy and hydroxymethyl groups of the ligand with Q194^{ECL2}, N175$^{4.60}$ and Y94$^{2.58}$, respectively (**C**).

During a 500 ns-long MD simulation (Figure 50), the ligand moved toward the TM helices II and III, losing the hydrogen bond with N175$^{4.60}$ and forming another one with Y94$^{2.58}$, while maintaining the polar contact with Q194^{ECL2}. The former residue would be located in a hydrated portion of the binding site, including S123$^{3.35}$, another residue occasionally contacted in the simulation by the hydroxymethyl group. The additional hydrogen bond contact with Y94$^{2.58}$ and the partial loss of the interaction with N175$^{4.60}$ would justify the limited affinity reduction at the MT$_2$ receptor, conserving the selectivity at this receptor subtype of the parent compound (UCM765).

6.4 CONCLUSIONS AND FUTURE PERSPECTIVES

In this chapter, some aspects related to the molecular requirements to achieve high binding affinity and selectivity at the MT_2 receptor were thoroughly analysed. Moreover, attempts to increase water solubility, a major issue in the development of melatonergic ligands, was considered in these points. A series of 2-substituted-indole ligands turned out to be a useful tool to probe the steric and physicochemical requirements and tolerance of the MT_1/MT_2 receptor subpocket, accommodating the phenyl ring of 2-PhMLT in crystal structures. The new 2-aryl derivatives **24**, **25** and **26** shows that the selectivity, and the partial loss of intrinsic activity of partial agonists, is related to the occupation of the subpocket with out-of-plane substituents, coherently with previous ligand-based studies. In particular, thermodynamic integration transforming 2-PhMLT into compound **26** shows the importance of the different dynamic flexibility of the aromatic subpocket at the two receptor subtypes, an aspect that is not clearly understood from crystal structures, which are not obtained with subtype-selective ligands. At the MT_1 receptor, the re-shaping of the subpocket, required to accommodate bulky substituents, proved to be an energy-consuming process likely responsible for the loss of affinity of MT_2-selective compounds.

Moreover, atropisomers (*R_a*)-**32** and (*S_a*)-**32** highlighted that the additional volume accessible at the MT_2 receptor is quite diffused across the region delimited by TM helices II, III and VII. The out-of-plane α-naphthyl group was able to accommodate at both sides of the region, either close to $W264^{6.48}$ or pointing toward the extracellular side of the binding pocket.

Aza-derivatives **29** and **31** and hydroxy-substituted compounds **40** and **41** evidence the tolerance of the aromatic subpocket to hydrophilic groups, which could be more pronounced at the MT_2 receptor. Moreover, simulations identified $Y94^{2.58}$ at the MT_2 receptor as a polar residue able to interact with hydrophilic substituents, resulting in potent ligands with improved physicochemical properties. With this aim, the introduction of hydroxyl groups could be useful to eventually design prodrugs.

6.5 COMPUTATIONAL PROTOCOLS

6.5.1 Docking calculations

Docking of compounds **29**, **30**, **31**, **40** and **42**

Docking grid was prepared from structure of the MT_2 receptor in complex with 2-PhMLT (Appendix 1), imposing bounding and enclosing boxes of 10 and 20 Å, respectively, centred on the co-crystalized ligand. Docking calculations were performed with Glide 7.9 [190,191] in standard precision mode. Parameters controlling pose retention after the rough scoring stage for refinement and post-dock minimization stages were increased tenfold from default values. Default scaling of the van der Waals radii was applied only on nonpolar atoms, i.e., having a partial charge lower or equal to |0.15|. Docking of reference compound UCM765 has been performed with the same settings.

Induced-fit docking of (*R_a*)-**32** and (*S_a*)-**32**

A protocol called "induced-fit docking" [273] was adopted to predict the binding mode of (S_a)-**12** and (R_a)-**12** within the MT_2 receptor binding site. The grid was centred on the co-crystallized 2-PhMLT, setting the dimension of the bounding box to 10 Å to restrain the position of the centre of mass of the two atropisomers during the first rough docking calculation. During this step, docking was performed with softened potential, i.e., van der Waals radii were scaled by a factor of 0.7 for protein atoms and 0.5 for ligand atoms. The obtained ensemble of poses was retained as input for a protein structural optimization procedure, [274] performed with OPLS3e force field [193] and implemented in with Prime 5.2. [248] The procedure consisted in 5 cycles of conformational search with OPLS3e molecular mechanics potentials applied to all the residues inside a shell of 5 Å from the initial ligand poses and followed by Truncated Newton minimization [275] in VSGB2.1 implicit solvation model. The two residues undertaking hydrogen bonds with the ligands, i.e., $N175^{4.60}$ and Q194, were not considered in the procedure and were kept in fixed conformation. The two atropisomers were then re-docked in the refined binding sites with Glide default scaling factors [191]. Both docking stages were run applying restraints on the two hydrogen bonds undertaken by the methoxy and amide groups. The complexes thus retrieved were ordered according to the IFD score, a composite score accounting for the receptor-ligand interaction energy after re-docking and the total energy of the complex after the structural optimization stage, which additionally considers receptor strain and solvation terms computed in the VSGB2.1 continuum.

6.5.2 Molecular dynamics simulations of receptor-ligand complexes

After energy minimization of the receptor-ligand complexes to an energy gradient of 0.01 $kJ \cdot mol^{-1} \cdot Å^{-1}$, MD of MT_2 receptor complexes with compound **29**, **30**, **31** and (R_a)-**32** and (S_a)-**32**, as well as complexes between the two melatonin receptors and UCM1014 enantiomers, have been run with Gromacs 2019.4 MD engine, [202] using ff14sb Amber force field, [196] as reported in Paragraph 4.2.1. Instead, MD simulation of MT_2 receceptor bound with compound **42** was performed with Desmond 5.4 [251] and OPLS3e force field, [193] using protocol reported in Paragraph 5.5.2. Systems, in which the receptors are bound with (*R*)-UCM1014 and (R_a)-**32**, (S_a)-**32**, are pre-equilibrated with simulations performed in μVT ensemble [155] to hydrate the orthosteric site, prior to simulations.

6.5.3 Thermodynamic integration simulations

Crystal structures of MT_1 and MT_2 receptor complex with 2-PhMLT (PDB id *6ME3* [74] and *6ME6* [75]) were used to prepare the systems as described in Appendix I. Alchemical transformation of the phenyl ring into the α-naphthyl one of compound **26** was performed with Amber20 pmemd.cuda TI module. [183] Membrane and system preparation and parametrization followed the protocol reported in Paragraph 4.2.1. OPLS partial atomic charges [193] were assigned to the ligands. Notably, TIP3P water models were used as in ref. 276. MD simulations were run in NPT ensemble: temperature was enforced at 298 K by Langevin thermostat [277] with a collision frequency of 2 ps^{-1}; pressure was kept at 1 bar by using the Monte Carlo barostat [278] with a pressure relaxation time of 2 ps. For each system, four snapshots were extracted after 10-25 ns of production and the coordinates were used to prepare dual ligand topologies.

For unique atoms (two hydrogens of 2-PhMLT, four carbons and four hydrogens of compound **26**), Lennard-Jones and Coulomb potentials were replaced with softcore potentials. [181] Parameters α and β, respectively modulating the Van der Waals and electrostatics in eqs. 3.32 and 3.33 were set to 0.5 and 12 $Å^2$.

Snapshots were submitted to an initial equilibration performed at λ=0.5, to prepare the inputs for the proper TI simulations. The equilibration included:

i) 5,000 steps of steepest descent minimization with protein backbone restrained with 1.0 $\mathrm{kcal \cdot mol^{-1} \cdot Å^{-2}}$;
ii) 100 ps in NVT ensemble with gradual heating to 298 K with Berendsen thermostat keeping the restraints on the backbone atoms;
iii) 100 ps in NVT ensemble with restraints applied to backbone heavy atoms lowered to 0.1 $\mathrm{kcal \cdot mol^{-1} \cdot Å^{-2}}$;
iv) 1,000 ps NPT MD with same conditions of the production.

Then, twelve simulations were run at different λ values (0.00922, 0.04794, 0.11505, 0.20634, 0.31608, 0.43738, 0.56262, 0.68392, 0.79366, 0.88495, 0.95206, 0.99078), using the single-step scheme. [183] Random velocities were assigned at 5 K and the systems were gradually heated in 400 ps to 298 K, followed by 100 ps at constant temperature. Simulations were performed in the NPT ensemble, with the conditions described above. The SHAKE algorithm was disabled, requiring an integration timestep of 0.001 ps. After 5000 ps, $\partial V/\partial \lambda$ values, which were registered each ps of simulation, were averaged for each window and multiplied for the weight assigned to each λ value. All simulations were performed on NVIDIA RTX3070 graphics cards.

Chapter 7. Functionally selective ligands impact on the MT_2 receptor activation free-energy landscape

7.1 INTRODUCTION

7.1.1 Class A GPCRs activation in MD simulations

The availability of several crystal structures of Class A GPCRs in both the active and inactive state provides evidence of the major determinants related to the process of receptor activation. A major breakthrough in this field was possible with the first structures of a non-opsine receptor, the β_2-adrenergic receptor, being captured bound to an inverse agonist [279] and to the G_s protein. [97] From that moment, a number of receptors have been co-crystalized in both conformational states, in turn characterized by highly conserved conformational changes of the TM bundle. [280] During the last decade, different simulative approaches have been applied to investigate the mechanism of receptor activation. Unbiased MD simulations performed by Dror et al. [281,282] in the timescale of the microsecond captured the relaxation of the agonist-bound binary complex into the inactive conformation. However, to characterize intermediate states or alternative transitions and evaluate the impact of ligands on the receptor conformational state, enhanced sampling protocols and algorithms for data analysis have been employed. [283] MD simulations approaches included MetaD-based [283] and string method with swarm of trajectory [284,285] protocols. Filizola's group applied a MetaD-based protocol consisting of the application of PCVs [169] in the RMSD [286,287] or in the contact map space, [288] starting from a frameset retrieved via ABMD simulations, during which the TM bundle was forced into the active or inactive conformation. *wt*-MetaD with the multiple-walker implementation was applied to study the activation of a class B GPCR, the glucagon receptor, [289] evidencing the preeminent role of the *N*-terminal portion of TM helix VI, whose outward movement is considered a general hallmark for the activation of all GPCRs superfamilies. Interestingly, these simulations showed an allosteric coupling between the two ends of the TM bundle, as the binding of the G-protein to the intracellular side strongly stabilized the transition toward the active state of the receptor.

7.1.2 Scientific rationale

The aim of this project, conducted in collaboration with the Biomolecular and Pharmaceutical Modelling group of Prof. Francesco Luigi Gervasio at the University of Geneva, focused on the application of MetaD-based protocols to study the free-energy landscape of the activation of the MT_2 receptor. Therefore, simulations were performed to study the activation process of binary complexes (receptor and ligand, in the absence of the G-protein) of the MT_2 receptor with prototypical ligands, indole-based agonist IIK7 and antagonist K185 (Figure 11). [135] The two compounds share a tetracyclic structure in which the indole of melatonin has been expanded to include a phenyl ring, topologically corresponding to the phenyl ring of 2-phenylmelatonin, which has been connected to the indole nitrogen through a 5- or 7-membered ring . As thoroughly described in Chapter 6, ligands occupying the aromatic pocket of the binding site usually achieve a higher binding affinity and, depending on the structure and arrangement of the substituent, selectivity for the MT_2 receptor. Therefore, the choice of the ligands for these simulations draws on established structure-activity relationships to determine the impact of their binding mode on the conformational space of the receptor. A major difference between the two ligands is due the different ring connecting the indole with the condensed phenyl ring. Moreover, the angle between the phenyl ring and the indole plane is wider for the antagonist due to the presence of the seven-membered cycle replacing the five-atom ring of the agonist and forcing the phenyl in an out-of-plane arrangement. The presence of such out-of-plane substituent might influence the exploration of alternative free-energy minima along the activation pathway. Identification of ligand-induced metastable states, [285,287] that cannot be observed in crystal structures, and investigation of the role of the microswitches in the conformational change, [290] might provide relevant information for the design of novel ligands with finely tuned behaviour.

7.2 RESULTS AND DISCUSSION

7.2.1 Molecular dynamics of MT_2 receptor complexes with prototypical ligands

Binary complexes of the MT_2 receptor bound to agonist IIK7 or antagonist K185 were obtained via docking calculations (Figure 51) performed on the protein structure prepared from the active ternary complex in which a G_i protein is present (see Appendix IV). [52] MD simulations of the complexes of the MT_2 receptor bound to the two ligands verified the stability of the binary complexes in their active conformation in μs-long plain MD. In particular, even the complex of the active MT_2 receptor bound to the antagonist K185 could not access any alternative state, suggesting an impeding conformational transition toward the inactive state. Indeed, the stability of both the TM domains and the ligand binding poses were maintained during the simulations of the two active complexes. RMSF analysis showed that 110 α carbons over a total of 223, comprised in the seven helices of the TM domain, had a fluctuation lower than 0.75 Å (Figure 52). This group of α carbons was selected for re-alignment of RMSD-based *CV*s, according to the Kearsley optimal alignment matrix. [208]

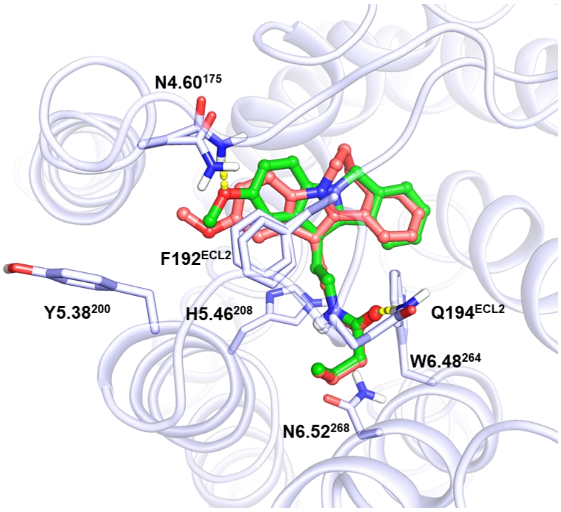

Figure 51. Binding mode of IIK7 (green sticks) and K185 (red sticks) within the binding site of the MT_2 receptor (white cartoon and sticks, PDB id *7VH0*). Hydrogen bonds are represented with yellow dashed lines.

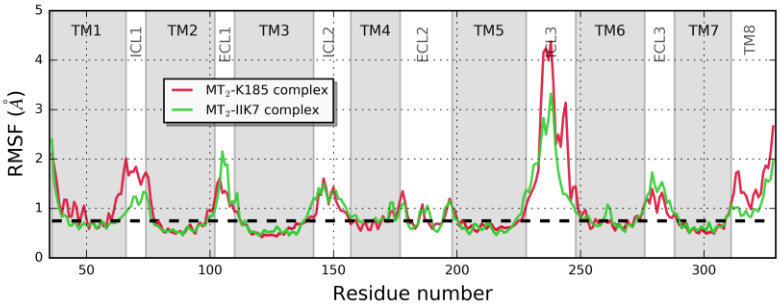

Figure 52. Stability of the TM domain of the MT_2 receptor during MD simulations of the active binary complexes with the agonist IIK7 and the antagonist K185. The area with grey background comprises residues inside the TM domain. RMSF analysis is performed for the 200-1000 ns interval. Residues with a RMSF lower than a 0.75 Å cut-off were used to perform the re-alignment of RMSD-based *CV*s.

MD simulations confirm the more pronounced out-of-plane deviation (48±7°) of the condensed phenyl ring of K185, accommodated at the hydrophobic subsite comprised between TM helices II, VI and VII, in comparison with the nearly in-plane arrangement for IIK7 (26±10°). This difference is due to the condensed azepine ring, controlling the angle between the planes of the phenyl ring and the indole plane. Two alternative conformations are accessed by the ring, according to values assumed by dihedral angles τ_1, τ_2 and τ_3, defined according to Figure 52. $\tau_1 \sim 60°$, $\tau_2 \sim -30°$ and τ_3 -40° lead to a boat-like conformation that would be more energetically stable than the pseudo-boat conformation ($\tau_1 \sim 0°$, $\tau_2 \sim 45°$ and $\tau_3 \sim -80°$). Instead, τ_4 assumes the same value (~60°) for the two conformations of the heptatomic ring both, allowing the same inclination and orientation of the out-of-plane phenyl ring (Figure 53), in turn able to establish a π-π interaction with Y298$^{7.39}$.

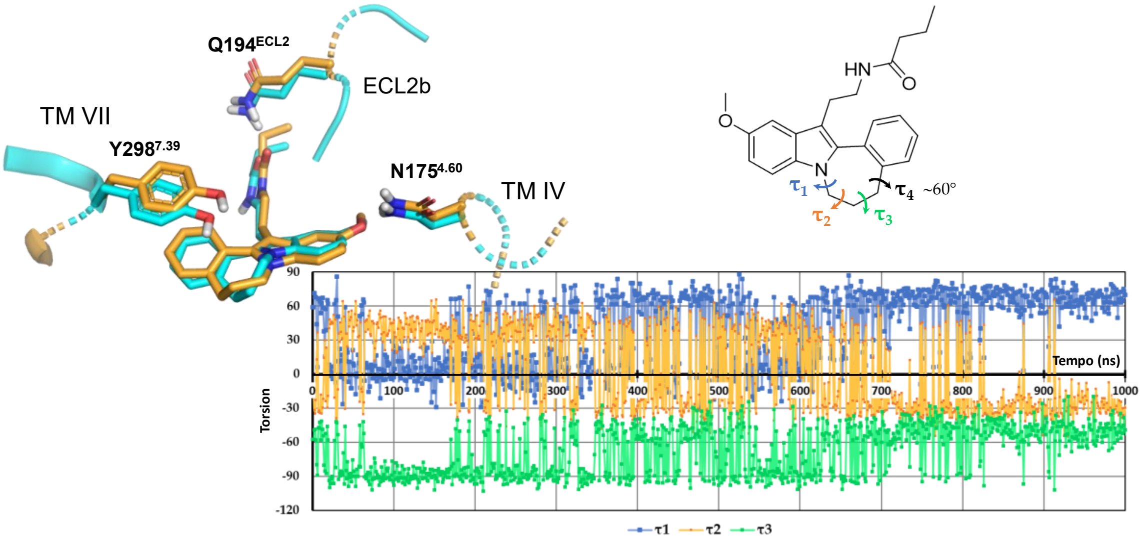

Figure 53. Conformational analysis of K185 bound within the binding site of the active state of the MT$_2$ receptor during a μs-long MD simulation. Dihedral angles of the heptatomic ring of the 6,7-dihydro-5*H*-benzo[3,4]azepino[1,2-*a*]indole scaffold are monitored. K185 and surrounding residues are shown with the heptatomic ring in cyan and orange conformations, defining "boat" and "pseudo-boat" conformations.

ABMD simulations are employed to force the TM bundle of the two complexes in their inactive conformation, which is then relaxed with unbiased simulations. Since the target structure for the simulations was the thermostabilized inactive structure, [74] the TM helix

VIIb and the NAXIY motif assumed a slightly different backbone geometry with respect to the reference template, due to the presence of a proline instead of an alanine in position $305^{7.50}$. However, ABMD simulations permitted to initiate *wt*-MetaD simulations from both receptor functional states.

7.2.2 MT_2 receptor activation free-energy surface

Multiple-walker MetaD simulations were performed adopting *CV*s describing the conformational transition between the active and the inactive state of the receptor. Two RMSD-based variables, described in Paragraph 7.4.5, account for the movement of the TM helices Va, VIa and VIIb. The first portion of the TM helix V should control the movement leading, upon receptor activation, to a reduction of the volume of the orthosteric binding site and to a decrease of the so-called TM V bulge, which is due to the kink introduced by $P212^{5.50}$. This inward bulge is quantified as the distance between the α carbons of $H208^{5.46}$ and $L296^{7.41}$. Instead, the cytoplasmic halves of the TM helices VI and VII control the formation and disappearance of the surface area contacting the G_i protein. Displacement of these helices during the simulations, called *macroswitches*, [290] would largely account for the receptor conformational change. Keeping into account these preliminary considerations, after 3.0 μs of simulation (cumulative time given by the exploration performed by all the walkers), FES of the two systems were analysed (Figure 54.A-B) and convergence of its time series of the reprojection over PROG (definition in Paragraph 7.4.5) was achieved during the second half of the simulation. The resulting free-energy difference between the active and inactive states of the two complexes amounted to around 8 $kcal \cdot mol^{-1}$, strongly favouring the active conformation of the receptor. This could be due to an inherent high basal activity attributed to melatonin receptors, [80,81] and to constitutive coupling to the G-protein. Additionally, this behaviour of the receptor would be corroborated by the characterization of inverse agonists selective for the MT_2 receptor. [143]

However, it is more probable that such a high free-energy difference could be related to hysteresis along the *CV* describing the progress of the transition, as RMSD-based variables could offer a rough description of such a complex transition. This aspect will be deepened in the next paragraph.

One of the most important differences between the two systems is related to the absence or presence of a free-energy minimum at intermediate coordinates of the PROG *CV*. Moreover, the binary complex MT$_2$-IIK7 is characterized by a third free-energy minimum, roughly at the same energetic level of the inactive one (Figure 53.A), suggesting an easier transition between the two functional states of the receptor and a lower free-energy barrier required for the activation, coherently with the activation mechanism proposed for the β$_2$-adrenergic receptor. [291,292]

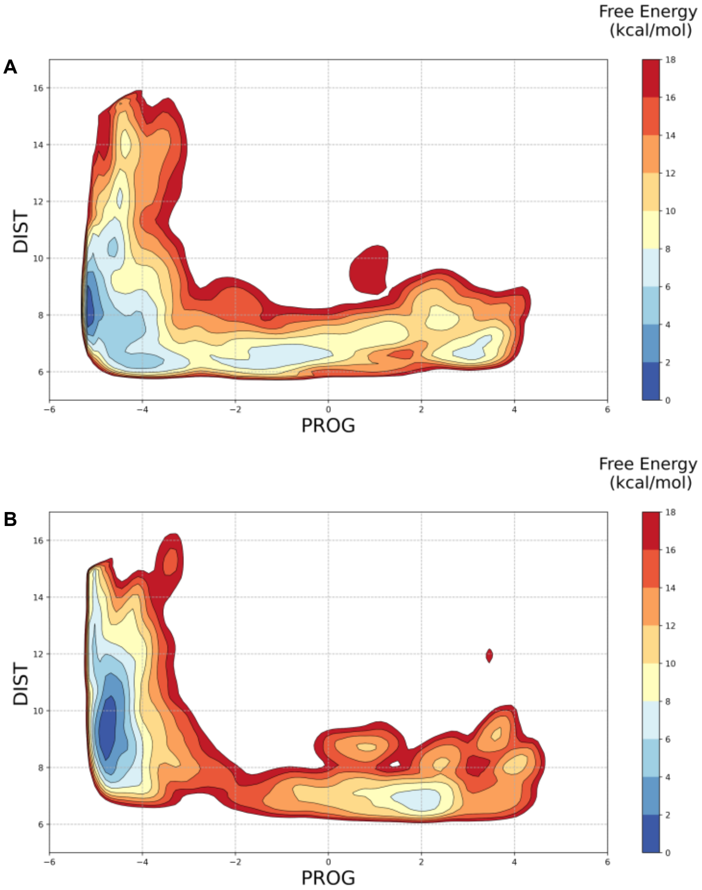

Figure 54. Free-energy landscapes of the activation of the MT$_2$ receptor bound to IIK7 (**A**) and K185 (**B**), obtained via multiple-walker *wt*-MetaD.

Clustering of the α carbons of the *N*-terminal region of TM helix VI performed on the snapshots falling inside this free-energy minimum (Figure 54.A, loosely corresponding to $-2 < \text{PROG} < 0$) revealed that the most populated cluster is still comparable to the active state of the receptor. However, in this free-energy basin, less populated clusters showed that the cytoplasmic end of the TM helix VI is situated at an intermediate distance from the TM helix III (Figure 55), with respect to the active and inactive configurations. Contemporarily, the backbone of the NAXIY motif assumed the twist characterizing the active-like conformations (Figure 56.A) at intermediate PROG values, infrequently accessed by the antagonist-bound complex (Figure 56.B), as shown by reweighting of the microswitch, defined as the heavy atoms of the residue sidechains belonging the motif. In fact, shifting between the two alternative states of the TM helices VIa and VIIb could be sufficient to explore some of the alternative degrees of freedom, involving residues, i.e., the so-called *microswitches*, participating to key contacts defining the active or the inactive states.

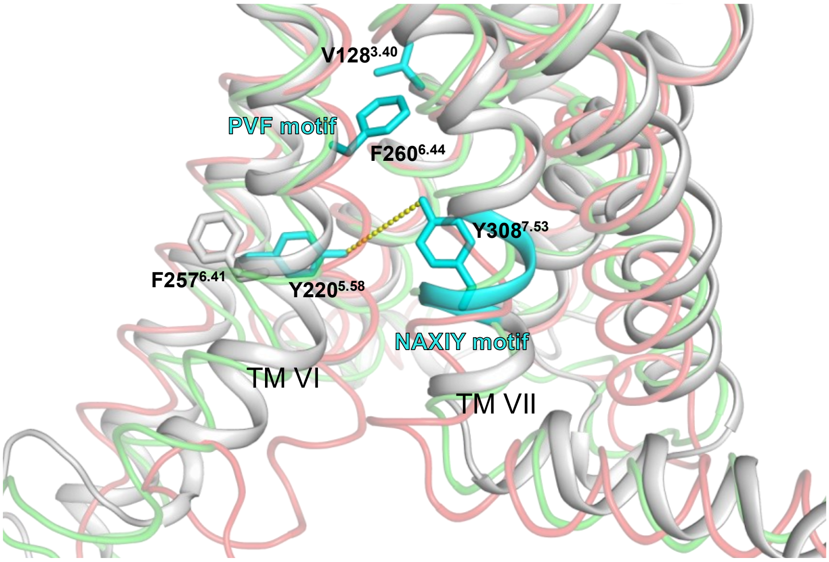

Figure 55. Comparison between the active (green tube, PDB id *7VH0*) [87] and inactive (red tube, PDB id *6ME9*) [75] states and a putative intermediate (grey cartoon) conformation of the MT_2 receptor. The intermediate conformation is retrieved from simulations at intermediate PROG values. TM helix VIIb adopts a conformation similar to the one of the active state, while disrupting the interaction between Y220$^{5.38}$ and Y308$^{7.53}$ present in the active state (distance measure in yellow dashed line). TM helix VIa assumed an intermediate conformation, in which F257$^{6.41}$ could not pack with Y220$^{5.38}$, as happens in the active state.

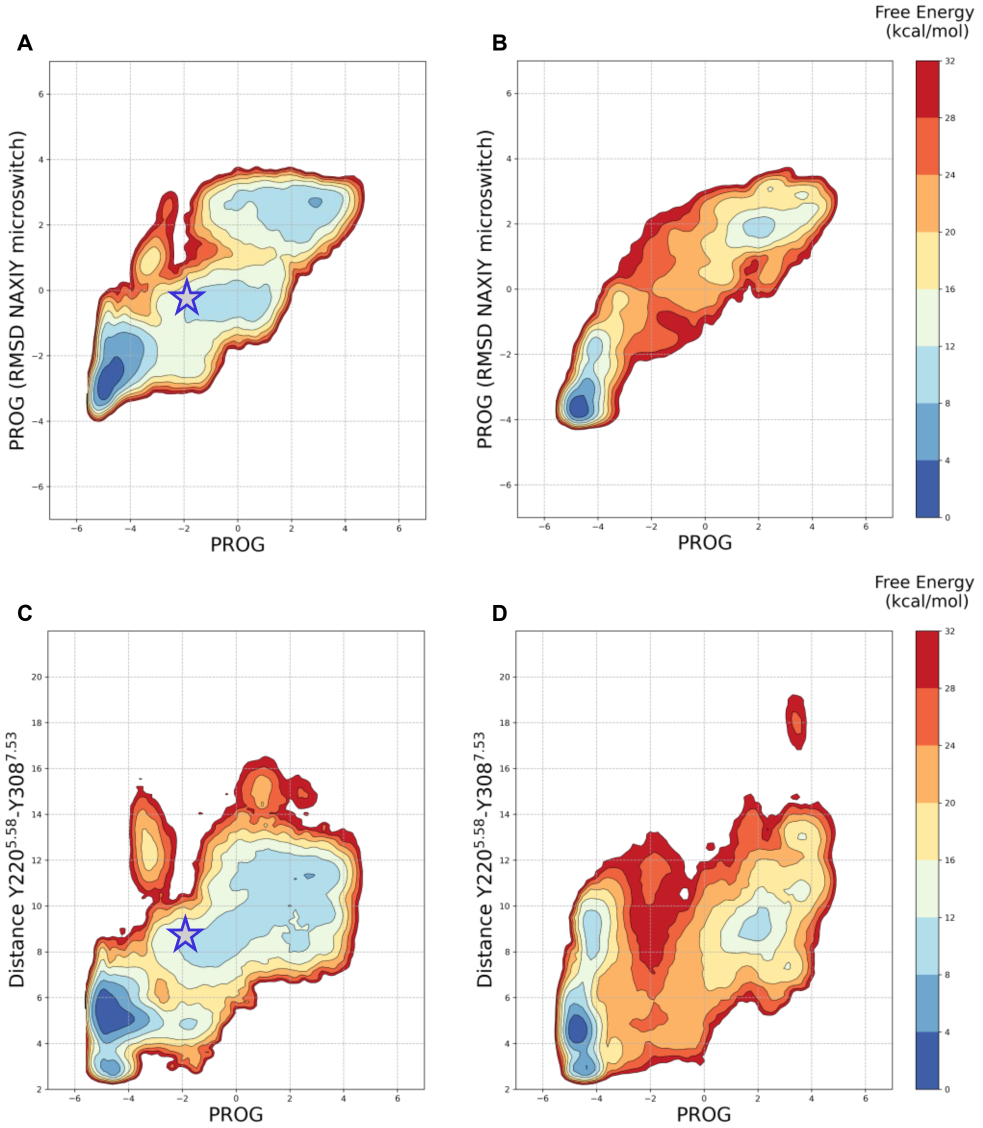

Figure 56. FES of MT$_2$ receptor activation, when bound to IIK7 (**A**) and K185 (**B**). FES are obtained via reweighting of those from the multiple-walker MetaD simulations, projecting onto the RMSD difference of the NAXIY motif at the two functional states. FES is additionally reprojected on the distance of the Y-Y motif (**C-D**). The distance is measured between the hydroxyl oxygens of Y220$^{5.38}$ and Y308$^{7.53}$. The stars individuate a representative conformation for the intermediate state of the agonist-bound binary complex (**A**,**C**), displayed in Figure 55 as the grey conformation.

One example is provided by the YY-motif (i.e., the distance between the hydroxyl oxygens of Y220$^{5.58}$ and Y308$^{7.53}$), monitored in Figure 56.C-D. In the active conformation of the receptor, the two residues would interact at a distance compatible with a water-bridged hydrogen bond interaction, as captured in X-ray structures of other Class A GPCRs. [279,293] The latter interaction would be severed upon receptor inactivation caused by the inward movement of the cytoplasmic portion of the TM helix VI. Therefore, such interaction is diagnostic for a wider conformational change of the intracellular side of the receptor. Additionally, Y308$^{7.53}$ could explore different states (Figure 56.C) previously associated in MetaD simulations to metastable states of the receptor. [294]

A complete transition could not be achieved during simulations starting from the inactive conformation (Figure 55). Indeed, in walkers starting from the free-energy basin of the inactive state, the *N*-terminal portion of TM helix VI could not superimpose to the active conformation as F257$^{6.41}$ could not direct to the internal side of the TM helix as in the cryo-EM structure. This residue might be concurring to the high stability of the active conformation, in which it establishes a π-π interaction with Y308$^{7.53}$, stabilising the Y-Y motif interaction. Mutation of the residue to alanine or valine decreases the receptor basal activity, [87] possibly rationalizing the high basal activity observed for melatonin receptors. [81,82]

Reweighting of the P$^{5.50}$V$^{3.40}$F$^{6.44}$ motif (Figure 57.A-B), known as the "connector region", here defined as the heavy atom of the side chains of V128$^{3.40}$ and F260$^{6.44}$, follows the same behaviour as the previously discussed microswitches, hinting to some ligand-induced conformational change. Movement of these residues, eventually including H208$^{5.46}$, [87] could be prodromic to the conformational transitions at the intracellular side and it could be differently hindered by bulkier ligand substituents close to the CWxP motif.

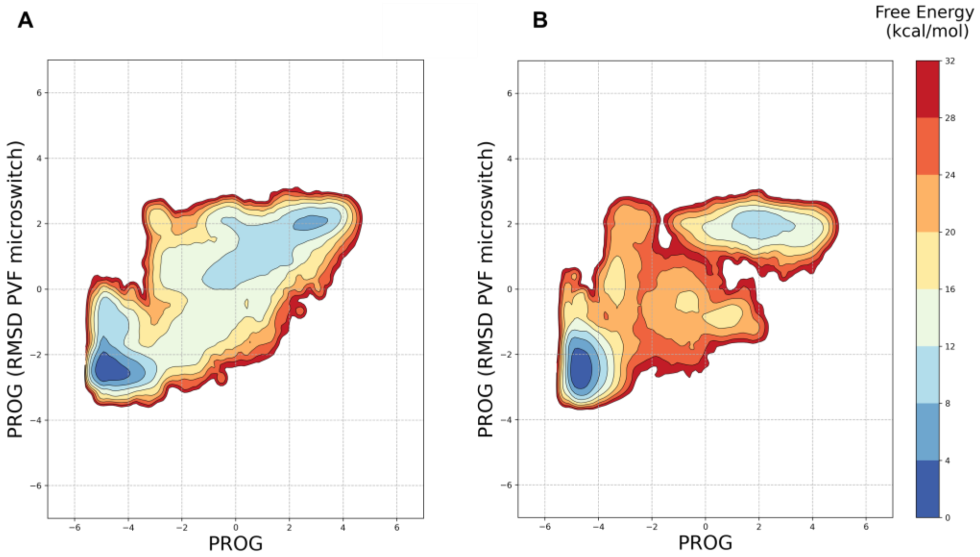

Figure 57. FES of MT$_2$ receptor activation, when bound to IIK7 (**A**) and K185 (**B**). FES are obtained via reweighting of those from the multiple-walker MetaD simulations, projecting onto the RMSD difference of the PVF motif at the two functional states.

To assess the degree of exploration of alternative conformational states of the receptor, reweighting of the FES was performed with a machine learning (ML)-defined descriptor (see Appendix V), called A^{100}. [295] This independent descriptor effectively shows a more direct continuity in the conformational transition for the agonist system.

7.2.3 Shortcomings of the multiple-walker approach

Different limitations could be seen in the application of the multiple-walker MetaD on the defined *CV*s. The hysteresis along the PROG *CV* is mainly due to the lack of exchanges between the two free-energy basins (Figure 58), preventing a quantitative comparison between the active and inactive states and resulting in disconnected free-energy profiles. In fact, walkers starting from each of the two basins could not reach the other one, albeit a certain degree of exploration was permitted at intermediate values (PROG ~ -3 Å). Therefore, simulations were not in diffusive regime and the exploration of different states of the receptor was only guaranteed by starting from structures with PROG values corresponding to both active and inactive states.

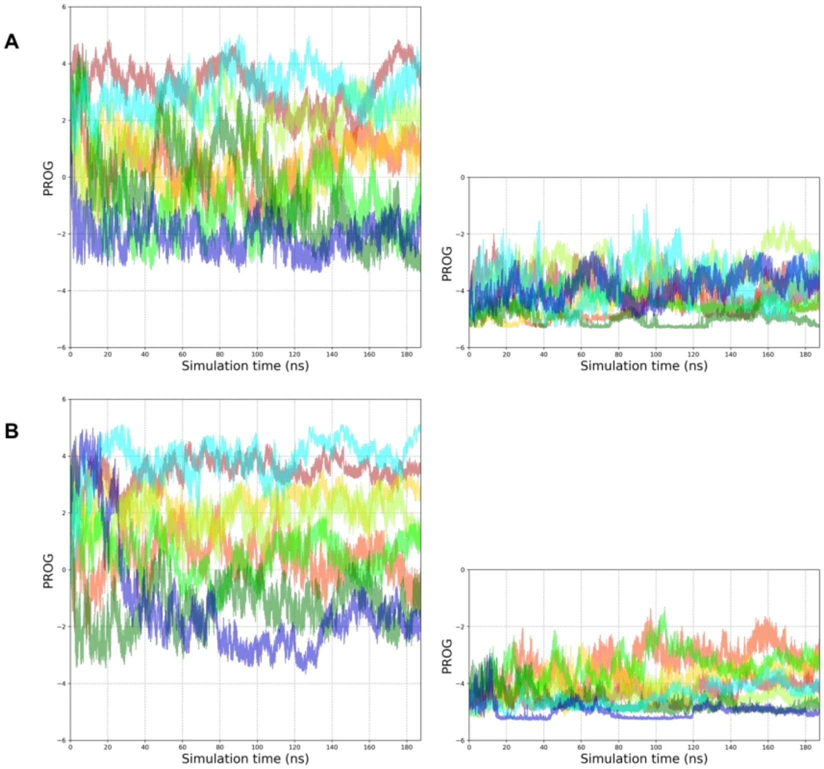

Figure 58. Exploration of the PROG *CV* in multiple-walker MetaD of the complexes of MT_2 receptor bound to IIK7 (**A**) and K185 (**B**). Each colour represents a different walker. Simulations are divided according to their starting free-energy basin (inactive on the left, active on the right).

Apparently, the complexity of the conformational transition related to receptor activation, including multiple specific residue contacts characterizing each state, [290] might discourage the application of linear RMSD combinations for further trials. Application of PCVs [168] might solve this issue, including a better description of microswitches conformational change.

Other limitations are related to the lack of a repulsive potential discouraging the visit of high values of the DIST *CV*, as reported in ref. 289. In these simulations, the exploration was restricted using the distances from the two reference templates, enabling the exploration of conformations of the TM VI in the active state that are far from the reasonable ones, i.e., with an extreme outward bend of the *N*-terminal portion of the helix.

Another limit of the simulations, possibly reducing the stability of the inactive state, regards the sodium ion that never spontaneously binds to $D86^{2.50}$ allosteric pocket during all the simulations. Given its role as negative allosteric modulator, [85] this is an important condition to be taken into account for the receptor conformational equilibria and, even for melatonin receptors, role of sodium chloride as uncoupling agent has been observed, albeit at high concentrations. [81,148] Similarly, the protonation state of the D86$^{2.50}$ might influence the receptor preference for one conformational state. [296]

7.3 CONCLUSIONS AND FUTURE PERSPECTIVES

The present study focuses on the impact of ligand-induced conformational changes in the context of the receptor activation. While preliminary, the design of novel *CV*s here presented might be useful for a variety of purposes. Given the conserved conformational changes across class A GPCRs at the level of microswitches, a protocol successfully applied could be transferred to other receptors. Additionally, finding unique ligand-induced metastable states might be useful to design ligands which are functionally selective at a specific receptor subtype. An example is provided by ligands, such as 5-HEAT (Figure 10), contemporarily being a MT_1 agonist and MT_2 antagonist. [81] While proving ineffective to sample the receptor conformational transition from inactive to active state and vice versa, RMSD-based linear combinations might still be considered for a more limited exploration of the active state to find unique metastable states. [285,287] To this aim, a similar protocol, provided the availability of structure of ternary complexes, could be applied to study the impact of biased ligands, [297] in turn influencing the conformational state of the receptor and the interaction with distinct intracellular signaling partners, without to consider the simulation of the overall activation process.

7.4 COMPUTATIONAL PROTOCOLS

7.4.1 Docking calculations

Docking grid was generated on the prepared structure of the active MT_2 receptor complexed with ramelteon (see Appendix IV), [87] imposing bounding and enclosing boxes of 10 and 20 Å, respectively, centred on the ligand. Docking calculations were performed with Glide 9.0 [298] in standard precision mode, applying the OPLS4 force field [299] and default scaling factors. [191] Parameters controlling the criteria for poses to be kept after rough scoring stage and to be admitted in pose refinement stages were increased by a tenfold. For each run 250 ligand poses were admitted to post-docking minimization. Docking poses of compounds IIK7 and K185 were chosen according to criteria of scaffold superimposition to co-crystalized ligand, geometry of the alkylamide chain and of the formation of the two hydrogen bonds between the amide and methoxy groups and N175$^{4.60}$ and Q194^{ECL2}, respectively. Prior to docking calculations, different K185 structures were generated in GB/SA continuum [247] as input to the docking calculation, including "boat" and "pseudo-boat" conformations of the 6,7-dihydro-5*H*-benzo[3,4]azepino[1,2-*a*]indole heptatomic ring, generated with a mixed torsional/low-mode sampling conformational search [300] implemented in MacroModel. The structures of the ternary complexes were then minimized to an energy gradient of 0.01 $kJ \cdot mol^{-1} \cdot Å^{-1}$ with OPLS4 force field, [299] implemented in MacroModel 13.1, [301] and protein backbone atoms were kept fixed.

7.4.2 System preparation

The protein-ligand complexes were embedded with a POPC:cholesterol 80%-20% membrane of 80 $Å^2$ generated through the Charmm-GUI server. [194] The systems were then solvated with TIP4P-D water molecules. An additional water molecule was added inside the binding site, close to the amide group of the ligands and residues H208$^{5.46}$ and N268$^{6.52}$, through a procedure implemented in Desmond 5.4 [251] and performed with Grand Canonical Monte Carlo sampling in μVT ensemble. [155] Sodium and chloride ions were added to the system with the *genion* tool to a concentration of 0.15 M and, then, until electroneutrality. The systems were parametrized with DES-Amber force field, [302] and TIP4P-D waters with increased London dispersion interactions [303] and parametrized in conjunction. Lipid 17 parameters were assigned to the membrane bilayer, while gaff2 parameters were used for ligands. Partial atomic charges of the ligands were assigned by Jaguar 11.1 [304] with a RESP procedure performed *in vacuo* at the Hartree-Fock level of theory using the 6-31G* basis set. The systems were then minimized with the steepest descent, until the maximum force reached a value inferior to 100.0 $kJ \cdot mol^{-1} \cdot nm^{-1}$, and then POPC membrane was relaxed through 50 ps of MD in the semi-isotropic NPE ensemble. During these two steps, the protein-ligand complexes were kept restrained.

7.4.3 MD and MetaD simulations setup

MD simulations were performed with Gromacs 2021.4 in semi-isotropic NPT ensemble. Temperature coupling was enforced using v-rescale thermostat, [305] separately coupled to the solute and the group of water and ion atoms, and with time constant τ_T=0.1 ps. Pressure was regulated with the c-rescale barostat [306] and time constant τ_P=0.5 ps. Long-range electrostatics were computed with the Particle Mesh Ewald summation [204] with a Fourier scheme adopting fourth order interpolation and 1.6 Å grid spacing, while short-range and Lennard-Jones interactions were computed using a 10 Å cutoff. Bond lengths of hydrogens bound to heavy atoms were restrained to their equilibrium values with the LINCS algorithm, [205] consenting the use of 2 fs timestep.

7.4.4 Adiabatic bias molecular dynamics

ABMD simulations [164] were used to inactivate the MT_2 receptor by enforcing stepwise "ratchet-and-pawl" potentials applied to force *CV*s putatively controlling receptor inactivation in 20 ns-long simulations. Similarly to ref. 286, two different *CV*s were employed to promote such conformational rearrangement:

i) RMSD=0 Å with respect to the α carbons of TM domain of the inactive receptor (PDB id *6ME9*) [75] with a force constant of 1,000 $\text{kcal}\cdot\text{mol}^{-1}\cdot\text{Å}^{-2}$,

ii) χ_1=-0.9 rad (~-50°) of H208$^{5.46}$, i.e., outside of the binding site as in the inactivated thermostabilized receptor, forced with a spring constant of 10 $\text{kcal}\cdot\text{mol}^{-1}\cdot\text{rad}^{-2}$.

The resulting inactive complexes were submitted to 100 ns-long MD simulations to obtain input structures for multiple-walker MetaD simulations.

7.4.5 Multiple-walker metadynamics

wt-MetaD simulations were performed by using sixteen walkers, eight starting from the system in an active conformation and the other eight from the inactive conformation of the complex, which is obtained from the above-described ABMD simulations.

Similarly to ref. 289, two linear combinations of RMSD functions were defined on the basis of thirty-eight α carbon positions belonging to three TM helices (Figure 59), including the upper or extracellular portion of TM helix V (TM Va: Y200$^{5.38}$-L211$^{5.49}$) and the lower or intracellular portions of TM helices VI (TM VIa: S245$^{6.29}$-F264$^{6.44}$) and VII (TM VIIb: C302$^{7.47}$-L311$^{7.56}$). The first *CV* accounts for the progress along the activation,

$$\text{PROG} = RMSD_{active} - RMSD_{inactive} \tag{7.1}$$

while, the second *CV* allows for the exploration of alternative states to the minimum distance path between the two structures,

$$\text{DIST} = RMSD_{active} + RMSD_{inactive} \tag{7.2}$$

The two templates used for the definition of the *CV*s are represented by the energy-minimized complexes of the MT$_2$ receptor bound to ramelteon (i.e., the active complex is PDB id *7VH0* and the inactivated one being PDB id *6ME9*).

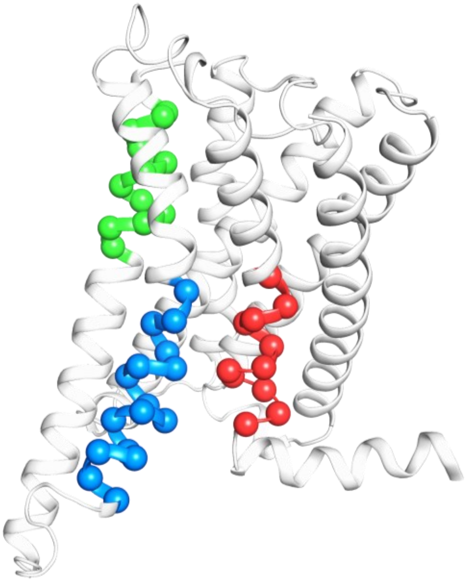

Figure 59. Active reference template of the MT$_2$ receptor (PDB id *7VH0*). RMSD-based *CV*s (PROG and DIST) are defined through the selection of three sections, each belonging to a different TM helix: TM Va (green cartoon and spheres), TM VIa (blue cartoon and spheres) and TM VIIb (red cartoon and spheres).

The eight input structures belonging to each free-energy minimum basin were chosen by extracting from unbiased MD simulations snapshots with the most different values in the PROG-DIST distribution.

MetaD repulsive potential was deposited every 500 integration steps in the form of 2D Gaussian on the surface defined by the two *CV*s, having a radius of 0.15 Å and an initial height of 0.35 kcal·mol^{-1}. The latter is rescaled through using a bias factor γ=16. Simulations are refrained from exploring conformations further than RMSD=10 Å from the two template references.

Analysis of the trajectories and of FES is performed after a cumulative simulation time of 3.0 μs, which consists of 187.5 ns for each walker. Clustering of the trajectories is performed with the *gromos* method, [307] using a cutoff of 0.75 Å. Free-energy reweighting surfaces are performed according to the approach proposed by Tiwary and Parrinello. [178]

Chapter 8. Conclusions

The work presented in the Thesis demonstrates the utility of free-energy calculations for the understanding of receptor-ligand interactions. Such molecular modelling studies require the comprehension of multiple processes regarding not only the energetics of the protein-ligand complex in the proximity of geometries observed in crystal structures, but also other aspects including: *i)* the ligand binding and unbinding process, *ii)* conformational equilibria in solution and inside the target, and *iii)* the conformational landscape of the receptor.

Development of specialized hardware such as graphic processor units has unlocked the microsecond timescale even for routinary calculations and with a relatively low economic and time costs. Due to this technological advance, molecular modelling simulations permit to gather relevant information for the design of novel ligands with optimized properties and for rationalization of their bioactivity.

Several properties of melatonergic ligands have been taken into account in the Thesis, which include the residence time of the ligands, the stereoselectivity, the subtype and the functional selectivity, and the water-solubility, all aspects that can be determinant for the success of a novel ligand. To increase the exploration of the conformational space, free-energy calculations have been employed to increase the sampling of molecular dynamic simulations, which are inherently limited to explore configurations that are energetically close to the experimental structures of the receptor-ligand complex. In some of the examples reported in the Thesis, residues belonging to an outer layer, with respect to the binding site residues directly facing the ligands, seem to influence the binding mechanism and their involvement would not be evaluated or investigated with simpler calculations. Remarkably, equilibrium simulations, such as free-energy perturbation and thermodynamics integration, do not require the *a priori* knowledge necessary for other methods and can be applied to large datasets, even in industrial pipelines, in lieu of simpler static models.

In fact, the design of suitable collective variables is still a demanding task for complex transformations happening at longer timescales than those accessible nowadays in simulations. Machine learning approaches rise could be beneficial in these regards, by integrating a large amount of data in the development of biased sampling protocols. However, the human interface necessary for these studies and theoretical models requiring a long-term effort in their development can still hinder the growth of semi-automatic tools characterizing free-energy differences in biomolecular systems. Moreover, the complexity found in mechanistic studies of a receptor-ligand system can hardly be transferred to other macromolecular targets. Nevertheless, the high similarity among class A GPCR can still leave room for the transferability of some of the considerations and of the protocols drawn in this work to the study of other receptor-ligand complexes.

Chapter 9. Appendices

Appendix I: Protein preparation protocol 1

Crystal structures of MT_1 and MT_2 receptors in complex with 2-phenylmelatonin (PDB id *6ME3*), 2-iodomelatonin (PDB id *6ME4*) [74] and 2-phenylmelatonin (PDB id *6ME6*) [75] were employed for modelling simulations. Molecules belonging to buffers used in the crystallization are removed, as well as the fusion proteins used in the crystallization construct. Residues belonging the N-terminal sequence in the MT_2 receptor were removed, leaving Pro36 as the first residue. ICL3 (including Q219-P227 and R232-L240 in MT_1 and MT_2 receptors) and missing side chains were added with Modeller 9.21. [308,309] One hundred models were generated for each structure, leaving residues adjacent to the loop flexible (i.e., R218 and K228 for the MT_1 receptor, R231 and C241 for the MT_2 receptor), while the rest of the protein was kept frozen during the optimization of the spatial restraints. Finally, the models were ranked according to the molecular probability density function [310] and those with the lowest *molpdf* were further processed. Thermostabilizing mutations in the crystal structures were reverted to the residues of the wildtype with Maestro 11.6. [246] The structures were processed by adding hydrogen atoms and termini were capped with acetyl and methylamino groups with the Protein Preparation Wizard tool of the Maestro Suite. [311] ICL3 residues and the side chains of the missing or modified amino acids were energy-minimized in GB/SA model [247] with OPLS3e force field [193] implemented in MacroModel 12.0 [192], using the Polak-Ribière conjugate gradient method to a convergence threshold of $0.05\ kJ\cdot mol^{-1}\cdot Å^{-1}$.

The orientation of thiol and hydroxyl groups and the conformation of asparagine, glutamine, and histidine residues were adjusted to optimize the hydrogen bond network. Basic and acidic amino acids were modelled in their charged protonation state, while histidine residues were modelled in their neutral state. The tautomeric state of histidine residues was chosen coherently with the optimization of the hydrogen bonding network. In particular, $H195/208^{5.46}$ located on the border of the TM opening, was modelled in its distal tautomeric state. The final structures were energy minimized through a first minimization run allowing relaxation of hydrogen atoms, followed by a second minimization run with heavy atom positions restrained to an RMSD value of 0.3 Å.

Appendix II: Analysis of PCV-US simulations

Different criteria are used to assess the reliability of the PMF resulting from PCV-US simulations and evaluating the unbinding of 2-iodomelatonin from the MT_1 receptor:

i) time series of the PMF profile, as a function of the simulation time for each US window (Figure 60.A).

ii) the overlap of the biased probability distributions in the neighbouring US windows by monitoring the occurrence of the $\mathcal{S}$ value in logarithmic scale (Figure 60.B).

iii) finally, the qualitative agreement of the *a priori* probabilities (eq. 3.17) for the neighbouring US windows is checked by dissecting the global PMF into the free-energy profiles of the individual simulations (Figures 60.C).

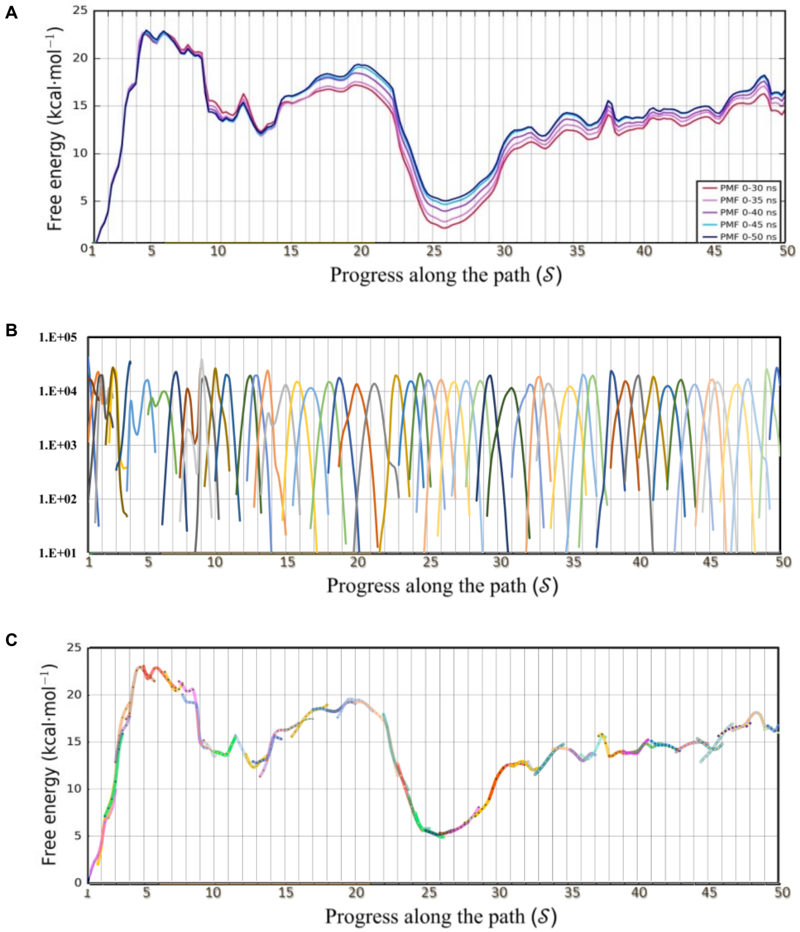

Figure 60. Convergence of PCV-US simulations

Appendix III: Analysis of TI simulations

Data from individual TI simulations reported in Paragraph 6.2.3 is reported. For each subtype receptor, four TI simulations are performed, each consisting of twelve windows with a different λ value. For each simulation, <∂V/∂λ> and ΔG profiles are shown.

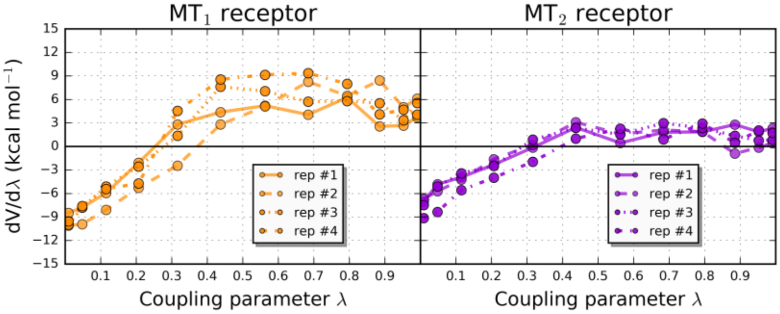

Figure 61. Analysis of <∂V/∂λ> values for each simulation and for each TI window with respect to the coupling parameter λ value.

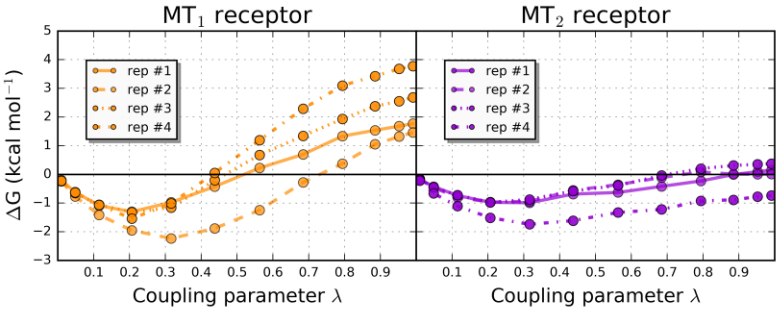

Figure 62. Analysis of ΔG values for each simulation and for each TI window with respect to the coupling parameter λ value.

Appendix IV: Protein preparation protocol 2

Preparation of the cryo-electron microscopy structure of the ternary complex of MT_2 receptor bound to ramelteon

Crystal structure of the ternary complex of the MT_2 receptor bound with ramelteon and in complex with the inhibitory G-protein (PDB access code *7VH0*) [87] was prepared for simulations, after the antibody fragment scFv16 (chain E) was removed. Hydrogens and bond orders were added with the Protein Preparation Wizard. [311] The disulphide bridge between $C113^{3.25}$ and $C190^{ECL2}$ was rebuilt. Missing side chains and mutated residues were restored by Prime 6.3. [312] Missing portions of the receptor were built by using a chimeric model template (Figure 63.A) designed with Prime 6.3 through the knowledge-based method, which relies on backbone coordinates (and side chains of conserved residues) from different structures. Residues at the beginning of the TM helix I and at the end of helix VIII (pink residues in Figure 63.A) were modelled on the thermostabilized construct of the MT_2 receptor in complex with ramelteon (PDB access code *6ME9*, chain B). [74] A partially unfolded intracytoplasmic portion of the TM helix VI (blue residues in Figure 63.A) was rebuilt using the cryo-electron microscopy structure of the MT_1 receptor in complex with ramelteon (PDB access code *7VGZ*, chain B). [87] ICL3 missing residues are rebuilt by using a template recovered through a BLAST-NBCI server search run. Non-conserved residues of the framework and the missing residues (including the ICL3 residues) are subjected to a rotamer search to remove clashes and then minimized with the OPLS-2005 force field in vacuum. [313] Lastly, a side-chain prediction and minimization run with OPLS4 force field in the implicit solvent model VSGB2.1 are performed on these residues to further refine the model. The goodness of the model was checked by monitoring the Ramachandran plot (Figure 63.B), in which only two residues are reported in not consented regions, with one of them being a glycine residue.

After model building, the orientation of thiol and hydroxyl groups and of asparagine and glutamine side chains were then adjusted to optimize the hydrogen bonding network and, as well, the tautomeric state of the histidine residues was chosen coherently with this aim. Notably, coherently with the previous simulations, $H208^{5.46}$ was modelled with its distal and neutral tautomeric state. Basic and acid amino acids were modelled in their charged protonation states, while histidine residues were prepared in their neutral state. However, D54$^{1.46}$ was modelled in its protonated state to increase the stability of the interface between TM helices I and II. Protein termini were protected with capping neutral groups and all hydrogens atoms were minimized with OPLS4 force field by using Impact 9.0. [314] A final energy-minimization of the entire ternary complex was conducted with Macromodel 13.1 [301] with OPLS4 force field using the Polak-Ribière conjugate gradient method to a convergence threshold of 0.01 kJ·mol^{-1}·Å^{-1}, while the backbone atoms were kept fixed.

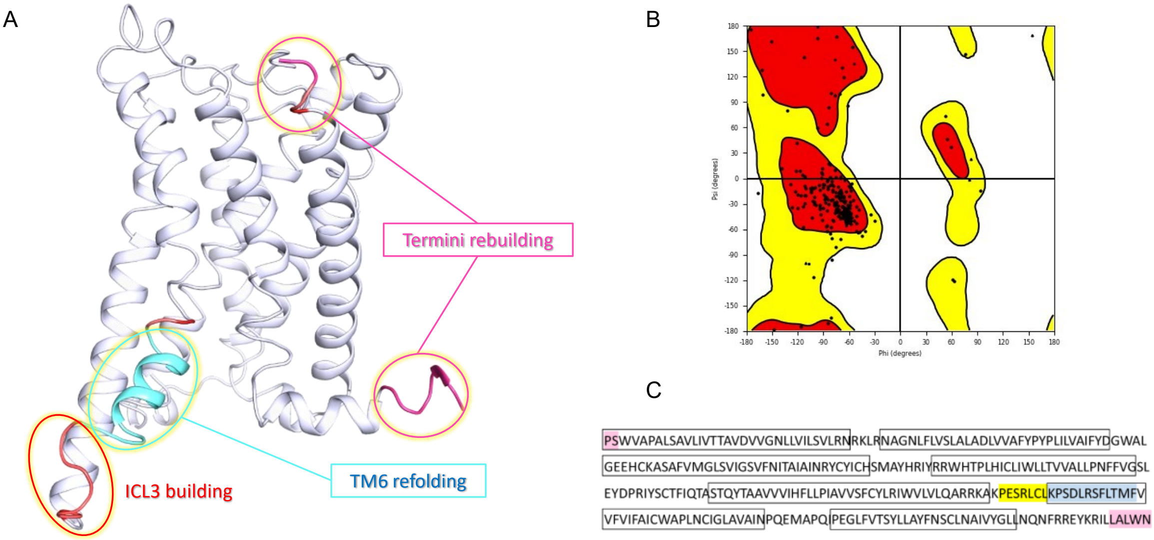

Figure 63. Representation of the chimeric homology model used to refine the cryo-EM structure of the MT$_2$ receptor bound with ramelteon (**A**). Ramachandran plot (**B**) and origin template of the sequence (**C**) are also shown. The pink sequence stands for the region for which the inactive MT$_2$ bound to ramelteon inactive complex (PDB id *6ME9*) [75] has been used. The yellow sequence is the reconstructed ICL3 and the blue region is the *N*-terminal region of the TM helix VI for which the MT$_1$ bound to ramelteon in its active complex (PDB id *7VGZ*) [87] has been used.

Appendix V: Free-energy surface of the MT_2 activation projected on the ML-defined descriptor A^{100}

Reweighting of the free-energy landscape due to MT_2 activation was reprojected onto the machine learning (ML)-defined *CV*, called A^{100}, which is a combination of five inter-helix distances (Figure 64) used as a classifier for the identification of the functional state of GPCRs belonging to class A. The activity model was trained on X-ray crystal structures and multimicrosecond MD trajectories and recognizes important distances, similarly to what has been proposed by Manglik and Krause [280]. Applying the model described for the β_2 adrenergic receptor to the MT_2 receptor, the A^{100} descriptor is defined as follows:

$$\begin{aligned} A^{100} = {} & -14.43 \cdot r(V61^{1.53} - L310^{7.55}) - 7.62 \cdot r(D86^{2.50} - I225^{3.37}) \\ & +9.11 \cdot r(N130^{3.42} - T157^{4.42}) - 6.32 \cdot r(L228^{5.66} - F250^{6.34}) \\ & -5.22 \cdot r(V274^{6.58} - F290^{7.35}) + 287.88 \end{aligned} \tag{9.1}$$

According to the three-state model, [295] $A^{100} > 55$ defines active-like conformations, while $A^{100} < 0$ defines inactive ones and values $0 < A^{100} < 55$ define intermediate states.

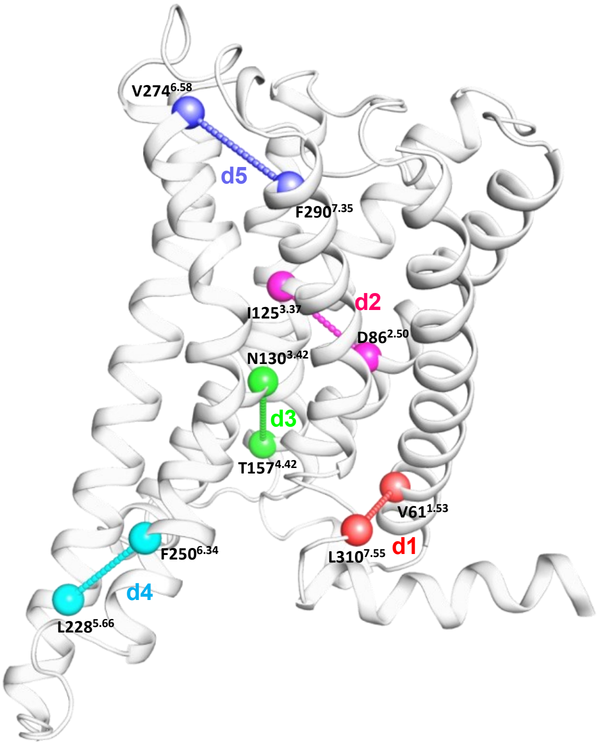

Figure 64. Five inter-helix distances used to define A^{100}, represented as the distances between the α carbons in the active template of the MT_2 receptor

The equation was applied to the multiple-walker *wt*-MetaD simulations and revealed a better sampling of intermediate-classified conformations for the complex of the receptor bound to the agonist (Figure 65.A), while the system bound to K185 explored more negative A^{100} values (Figure 65.B). While offering diagnostics to check the exploration of alternative conformations of the TM bundle, however the classifier does not permit an evaluation of the conformational change at the level of the microswitches.

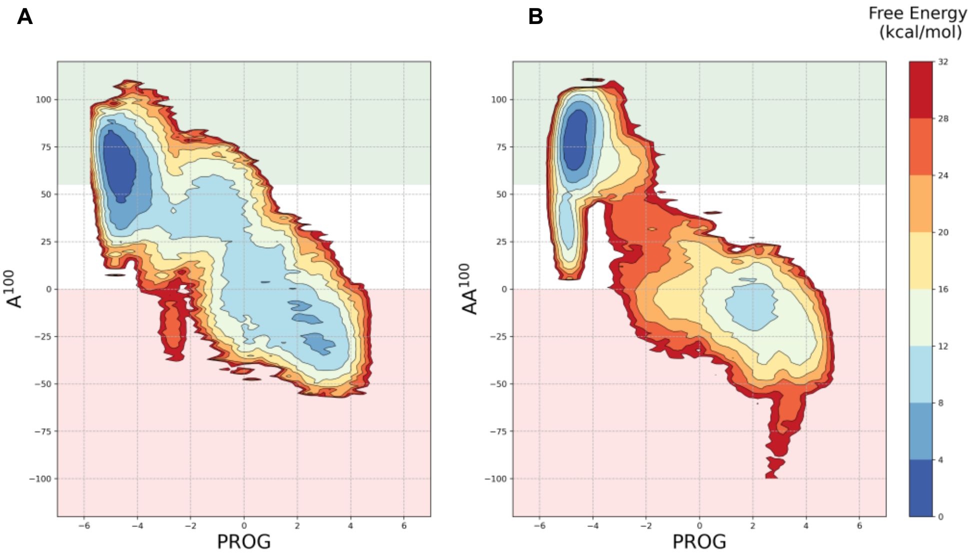

Figure 65. Free-energy surfaces of MT_2 activation landscapes bound to IIK7 (**A**) and K185 (**B**) obtained via reweighting of those from the multiple-walker MetaD simulations, projecting onto a ML-derived *CV*, named A^{100}. Green, white and red areas define the active, intermediate and inactive conformations according to the three-states-model definition of the *CV*, reported in ref. 295.

References

---

1 Elisi, G. M.; Scalvini, L.; Lodola, A.; Mor, M; Rivara, S. Free-energy simulations support a lipophilic binding route for melatonin receptors. *J. Chem. Inf. Model.* **2022**, 62, 210-22.

2 Elisi, G. M.; Bedini, A.; Scalvini, L.; Carmi, C.; Bartolucci, S.; Lucini, V.; Scaglione, F.; Mor, M.; Spadoni, G. Chiral recognition of flexible melatonin receptor ligands induced by conformational equilibria. *Molecules.* **2020**, 25, 4057.

3 Mari, M.; Elisi, G. M.; Bedini, A.; Lucarini, S.; Retini, M.; Lucini, V.; Scaglione, F.; Vincenzi, F.; Varani, K.; Castelli, R.; Mor, M-; Rivara, S.; Spadoni, G. 2-Arylmelatonin analogues: Probing the 2-phenyl binding pocket of melatonin MT_1 and MT_2 receptors. *Eur. J. Med. Chem.* **2022**, 243, 114762.

4 Ferlenghi, F.; Mari, M.; Gobbi, G.; Elisi, G. M.; Mor, M.; Rivara, S.; Vacondio, F.; Bartolucci, S; Bedini, A.; Fanini, F.; Spadoni, G. *N*-(Anilinoethyl)amide melatonergic ligands with improved water solubility and metabolic stability. *ChemMedChem*. **2021**, 16, 3071-82.

5 Elisi, G. M.; Scalvini, L.; Lodola, A.; Bedini, A.; Spadoni, G:; Rivara, S. In silico drug discovery of melatonin receptor ligands with therapeutic potential. *Expert Opin. Drug Discov.* **2022**, 17, 343-54.

6 Hardeland, R.; Cardinali, D. P.; Srinivasan, V.; Spence, D. W.; Brown, G. M.; Pandi-Perumal, S. R. Melatonin–a pleiotropic, orchestrating regulator molecule. *Prog. Neurobiol.* **2011**, 93, 350-84.

7 Reiter, R. J. Pineal melatonin: cell biology of its synthesis and of its physiological interactions. *Endocr Rev.* **1991**, 12, 151-80.

8 Costa, E. J. X.; Lopes, R. H.; Lamy-Freund, M. T. Permeability of pure lipid bilayers to melatonin. *J. Pineal Res.* **1995**, 19, 123-6

9 Yu, H.; Dickson, E. J.; Jung, S. R.; Koh, D.; Hille, B. High membrane permeability for melatonin. *J. Gen. Physiol.* **2016**, 147, 63-76.

10 Tosini, G.; Menaker, M. The clock in the mouse retina: melatonin synthesis and photoreceptor degeneration. *Brain Res.* **1998**, 789, 221-8.

11 Zhao, D.; Yu, Y.; Shen, Y.; Liu, Q.; Zhao, Z.; Sharma, R.; Reiter, R. J. Melatonin synthesis and function: evolutionary history in animals and plants. *Front. Endocrinol, (Lausanne).* **2019**, 17, 249.

12 McCord, C. P.; Allen, F. P. Evidence associating pineal gland function with alterations in pigmentation. *J. Exp. Zool.* **1917**, 23, 207-24.

13 Lerner, A. B.; Case, J. D.; Takahashi, Y.; Lee, T. H.; Mori, W. Isolation of melatonin, the pineal gland factor that lightens melanocytes. *J. Am. Chem. Soc.* **1958**, 80, 2587.

14 Lerner, A. B.; Case, J. D. Structure of melatonin. *J. Am. Chem. Soc.* **1959**, 81, 6084.

15 Ralph, C. L.; Mull, D.; Lynch, H. L.; Hedlund, L. A melatonin rhythm persists in rat pineals in darkness. *Endocrinology.* **1971**, 89, 1361-6.

16 Lynch, H. J.; Wurtman, R. J.; Moskowitz, M. A.; Archer, M. C.; Ho, M. H. Daily rhythm in human urinary melatonin. *Science.* **1975**, 187, 169-71.

17 Dubocovich, M. L.; Delagrange, P.; Krause, D. N.; Sugden, D.; Cardinali, D. P.; Olcese, J. International Union of Basic and Clinical Pharmacology. LXXV. Nomenclature, classification, and pharmacology of G protein-coupled melatonin receptors. *Pharmacol. Rev.* **2010**, 62, 343-80.

18 Simonneaux, V.; Ribelayga, C. Generation of the melatonin endocrine message in mammals: a review of the complex regulation of melatonin synthesis by norepinephrine, peptides, and other pineal transmitters. *Pharmacol. Rev.* **2003**, 55, 325-95.

---

19 Klein, D. C.; Weller, J. L. Indole metabolism in the pineal gland: a circadian rhythm in N-acetyltransferase. *Science.* **1970**, 169, 1093-5.

20 Hirata, F.; Hayaishi, O.; Tokuyama, T.; Seno, S. In vitro and in vivo formation of two new metabolites of melatonin. *J. Biol. Chem.* **1974**, 249, 1311-3.

21 Hardeland, R.; Poeggeler, B. Melatonin and synthetic melatonergic agonists: actions and metabolism in the central nervous system. *Cent. Nerv. Syst. Agents Med. Chem.* **2012**, 12, 189-216.

22 Jockers, R.; Delagrange, P.; Dubocovich, M. L.; Markus, R. P.; Renault, N.; Tosini, G.; Cecon, E.; Zlotos, D. P. Update on melatonin receptors: IUPHAR Review 20. *Br. J. Pharmacol.* **2016**, 173, 2702-25.

23 Liu, J.; Clough, S. J.; Hutchinson, A. J.; Adamah-Biassi, E. B.; Popovska-Gorevski, M.; Dubocovich, M. L. MT$_1$ and MT$_2$ Melatonin Receptors: A Therapeutic Perspective. *Annu Rev Pharmacol Toxicol.* **2016**, 56, 361-83.

24 Slominski, R. M.; Reiter, R. J.; Schlabritz-Loutsevitch, N.; Ostrom, R. S.; Slominski, A. T. Melatonin membrane receptors in peripheral tissues: distribution and functions. *Mol. Cell. Endocrinol.* **2012**, 351, 152-66.

25 Galano, A.; Medina, M. E.; Tan, D.-X.; Reiter, R. J. Melatonin and its metabolites as copper chelating agents and their role in inhibiting oxidative stress: a physicochemical analysis. *J. Pineal Res.* **2015**, 58, 107-16.

26 Tan, D.-X.; Manchester, L. C.; Reiter, R. J.; Plummer, B. F.; Hardies, L. J.; Weintraub, S. T.; Vijayalaxmi; Shepherd, A. M. A novel melatonin metabolite, cyclic 3-hydroxymelatonin: a biomarker of in vivo hydroxyl radical generation. *Biochem. Biophys. Res. Commun.* **1998**, 253, 614-20.

27 Reiter, R. J.; Tan, D.-X; Rosales-Corral, S.; Manchester, L. C. The universal nature, unequal distribution and antioxidant functions of melatonin and its derivatives. *Mini Rev. Med. Chem.* **2013**, 13, 373-84.

28 Liu, L.; Labani, N.; Cecon, E.; Jockers, R. Melatonin target proteins: Too many or not enough? *Front. Endocrinol. (Lausanne).* **2019**, 10, 791.

29 Nosjean, O.; Ferro, M.; Coge, F.; Beauverger, P.; Henlin, J. M.; Lefoulon, F.; Fauchere, J. L.; Delagrange, P.; Canet, E.; Boutin, J. A. Identification of the melatonin-binding site MT$_3$ as the quinone reductase 2. *J. Biol. Chem.* **2000**, 275, 31311-7.

30 Calamini, B.; Santarsiero, B. D.; Boutin, J. A.; Mesecar, A. D. Kinetic, thermodynamic and X-ray structural insights into the interaction of melatonin and analogues with quinone reductase 2. *Biochem. J.* **2008**, 413, 81-91.

31 Cecon, E., Oishi, A.; Jockers, R. Melatonin receptors: molecular pharmacology and signalling in the context of system bias. *Br. J. Pharmacol.* **2018**, 175, 3263-80.

32 Levoye, A.; Dam, J.; Ayoub, M. A.; Guillaume, J. L.; Couturier, C.; Delagrange, P.; Jockers, R. The orphan GPR$_{50}$ receptor specifically inhibits MT1 melatonin receptor function through heterodimerization. *EMBO J.* **2006**, 25, 3012-23.

33 Suofu, Y.; Li, W.; Jean-Alphonse, F. G.; Jia, J.; Khattar, N. K.; Li, J.; Baranov, S. V.; Leronni, D.; Mihalik, A. C.; He, Y.; Cecon, E.; Wehbi, V. L.; Kim, J.; Heath, B. E.; Baranova, O. V.; Wang, X.; Gable, M. J.; Kretz, E. S.; Di Benedetto, G.; Lezon, T. R.; Ferrando, L. M.; Larkin, T. M.; Sullivan, M.; Yablonska, S.; Wang, J.; Minnigh, M. B.; Guillaumet, G.; Suzenet, F.; Richardson, R. M.; Poloyac, S. M.; Stolz, D. B.; Jockers, R.; Witt-Enderby, P. A.; Carlisle, D. L.; Vilardaga, J. P.; Friedlander, R. M. Dual role of mitochondria in producing melatonin and driving GPCR signaling to block cytochrome c release. *Proc. Natl. Acad. Sci. U. S. A.* **2017**, 114, 7997-8006

34 Foord, S.M.; Bonner, T.I.; Neubig, R.R.; Rosser, E.M.; Pin, J.-P.; Davenport, A.P.; Spedding, M.; Harmar, A.J. International Union of Pharmacology. XLVI. G protein-coupled receptor list. *Pharmacol. Rev.* **2005**, 57, 279-88.

35 Fredriksson, R.; Lagerström, M.C.; Lundin, L.-G.; Schiöth, H.B. The G-protein-coupled receptors in the human genome form five main families. Phylogenetic analysis, paralogon groups, and fingerprints. *Mol. Pharmacol.* **2003**, 63, 1256-72.

36 Oishi, A.; Cecon, E.; Jockers, R. Chapter Two - Melatonin receptor signaling: Impact of receptor oligomerization on receptor function. *Int. Rev. Cell Mol. Biol.* **2018**, 338, 59-77.

---

37 Ebisawa, T.; Karne, S.; Lerner, M. R.; Reppert, S. M. Expression cloning of a high affinity melatonin receptor from Xenopus dermal melanophores. *Proc. Natl. Acad. Sci. USA.* **1994**, 91, 6133-7.

38 Reppert, S.M., Weaver, D.R., Ebisawa, T. Cloning and characterization of a mammalian melatonin receptor that mediates reproductive and circadian responses. *Neuron*. **1994**, 13, 1177-85.

39 Reppert, S. M.; Godson, C.; Mahle, C. D.; Weaver, D. R.; Slaugenhaupt, S. A.; Gusella, J. F. Molecular characterization of a second melatonin receptor expressed in human retina and brain: the Mel1b melatonin receptor. *Proc Natl Acad Sci USA.* **1995**, 92, 8734-8.

40 Reppert, S. M.; Weaver, D. R.; Godson, C. Melatonin receptors step into the light: cloning and classification of subtypes. *Trends Pharmacol. Sci.* **1996**, 17, 100-2.

41 Garratt, P. J.; Sally, R. J.; Rowe, J.; Sugden, D. Mapping the melatonin receptor. 1. the 5-methoxyl group of melatonin is not an essential requirement for biological activity. *Bioorg. Med. Chem. Lett.* **1994**, 4, 1555-8.

42 Liu, C.; Weaver, D. R.; Jin, X.; Shearman, L.P.; Pieschl, R. L.; Gribkoff, V. K.; Reppert, S. M. Molecular dissection of two distinct actions of melatonin on the suprachiasmatic circadian clock. *Neuron.* **1997** 19, 91-102.

43 Jin, X.; Von Gall, C.; Pieschl, R. L.; Gribkoff, V. K.; Stehle, J. H.; Reppert, S. M.; Weaver, D. R. Targeted disruption of the mouse Mel(1b) melatonin receptor. *Mol. Cell. Biol.* **2003**, 23, 1054-60.

44 Zlotos, D. P.; Jockers, R.; Cecon, E., Rivara, S., Witt-Enderby, P. A. MT$_1$ and MT$_2$ melatonin receptors: ligands, models, oligomers, and therapeutic potential. *J. Med. Chem.* **2014**, 57, 3161-85.

45 Tosini, G.; Owino, S.; Guillaume, J-L.; Jockers, R. Understanding melatonin receptor pharmacology: latest insights from mouse models, and their relevance to human disease. *Bioessays*. **2014**, 36, 778-87.

46 Legros, C.; Dupré, C.; Brasseur, C.; Bonnaud, A.; Bruno, O.; Valour, D.; Shabajee, P.; Giganti, A.; Nosjean, O.; Kenakin, K. P.; Boutin, J. A. Characterization of the various functional pathways elicited by synthetic agonists or antagonists at the melatonin MT$_1$ and MT$_2$ receptors. *Pharmacol. Res. Perspect.* **2019**, 8, e00539.

47 Ruan, W.; Yuan, X.; Eltzschig, H. K. Circadian rhythm as a therapeutic target. *Nat. Rev. Drug. Discov.* **2021**, 20, 287-307.

48 Comai, S.; Gobbi, G. Sleep well. Untangling the role of melatonin MT$_1$ and MT$_2$ receptors in sleep. *J. Pineal Res.* **2019**, 66, e12544.

49 Pandi-Perumal, S. R.; Trakht, I.; Srinivasan, V.; Spence, D. W.; Maestroni, G. J. M.; Zisapel, N.; Cardinali, D. P. Physiological effects of melatonin: role of melatonin receptors and signal transduction pathways. *Prog. Neurobiol.* **2008**, 85, 335-53.

50 Wu, Y.-H.; Zhou, J.-H.; Van Heerikhuize, J.; Jockers, R.; Swaab, D. F. Decreased MT$_1$ melatonin receptor expression in the suprachiasmatic nucleus in aging and Alzheimer's disease. *Neurobiol. Aging.* **2007**, 28, 1239-47.

51 Sinha, B.; Wu, Q.; Li, W.; Tu, Y.; Sirianni, A. C.; Chen, Y.; Jiang, J.; Zhang, X.; Chen, W.; Zhou, S.; Reiter, R. J.; Manning, S. M.; Patel, N. J.; Aziz-Sultan, A. M.; Inder, T. E.; Friedlander, R. M.; Fu, J.; Wang, X. Protection of melatonin in experimental models of newborn hypoxic-ischemic brain injury through MT$_1$ receptor. *J. Pineal Res.* **2018**, 64, e12443.

52 Wang, X.; Sirianni, A; Pei, X.; Cormier, K; Smith, K; Jiang, J.; Zhou, S.; Wang, H.; Zhao, R.; Yano, H.; Kim, J. E.; Li, W.; Kristal, B. S.; Ferrante, J. R.; Friedlander, R. M. The melatonin MT$_1$ receptor axis modulates mutant Huntington-mediated toxicity. *J. Neurosci.* **2011**, 31, 14496-507.

53 Barberino, R. S.; Menezes, V. G.; Ribeiro, A. E. A. S.; Palheta, R. C. Jr.; Jiang, X.; Smitz, J. E. J.; Matos, M. H. T. Melatonin protects against cisplatin-induced ovarian damage in mice via the MT$_1$ receptor and antioxidant activity. *Biol. Reprod.* **2017**, 96, 1244-55.

---

54 Kaneko, Y.; Hayashi, T.; Yu, S. J.; Tajiri, N.; Bae, E. C.; Solomita, M. A.; Chheda, S. H.; Weinbren, N. L.; Parolini, O.; Borlongan, C. V. Human amniotic epithelial cells express melatonin receptor MT$_1$, but not melatonin receptor MT$_2$: a new perspective to neuroprotection. *J. Pineal Res.* **2011**, 50, 272-80.

55 Radio, N. M.; Doctor, J. S.; Witt-Enderby, P. A. Melatonin enhances alkaline phosphatase activity in differentiating human adult mesenchymal stem cells grown in osteogenic medium via MT$_2$ melatonin receptors and the MEK/ERK (1/2) signaling cascade. *J. Pineal Res.* **2006**, 40, 332-42.

56 Sharan, K.; Lewis, K.; Furukawa, T.; Yadav, V. K. Regulation of bone mass through pineal-derived melatonin-MT$_2$ receptor pathway. *J. Pineal Res.* **2017**, 63, e12423.

57 Posa, L.; Lopez-Canul, M.; Rullo, L.; De Gregorio, D.; Dominguez-Lopez, S.; Kaba Aboud, M.; Caputi, F. F.; Candeletti, S.; Romualdi, P.; Gobbi, G. Nociceptive responses in melatonin MT$_2$ receptor knockout mice compared to MT$_1$ and double MT$_1$/MT$_2$ receptor knockout mice. *J. Pineal Res.* **2020**, 69, e12671.

58 Lopez-Canul, M.; Palazzo, E.; Dominguez-Lopez, S.; Luongo, L.; Lacoste, B.; Comai, S.; Angeloni, D.; Fraschini, F.; Boccella, S.; Spadoni, G.; Bedini, A.; Tarzia, G.; Maione, S.; Granados-Soto, V.; Gobbi, G. Selective melatonin MT$_2$ receptor ligands relieve neuropathic pain through modulation of brainstem descending antinociceptive pathways. *Pain.* **2015**, 156, 305-17.

59 Posa, L.; De Gregorio, D.; Gobbi, G.; Comai, S. Targeting melatonin MT$_2$ receptors: a novel pharmacological avenue for inflammatory and neuropathic pain. *Curr. Med. Chem.* **2018**, 25, 3866-82.

60 Posa, L.; De Gregorio, D.; Lopez-Canul, M.; He, Q.; Darcq, E.; Rullo, L.; Pearl-Dowler, L.; Luongo, L.; Candeletti, S.; Romualdi, P.; Kieffer, B. L.; Gobbi, G. Supraspinal melatonin MT$_2$ receptor agonism alleviates pain via a neural circuit that recruits mu opioid receptors. *J. Pineal Res.* **2022**, 73, e12825.

61 Ochoa-Sanchez, R.; Comai, S.; Lacoste, B.; Bambico, F. R.; Dominguez-Lopez, S.; Spadoni, G.; Rivara, S.; Bedini, A.; Angeloni, D.; Fraschini, F.; Mor, M.; Tarzia, G.; Descarries, L.; Gobbi, G. Promotion of Non-Rapid Eye Movement sleep and activation of reticular thalamic neurons by a novel MT$_2$ melatonin receptor ligand. *J. Neurosci.* **2011**, 31, 18439-52.

62 Ochoa-Sanchez, R.; Rainer, Q.; Comai, S.; Spadoni, G.; Bedini, A.; Rivara, S.; Fraschini, F.; Mor, M.; Tarzia, G.; Gobbi, G. Anxiolytic effects of the melatonin MT$_2$ receptor partial agonist UCM765: Comparison with melatonin and diazepam. *Prog. Neuropsychopharmacol. Biol. Psychiatry.* **2012**, 39, 318-25.

63 Bonnefond, A.; Clément, N.; Fawcett, K.; Yengo, L.; Vaillant, E.; Guillaume, J.-L.; Dechaume, A.; Payne, F.; Roussel, R.; Czernichow, S.; Hercberg, S.; Hadjadj, S.; Balkau, B.; Marre, M.; Lantieri, O.; Langenberg, C.; Bouatia-Naji, N.; Meta-Analysis of Glucose and Insulin-Related Traits Consortium (MAGIC); Charpentier, G.; Vaxillaire, M.; Rocheleau, G.; Wareham, N. J.; Sladek, R.; McCarthy, M. I.; Dina, C.; Barroso, I.; Jockers, R.; Froguel, P. Rare MTNR1B variants impairing melatonin receptor 1B function ontribute to type 2 diabetes. *Nat. Genet.* **2012**, 44, 297-301.

64 Karamitri, A.; Plouffe, B.; Bonnefond, A.; Chen, M.; Gallion, J.; Guillaume, J. L.; Hegron, A.; Boissel, M.; Canouil, M.; Langenberg, C., Wareham, N. J.; Le Gouill, C.; Lukasheva, V.; Lichtarge, O.; Froguel, P.; Bouvier, M.; Jockers, R. Type 2 diabetes-associated variants of the MT$_2$ melatonin receptor affect distinct modes of signaling. *Sci. Signal.* **2018**, 11, eaan6622.

65 Karamitri, A.; Jockers, R. Melatonin in type 2 diabetes mellitus and obesity. *Nat. Rev. Endocrinol.* **2019**, 15, 105-25.

66 Contreras-Alcantara, S.; Baba, K.; Tosini, G. Removal of melatonin receptor type 1 induces insulin resistance in the mouse. *Obesity (Silver Spring).* **2010**, 18, 1861-3.

67 Kinker, G. S.; Ostrowski, L. H.; Ribeiro, P. A. C.; Chanoch, R.; Muxel, S. M.; Tirosh, I.; Spadoni, G.; Rivara, S.; Martins, V. R.; Santos, T. G.; Markus, R. P.; Fernandes, P. A. C. M. MT$_1$ and MT$_2$ melatonin receptors play opposite roles in brain cancer progression. *J. Mol. Med. (Berl).* **2021**, 99, 289-301.

---

68 Girouard, H.; Chulak, C.; Lejossec, M.; Lamontagne, D.; de Champlain, J. Vasorelaxant effects of the chronic treatment with melatonin on mesenteric artery and aorta of spontaneously hypertensive rats. *J Hypertens.* **2001**, 19, 1369-77.

69 Krause, D. N.; Barrios, V. E.; Duckles, S. P. Melatonin receptors mediate potentiation of contractile responses to adrenergic nerve stimulation in rat caudal artery. *Eur. J. Pharmacol.* **1995**, 276, 207-13.

70 Ting, K. N.; Dunn, W. R.; Davies, D. J.; Sugden, D.; Delagrange, P.; Guardiola-Lemaître, B.; Scalbert, E.; Wilson, V. G. Studies on the vasoconstrictor action of melatonin and putative melatonin receptor ligands in the tail artery of juvenile Wistar rats. *Br. J. Pharmacol.* **1997**. 122, 1299-306.

71 López-Canul, M.; Min, S. H.; Posa, L.; De Gregorio, D.; Bedini, A.; Spadoni, G.; Gobbi, G.; Comai, S. Melatonin MT_1 and MT_2 receptors exhibit distinct effects in the modulation of body temperature across the light/dark cycle. *Int. J. Mol. Sci.* **2019**, 20, 2452.

72 Pala, D.; Lodola, A.; Bedini, A., Spadoni, G.; Rivara, S. Homology models of melatonin receptors: challenges and recent advances. *Int. J. Mol. Sci.* **2013**, 14, 8093-121.

73 Heydenreich, F. M.; Vuckovic, Z.; Matkovic, M.; Veprintsev, D. B. Stabilization of G protein-coupled receptors by point mutations. *Front. Pharmacol.* **2015**, 6, 82.

74 Stauch, B.; Johansson, L. C.; McCorvy, J. D.; Patel, N.; Han, G. W.; Huang, X.; Gati, C.; Batyuk, A.; Slocum, S. T.; Ishchenko, A.; Brehm, W.; White, T. A.; Michaelian, N.; Madsen, C.; Zhu, L.; Grant, T. D.; Grandner, J. M.; Shiriaeva, A.; Olsen, R. H. J.; Tribo, A. R.; Yous, S.; Stevens, R. C.; Weierstall, U.; Katritch, V.; Roth, B. L.; Liu, W.; Cherezov, V. Structural basis of ligand recognition at the human MT_1 melatonin receptor. *Nature* **2019**, 569, 284-8.

75 Johansson, L. C.; Stauch, B.; McCorvy, J. D.; Han, G. W.; Patel, N.; Huang, X.; Batyuk, A.; Gati, C.; Slocum, S. T.; Li, C.; Grandner, J. M.; Hao, S.; Olsen, R. H. J.; Tribo, A. R.; Zaare, S.; Zhu, L.; Zatsepin, N. A.; Weierstall, U.; Yous, S.; Stevens, R. C., Liu, W.; Roth, B. L.; Katritch, V.; Cherezov, V. XFEL structures of the human MT_2 melatonin receptor reveal the basis of subtype selectivity. *Nature* **2019**, 569, 289-92.

76 Ballesteros, J. A.; Weinstein, H. Integrated methods for the construction of three-dimensional models and computational probing of structure-function relations in G protein-coupled receptors. *J. Neurosci. Methods* **1995**, 25, 366-428.

77 Ishchenko, A.; Stauch, B.; Han, G. H.; Batyuk, A.; Shiriaeva, A.; Li, C.; Zatsepin, N.; Weierstall, U.; Liu, W.; Nango, E.; Nakane, T.; Tanaka, R.; Tono, K.; Joti, Y.; Iwata, S.; Moraes, I.; Gati, C.; Cherezov, V. Toward G protein-coupled receptor structure-based drug design using X-ray lasers. *IUCrJ* **2019**, 6, 1106-19.

78 Stauch, B.; Cherezov, V. Serial Femtosecond Crystallography of G Protein-Coupled Receptors. *Annu. Rev. Biophys.* **2018**, 47, 377-97.

79 Spence, J. C. H.; Weierstall, U.; Chapman, H. N. X-ray lasers for structural and dynamic biology. *Rep. Prog. Phys.* **2012**, 75, 102601.

80 Cecon, E.; Liu, L.; Jockers, R. Melatonin receptor structures shed new light on melatonin research. *J. Pineal Res.* **2019**, 67, e12606.

81 Nonno, R.; Lucini, V.; Pannacci, M.; Mazzucchelli, C.; Angeloni, D.; Fraschini, F.; Stankov, B.M. Pharmacological characterization of the human melatonin Mel_{1a} receptor following stable transfection into NIH3T3 cells. *Br. J. Pharmacol.* **1998**, 124, 485-92.

82 Roka, F.; Brydon, L.; Waldhoer, M.; Strosberg, D.; Freissmuth, M.; Jockers, R.; Nanoff, C. Tight association of the human Mel_{1a}-Melatonin Receptor and Gi: Precoupling and constitutive activity. *Mol. Pharmacol.* **1999**, 56, 1014-24.

83 Mazna, P.; Grycova, L.; Balik, A.; Zemkova, H.; Friedlova, E.; Obsilova, V.; Obsil, T.; Teisinger, J. The role of proline residues in the structure and function of human MT_2 melatonin receptor. *J. Pineal Res.* **2008**, 45, 361-72.

---

84 Schwartz, T. W.; Frimurer, T. M.; Holst, B.; Rosenkilde, B.; Elling, C. E. Molecular mechanism of 7TM receptor activation-a global toggle switch model. *Annu. Rev. Pharmacol. Toxicol.* **2006**, 46:481-519.

85 Katritch, V.; Fenalti, G.; Abola, E. E.; Roth, B. L.; Cherezov, V. Allosteric sodium in class A GPCR signaling. *Trends Biochem. Sci.* **2014**, 39, 233-44.

86 White, K. L.; Eddy, M. T.; Gao, Z. G.; Han, G. W.; Lian, T.; Deary, A.; Patel, N.; Jacobson, K. A.; Katritch, V.; Stevens, R. C. Structural connection between activation microswitch and allosteric sodium site in GPCR signaling. *Structure*. **2018**, 26, 259-69.

87 Wang, Q.; Lu, Q.; Guo, Q.; Teng, M.; Gong, Q.; Li, X.; Du, Y.; Liu, Z.; Tao, Y. Structural basis of the ligand binding and signaling mechanism of melatonin receptors. *Nat. Commun.* **2022**, 13, 454.

88 Palczewski, K.; Kumasaka, T.; Hori, T.; Behnke, C. A.; Motoshima, H.; Fox, B. A.; Le Trong, I.; Teller, D. C.; Okada, T.; Stenkamp, R. E.; Yamamoto, M.; Miyano, M. Crystal structure of rhodopsin: A G protein-coupled receptor. *Science.* **2000**, 289, 739-45.

89 Hurst, D. P.; Schmeisser, M.; Reggio, P. H. Endogenous lipid activated G protein-coupled receptors: emerging structural features from crystallography and molecular dynamics simulations. *Chem. Phys. Lipids* **2013**, 169, 46-56.

90 Audet, M.; Stevens, R. C. Emerging structural biology of lipid G protein-coupled receptors. *Protein Sci.* **2019**, 28, 292-304.

91 Shao, Z.; Yin, J.; Chapman, K.; Grzemska, M.; Clark, L.; Wang, J.; Rosenbaum, D. M. High-resolution crystal structure of the human CB$_1$ cannabinoid receptor. *Nature.* **2016**, 540, 602-6.

92 Clément, N.; Renault, N.; Guillaume, J.-L.; Cecon, E.; Journé, A.-S.; Laurent, X.; Tadagaki, T.; Cogé, F.; Gohier, A.; Delagrange, P.; Chavatte, P.; Jockers, R. Importance of the second extracellular loop for melatonin MT$_1$ receptor function and absence of melatonin binding in GPR$_{50}$. *Br. J. Pharmacol.* **2018**, 175, 3281-97.

93 Stauch, B.; Johansson, L. C.; Cherezov, V. Structural insights into melatonin receptors. *FEBS J.* **2020**, 287, 1496-510.

94 Kokkola, T.; Foord, S. M.; Watson, M.; Vakkuri, O.; Laitinen, J. T. Important amino acids for the function of the human MT$_1$ melatonin receptor. *Biochem. Pharmacol.* **2003**, 65, 1463-71.

95 Gerdin, M. J.; Mseeh, F.; Dubocovich, M. L. Mutagenesis studies of the human MT$_2$ melatonin receptor. *Biochem Pharmacol.* **2003**, 66, 315-20.

96 Okamoto, H. H.; Miyauchi, H.; Inoue, A.; Raimondi, F.; Tsujimoto, H.; Kusakizako, T.; Shihoya, W.; Yamashita, K.; Suno, R.; Nomura, N.; Kobayashi, T.; Iwata, S.; Nishizawa, T.; Nureki, O. Cryo-EM structure of the human MT$_1$-G$_i$ signaling complex. *Nat. Struct. Mol. Biol.* **2021**, 28, 694-701.

97 Rasmussen, S. G.; DeVree, B. T.; Zou, Y.; Kruse, A. C.; Chung, K. Y.; Kobilka, T. S.; Thian, F. S.; Chae, P. S.; Pardon, E.; Calinski, D.; Mathiesen, J. M.; Shah, S. T.; Lyons, J. A.; Caffrey, M.; Gellman, S. H.; Steyaert, J.; Skiniotis, G.; Weis, W. I.; Sunahara, R. K.; Kobilka, B. K. Crystal structure of the beta2 adrenergic receptor-Gs protein complex. *Nature* **2011**, 477, 549-55.

98 Boutin, J. A.; Witt-Enerby, P. A.; Sotriffer, C.; Zlotos, D. P. Melatonin receptor ligands: a pharmaco-chemical perspective. *J. Pineal Res.* **2020**, 69, e12672.

99 Stein, R. M.; Kang, H. J.; McCorvy, J. D.; Glatfelter, C. G.; Jones, A. J.; Che, T.; Slocum, S.; Huang, X.-P.; Savych, O.; Moroz, Y. S.; Stauch, B.; Johansson, L. C.; Cherezov, V.; Kenakin, T.; Irwin, J. J.; Shoichet, B. K.; Roth, B. L.; Dubocovich, M. L. Virtual discovery of melatonin receptor ligands to modulate circadian rhythms. *Nature.* **2020**, 579, 609-14.

100 Patel, N.; Huang, X.-P.; Grandner, J. M.; Johansson, L. C.; Stauch, B.; McCorvy, J. D.; Liu, Y.; Roth, B.; Katritch, V. Structure-based discovery of potent and selective melatonin receptor agonists. *Elife*. **2020**, 9, e53779-

---

101 Mor, M.; Spadoni, G.; Di Giacomo, B.; Diamantini, G.; Bedini, A.; Tarzia, G.; Plazzi, P. V.; Rivara, S.; Nonno, R.; Lucini, V.; Pannacci, M.; Fraschini, F.; Stankov, B. M. Synthesis, pharmacological characterization and QSAR studies on 2-substituted indole melatonin receptor ligands. *Bioorg. Med. Chem.* **2001**, 9, 1045-57.

102 Rivara, S.; Mor, M.; Silva, C.; Zuliani, V.; Vacondio, F.; Spadoni, G.; Bedini, A.; Tarzia, G.; Lucini, V.; Pannacci, M.; Fraschini, F.; Plazzi, P. V. Three-dimensional quantitative structure-activity relationship studies on selected MT$_1$ and MT$_2$ melatonin receptor ligands: requirements for subtype selectivity and intrinsic activity modulation. *J. Med. Chem.* **2003**, 10, 1429-39.

103 Uchikawa, O.; Fukatsu, K.; Tokunoh, R.; Kawada, M.; Matsumoto, K.; Imai, Y.; Hinuma, S.; Kato, K.; Nishikawa, H.; Hirai, K.; Miyamoto, M.; Ohkawa, S. Synthesis of a novel series of tricyclic indan derivatives as melatonin receptor agonists. *J. Med. Chem.* **2002**, 45, 4222-39.

104 Miyamoto, M. Pharmacology of ramelteon, a selective MT$_1$/MT$_2$ receptor agonist: a novel therapeutic drug for sleep disorders. *CNS Neurosci. Ther.* **2009**, 15, 32-51.

105 Lankford, D. A. Tasimelteon for insomnia. *Expert Opin. Invest. Drugs* **2011**, 20, 987993.

106 de Bodinat, C.; Guardiola-Lemaître, B.; Mocaër, E.; Renard, P.; Muñoz, C.; Millan, M. J. Agomelatine, the first melatonergic antidepressant: discovery characterization and development. *Nat. Rev. Drug Discovery* **2010**, 9, 628−642.

107 Millan, M. J.; Gobert, A.; Lejeune, F.; Dekeyne, A.; Newman-Tancredi, A.; Pasteau, V.; Rivet, J.-M.; Cussac, D. The novel melatonin agonist agomelatine (S20098) is an antagonist at 5-hydroxytryptamine2C receptors, blockade of which enhances the activity of frontocortical dopaminergic and adrenergic pathways. *J. Pharmacol. Exp. Ther.* **2003**, 306, 954-64.

108 Zemlan, F. P.; Mulchahey, J. J.; Scharf, M. B.; Mayleben, D. W.; Rosenberg, R.; Lankford, A. The efficacy and safety of the melatonin agonist β-methyl-6-chloromelatonin in primary insomnia: a randomized, placebo-controlled, crossover clinical trial. *J. Clin. Psychiatry* **2005**, 66, 384-90.

109 Oertel, J.; Golz, L.; Kirch, W. Elucidation of Neu-P11 metabolism in urine of volunteers by liquid chromatography-tandem mass spectrometry. *J Chromatogr A.* **2013**, 278, 69-75.

110 He, P.; Ouyang, X.; Zhou, S.; Yin, W.; Tang, C.; Laudon, M.; Tian, S. A novel melatonin agonist Neu-P11 facilitates memory performance and improves cognitive impairment in a rat model of Alzheimer' disease. *Horm. Behav.* **2013**, 64, 1-7.

111 Dubocovich, M. L.; Masana, M. I.; Iacob, S.; Sauri, D. M. Melatonin receptor antagonists that differentiate between the human Mel1a and Mel1b recombinant subtypes are used to assess the pharmacological profileof the rabbit retina ML1 presynaptic heteroreceptor. *Naunyn-Schmiedeberg's Arch. Pharmacol.* **1997**, 355, 365-75.

112 Audinot, V.; Mailliet, F.; Lahaye-Brasseur, C.; Bonnaud, A.; Le Gall, A.; Amossé, C.; Dromaint, S.; Rodriguez, M.; Nagel, N.; Galizzi, J. P.; Malpaux, B.; Guillaumet, G.; Lesieur, D.; Lefoulon, F.; Renard, P.; Delagrange, P.; Boutin, J. A. New selective ligands of human cloned melatonin MT$_1$ and MT$_2$ receptors. *Naunyn-Schmiedeberg's Arch. Pharmacol.* **2003**, 367, 553-61.

113 Dubocovich, M. L.; Takahashi, J. S. Use of 2-[^{125}I]iodomelatonin to characterize melatonin binding sites in chicken retina. *Proc. Natl. Acad. Sci. U S A.* **1987**, 84, 3916-20.

114 Tsotinis, A.; Vlachou, M.; Papahatjis, D. P.; Calogeropoulou, T.; Nikas, S. P.; Garratt, P. J.; Piccio, V.; Vonhoff, S.; Davidson, K.; Teh, M. T.; Sugden, D. Mapping the melatonin receptor. 7. Subtype selective ligands based on β-substituted N-acyl-5-methoxytryptamines and N-acyl-5-methoxy-1-methyl-tryptamines. *J. Med. Chem.* **2006**, 49, 3509-19.

115 Garratt, P. J.; Travard, S.; Vonhoff, S.; Tsotinis, A.; Sugden, D. Mapping the melatonin receptor. 4. Comparison of the binding affinities of a series of substituted phenylalkyl amides. *J. Med. Chem.* **1996**, 39, 1797-1805.

---

116 Carocci, A.; Catalano, A.; Lovece, A.; Lentini, G.; Duranti, A.; Lucini, V.; Pannacci, M.; Scaglione, F.; Franchini, C. Design, synthesis, and pharmacological effects of structurally simple ligands for MT$_1$ and MT$_2$ melatonin receptors. *Bioorg. Med. Chem.* **2010**, 18, 6496-511.

117 Rivara, S.; Lodola, A.; Mor, M.; Bedini, A.; Spadoni, G.; Lucini, V.; Pannacci, M.; Fraschini, F.; Scaglione, F.; Sanchez, R. O.; Gobbi, G.; Tarzia, G. N-(Substituted-anilinoethyl)amides: design, synthesis, and pharmacological characterization of a new class of melatonin receptor ligands. *J. Med. Chem.* **2007**, 50, 6618-26.

118 Bedini, A.; Spadoni, G.; Gatti, G.; Lucarini, S.; Tarzia, G.; Rivara, S.; Lorenzi, S.; Lodola, A.; Mor, M.; Lucini, V.; Pannacci, M.; Scaglione, F. Design and synthesis of N-(3,3-diphenylpropenyl)-alkanamides as a novel class of high-affinity MT$_2$-selective melatonin receptor ligands. *J. Med. Chem.* **2006**, 49, 7393-403.

119 Wallez, V.; Durieux-Poissonnier, S.; Chavatte, P.; Boutin, J. A.; Audinot, V.; Nicolas, J.-P.; Bennejean, C.; Delagrange, P.; Renard, P.; Lesieur, D. Synthesis and structure-affinity-activity relationships of novel benzofuran derivatives as MT$_2$ melatonin receptor selective ligands. *J. Med. Chem.* **2002**, 45, 2788-800.

120 El Kazzouli, S.; Griffon du Bellay, A.; Berteina-Raboin, S.; Delagrange, P.; Caignard, D. H.; Guillaumet, G. Design and synthesis of 2-phenylimidazo[1,2-a]pyridines as a novel class of melatonin receptor ligands. *Eur. J. Med. Chem.* **2011**, 46, 4252-7.

121 Jeanty, M.; Suzenet, F.; Delagrange, F.; Nosjean, O.; Boutin, J. A.; Caignard, D. H.; Guillaumet, G. Design and synthesis of 1-(2-alkanamidoethyl)-6-methoxy-7-azaindolederivatives as potent melatonin agonists. *Bioorg. Med. Chem. Lett.* **2011**, 21, 2316-9.

122 Fourmaintraux, E.; Depreux, P.; Lesieur, D.; Guardiola-Lemaître, B.; Bennejean, C.; Delagrange, P.; Howell, H. Tetrahydronaphthalenic derivatives as new agonist and antagonist ligands for melatonin receptors. *Bioorg. Med. Chem.* **1998**, 6, 9-13.

123 Spadoni, G., Bedini, A.; Lucarini, S.; Mari, M.; Caignard, D.-H.; Boutin, J. A.; Delagrange, P.; Lucini, V.; Scaglione, F.; Lodola, A.; Zanardi, F.; Pala, D.; Mor, M.; Rivara, S. Highly potent and selective MT$_2$ melatonin receptor full agonists from conformational analysis of 1-benzyl-2-acylaminomethyl-tetrahydroquinolines. *J. Med. Chem.* **2015**, 58, 7512-25.

124 Li, P.-K.; Chu, G.-H.; Gillen, M. L.; Witt-Enderby, P. A. Synthesis and receptor binding studies of quinolinic derivatives as melatonin receptor ligands. *Bioorg. Med. Chem. Lett.* **1997**, 7, 2177-80.

125 Karageorge, G. N.; Bertenshaw, S.; Iben, L.; Xu, C.; Sarbin, N.; Gentile, A.; Dubowchik, G. M. Tetrahydroisoquinoline derivatives as melatonin MT$_2$ receptor antagonists. *Bioorg. Med. Chem. Lett.* **2004**, 14, 5881-4.

126 Sun, L.-Q.; Chen, J.; Takaki, K.; Johnson, G.; Iben, L.; Mahle, C. D.; Ryan, E.; Xu, C. Design and synthesis of benzoxazole derivatives as novel melatoninergic ligands. *Bioorg. Med. Chem. Lett.* **2004**, 14, 1197-200.

127 Mésangeau, C.; Fraise, M.; Delagrange, P.; Caignard, D. H.; Boutin, J. A.; Berthelot, P.; Yous, S. Preparation and pharmacological evaluation of a novel series of 2-(phenylthio)benzo[b]thiophenes as selective MT$_2$ receptor ligands. *Eur. J. Med. Chem.* **2011**, 46, 1835-40.

128 Mor, M.; Rivara, S.; Pala, D.; Bedini, A.; Spadoni, G.; Tarzia, G. Recent advances in the development of melatonin MT$_1$ and MT$_2$ receptor agonists. *Expert Opin. Ther. Patents.* **2010**, 20, 1058-77.

129 Attia, M. I.; Julius, J.; Witt-Enderby, P. A.; Zlotos, D. P. Synthesis and pharmacological evaluation of 13a,14-dihydro-6*H*,13*H*pyrazino[1,2-a;4,5-a′]diindole analogs as melatonin receptor ligands. *Tetrahedron* **2007**, 63, 754-60.

130 Morellato, L.; Lefas-Le Gall, M.; Langlois, M.; Caignard, D.-H.; Renard, P.; Delagrange, P.; Mathé-Allainmat, M. Synthesis of new N-(arylcyclopropyl)acetamides and N-(arylvinyl)acetamides as conformationally-restricted ligands for melatonin receptors. *Bioorg. Med. Chem. Lett.* **2013**, 15, 430-4.

---

131 Mattson, R. J.; Catt, J. D.; Keavy, D.; Sloan, C. P.; Epperson, J.; Gao, Q.; Hodges, D. B.; Iben, L.; Mahle, C. D.; Ryan, E.; Yocca, F. D. Indanyl piperazines as melatonergic MT$_2$ selective agents. *Bioorg. Med. Chem. Lett.* **2003**, 13, 1199-202.

132 Rivara, S.; Diamantini, G.; Di Giacomo, B.; Lamba, D.; Gatti, G.; Lucini, V.; Pannacci, M.; Mor, M.; Spadoni, G.; Tarzia, G. Reassessing the melatonin pharmacophore--enantiomeric resolution, pharmacological activity, structure analysis, and molecular modeling of a constrained chiral melatonin analogue. *Bioorg Med Chem.* **2006**, 14, 3383-91.

133 Jellimann, C.; Mathé-Allainmat, M.; Andrieux, J.; Kloubert, S.; Boutin, J. A.; Nicolas, J. P.; Bennejean, C.; Delagrange, P.; Langlois, M. Synthesis of phenalene and acenaphthene derivatives as new conformationally restricted ligands for melatonin receptors. *J. Med. Chem.* **2000**, 43, 4051-62.

134 de la Fuente Revenga, M.; Fernández-Sáez, N.; Herrera-Arozamena, C.; Morales-García, J. A.; Alonso-Gil, S.; Pérez-Castillo, A.; Caignard, D.-H.; Rivara, S.; Rodríguez-Franco, M. I. Novel *N*-acetyl bioisosteres of melatonin: melatonergic receptor pharmacology, physicochemical studies, and phenotypic assessment of their neurogenic potential. *J. Med. Chem.* **2015**, 58, 4998-5014.

135 Faust, R.; Garratt, P. J.; Jones, R.; Yeh, L.-K.; Tsotinis, A.; Panoussopoulou, M.; Calogeropoulou, T.; Teh, M.-T.; Sugden, D. Mapping the melatonin receptor. 6. Melatonin agonists and antagonists derived from 6H-isoindolo[2,1-a]indoles, 5,6-dihydroindolo[2,1-a]isoquinolines, and 6,7-dihydro-5*H*-benzo[*c*]-azepino[2,1-*a*]indoles. *J. Med. Chem.* **2000**, 43, 1050-61.

136 Koike, T.; Hoashi, Y.; Takai, T.; Nakayama, M.; Yukuhiro, N.; Ishikawa, T.; Hirai, K.; Uchikawa, O. 1,6-Dihydro-2*H*-indeno[5,4-*b*]furan derivatives: design, synthesis, and pharmacological characterization of a novel class of highly potent MT$_2$-selective agonists. *J. Med. Chem.* **2011**, 54, 3436-44.

137 Koike, T.; Takai, T.; Hoashi, Y.; Nakayama, M.; Kosugi, Y.; Nakashima, M.; Yoshikubo, S.; Hirai, K.; Uchikawa, O. Synthesis of a novel series of tricyclic dihydrofuran derivatives: discovery of 8,9-dihydrofuro[3,2-c]pyrazolo[1,5-a]pyridines as melatonin receptor (MT$_1$/MT$_2$) Ligands. *J. Med. Chem.* **2011**, 54, 4207-18.

138 Kanayama, T.; Kubota, H.; Matsumoto, S.; Saito, T.; Shimizu, T.; Katoh, N.; Matsui, S. Astellas Pharma Inc., assignee. Indolecarboxamide derivatives. European Patent EP2873660B1. **2016** Oct 26.

139 Ferreira, M. A. Jr.; Azevedo, H.; Mascarello, A.; Segretti, N. D.; Russo, V.; Werneck Guimarães, C. R. Discovery of ACH-000143: a novel potent and peripherally preferred melatonin receptor agonist that reduces liver triglycerides and steatosis in diet-induced obese rats. *J. Med. Chem.* **2021**, 64, 4, 1904-29.

140 Nonno, R.; Lucini, V.; Spadoni, G.; Pannacci, M.; Croce, A.; Esposti, D.; Balsamini, C.; Tarzia, G.; Fraschini, F.; Stankov, B. M. A new melatonin receptor ligand with mt1-agonist and MT$_2$-antagonist properties. *J. Pineal Res.* **2000**, 29, 234-40.

141 Teh, M. T.; Sugden, D. Comparison of the structure-activity relationships of melatonin receptor agonists and antagonists: lengthening the *N*-acyl side-chain has differing effects on potency on Xenopus melanophores. *Naunyn Schmiedebergs Arch Pharmacol.* **1998**, 358, 522-8.

142 Bedini, A.; Lucarini, S.; Spadoni, G.; Tarzia, G.; Scaglione, F.; Dugnani, S.; Pannacci, M.; Lucini, V.; Carmi, C.; Pala, D.; Rivara, S.; Mor, M. Toward the definition of stereochemical requirements for MT$_2$-selective antagonists and partial agonists by studying 4-phenyl-2-propionamidotetralin (4-P-PDOT) derivatives. *J. Med. Chem.* **2011**, 54, 8362-72.

143 Lucini, V.; Pannacci, M.; Scaglione, F.; Rivara, S.; Mor, M.; Bordi, F.; Plazzi, P. V.; Spadoni, G.; Bedini, A.; Piersanti, G.; Diamantini, G.; Tarzia, G. Tricyclic alkylamides as melatonin receptor ligands with antagonist or inverse agonist activity. *J. Med. Chem.* **2004**, 47, 4202-12.

144 Devavry, S.; Legros, C.; Brasseur, C.; Delagrange, P.; Spadoni, G.; Cohen, W.; Malpaux, B.; Boutin, J. A.; Nosjean, O. Description of the constitutive activity of cloned human melatonin receptors hMT$_1$ and hMT$_2$ and discovery of inverse agonists. *J. Pineal Res.* **2012**, 53, 29-37.

---

145 Rivara, S.; Vacondio, F.; Fioni, A.; Silva, C:; Carmi, C.; Mor, M.; Lucini, V.; Pannacci, M.; Caronno, A.; Scaglione, F.; Gobbi, G.; Spadoni, G.; Bedini, A.; Orlando, P.; Lucarini, S.; Tarzia, G. N-(Anilinoethyl)amides: design and synthesis of metabolically stable, selective melatonin receptor ligands. *ChemMedChem.* **2009**, 4, 1746-55.

146 Yan, J.-H.; Su, H.-R.; Boutin, J. A.; Renard, M. P. ; Wang, M.-W. High-throughput screening assay for new ligands at human melatonin receptors. *Acta Pharmacol. Sin.* **2008**, 29, 515-21.

147 Boutin, J. A.; Bonnaud, A.; Brasseur, C.; Bruno, O.; Lepretre, N.; Oosting, P.; Coumailleau, S.; Delagrange, P.; Nosjean, O.; Legros, C. New MT_2 Melatonin Receptor-Selective Ligands: Agonists and Partial Agonists. *Int. J. Mol. Sci.* **2017**, 23, 1347.

148 Legros, C.; Brasseur, C.; Delagrange, P.; Ducrot, P.; Nosjean, O.; Boutin, J. A. Alternative Radioligands for Investigating the Molecular Pharmacology of Melatonin Receptors. *J. Pharmacol. Exp. Ther.* **2016**, 356, 681-92.

149 Dubocovich, M. L.; Cardinali, D. P.; Delagrange, P.; Krause, D. N.; Strosberg, A. D.; Sugden, D.; Yocca, F. D. Melatonin Receptors. *In The IUPHAR Compendium of Receptor Characterization and Classification*, 2nd ed.; Girdlestone, D., Ed.; IUPHAR Media: London, **2000**; pp. 270−277.

150 Descamps-Francois, C.; Yous, S.; Chavatte, P.; Audinot, V; Bonnaud, A.; Boutin, J. A.; Delagrange, P.; Bennejean, C.; Renard, P.; Lesieur, D. Design and synthesis of naphthalenic dimers as selective MT_1 melatoninergic ligands. *J. Med. Chem.* **2003**, 46, 1127-9.

151 Rivara, S.; Pala, D.; Lodola, A. Mor, M.; Lucini, V.; Dugnani, S.; Scaglione, F.; Bedini, A.; Lucarini, S.; Tarzia, G.; Spadoni, G. MT_1-selective melatonin receptor ligands: synthesis, pharmacological evaluation, and molecular dynamics investigation of N-{[(3-O-substituted)anilino]alkyl}amides. *ChemMedChem*. **2012**, 7, 1954-64.

152 Mésangeau, C.; Pérès, B.; Descamps-François, C.; Chavatte, P.; Audinot, V.; Coumailleau, S.; Boutin, J. A.; Delagrange, P.; Bennejean, C.; Renard, P.; Caignard, D. H.; Berthelot, P.; Yous, S. Design, synthesis and pharmacological evaluation of novel naphthalenic derivatives as selective MT_1 melatoninergic ligands. *Bioorg. Med. Chem.* **2010**, 18, 3426−36.

153 Bender, B. J.; Gahbauer, S.; Luttens, A.; Lyu, J.; Webb, C. M.; Stein, R. M.; Fink, E. A.; Balius, T. E.; Carlsson, J.; Irwin, J. J.; Shoichet, B. K. A practical guide to large-scale docking. *Nat. Protoc.* **2019**, 16, 4799–832.

154 Liu, L.; Jockers, R. Structure-based virtual screening accelerates GPCR drug discovery. *Trends Pharmacol Sci.* **2020**, 41, 382-4.

155 Wang, L.; Berne B. J.; Friesner, R. A. Ligand binding to protein-binding pockets with wet and dry regions. *Proc. Natl. Acad. Sci. U S A.* **2011**, 108, 1326-30.

156 Venkatakrishnan, A. J.; Ma, A. K.; Fonseca, R.; Latorraca, N. R.; Kelly, B.; Betz, R. M.; Asawa, C.; Kobilka, B. K.; Dror, R. Diverse GPCRs exhibit conserved water networks for stabilization and activation. *Proc. Natl. Acad. Sci. U S A.* **2019**, 116, 3288-93.

157 De Vivo, M.; Masetti, M.; Bottegoni, G.; Cavalli, A. Role of molecular dynamics and related methods in drug discovery. *J. Med. Chem.* **2016**, 59, 4035-61.

158 Decherchi, S.; Cavalli, A. Thermodynamics and Kinetics of Drug-Target Binding by Molecular Simulation. *Chem. Rev.* **2020**, 120, 12788-833.

159 Hénin, J.; Lelièvre, T., Shirts, M. R.; Valsson, O.; Delemotte, L. Enhanced Sampling Methods for Molecular Dynamics Simulations. *Living J. Comp. Mol. Sci.* **2022**, 4, 1583.

160 Grubmüller, H.; Heymann, B.; Tavan, P. Ligand binding: molecular mechanics calculation of the streptavidin-biotin rupture force. *Science.* **1996**, 271, 997-9.

161 Jarzynski, C. Nonequilibrium equality for free energy differences. *Phys. Rev. Lett.* **1997**, 78, 2690-3.

162 Park, S.; Khalili-Araghi, F.; Tajkhorshid, E.; Schulten, K. Free energy calculation from steered molecular dynamics simulations using Jarzynski's Equality. *J. Chem. Phys.* **2003**, 119, 3559.

---

163 Colizzi, F.; Perozzo, R.; Scapozza, L.; Recanatini, M.; Cavalli, A. Single-molecule pulling simulations can discern active from inactive enzyme inhibitors. *J. Am. Chem. Soc.* **2010**, 132, 7361-71.

164 Marchi, M.; Ballone, P. Adiabatic bias molecular dynamics: A method to navigate the conformational space of complex molecular systems. *J. Chem. Phys.* **1999**, 110, 3697-702.

165 G.M. Torrie and J.P. Valleau. Nonphysical sampling distributions in monte carlo free energy estimation: Umbrella sampling. *J. Comput. Phys.* **1997**, 23, 1977.

166 Kästner, J. Umbrella sampling. *WIREs Comput. Mol. Sci.* **2011**, 1, 932-42.

167 Kumar, S.; Rosenberg, J. M.; Bouzida, D.; Swendsen, R. H.; Kollman, P. A. The weighted histogram analysis method for free-energy calculations on biomolecules. I. The method. *J. Comput. Chem.* **1992**, 13, 1011-21.

168 Branduardi, D.; Gervasio, F. L.; Parrinello, M. From A to B in free energy space. *J. Chem. Phys.* **2007**, 126, 054103.

169 Branduardi, D.; De Vivo, M.; Rega, N.; Barone, V.; Cavalli, A. Methyl phosphate dianion hydrolysis in solution characterized by path collective variables coupled with DFT-based enhanced sampling simulations. *J. Chem. Theory Comput.* **2011**, 7, 539-43.

170 Lodola, A.; Branduardi, D.; De Vivo, M.; Capoferri, L.; Mor, M.; Piomelli, D.; Cavalli, A. A catalytic mechanism for Cysteine N-Terminal Nucleophile Hydrolases, as revealed by free energy simulations. *PLoS ONE* **2012**, 7, e32397.

171 Roca, M.; Navas-Yuste, S.; Zinovjev, K.; López-Estepa, M.; Gómez, S.; Fernández, F. J.; Vega, M. C.; Tuñón, I. Elucidating the catalytic reaction mechanism of Orotate Phosphoribosyltransferase by means of X-ray crystallography and computational simulations. *ACS Catal.* **2020**, 10, 1871-85.

172 Laio, A.; Parrinello, M. Escaping free energy minima. *Proc. Natl. Acad. Sci. USA*. **2002**, 99, 12562-6.

173 Bussi, G.; Branduardi, D. Free-energy calculations with metadynamics: Theory and practice. *Rev. Comput. Chem.* **2015**, 28, 1-49.

174 Barducci, A.; Bussi, G.; Parrinello, M. Well-tempered metadynamics: A smoothly converging and tunable free-energy method. *Phys. Rev. Lett.* **2008**, 100, 020603.

175 Bussi, G.; Laio. A. Using metadynamics to explore complex free-energy landscapes. *Nat. Rev. Phys.* **2020**, 2, 200-12

176 Raiteri, P.; Laio, A.; Gervasio, F. L.; Micheletti, C.; Parrinello, M. Efficient reconstruction of complex free energy landscapes by multiple walkers metadynamics. *J. Phys. Chem. B.* **2006**, 3533-9.

177 Bussi, G.; Gervasio, F. L.; Laio, A.; Parrinello, M. Free-energy landscape for β hairpin folding from combined parallel tempering and metadynamics. *J. Am. Chem. Soc.* **2006**, 128, 13435-41.

178 Tiwary, P.; Parrinello, M. A time-independent free energy estimator for metadynamics. *J. Phys. Chem. B.* **2015**, 119, 736-42.

179 Mey, A. S. J. S.; Allen, B. K.; Macdonald, H. E. B.; Chodera, J. D.; Hahn, D. F.; Kuhn, M.; Michel, J.; Mobley, D. L.; Naden, L. N.; Prasad, S.; Rizzi, A.; Scheen, J.; Shirts, M. R.; Tresadern, G.; Xu, H. Best practices for alchemical free energy calculations. *Living J. Comput. Mol. Sci.* **2020**, 2, 18378.

180 Kirkwood, J. G. Statistical mechanics of fluid mixtures. *J. Chem. Phys.* **1935**, 3, 300.

181 Steinbrecher, T.; Mobley, D. L.; Case, D. A. Nonlinear scaling schemes for Lennard-Jones interactions in free energy calculations. *J. Chem. Phys.* **2007**, 127, 214108.

182 Liu, H.; Mark, A. E.; van Gunsteren, W. F. Estimating the relative free energy of different molecular states with respect to a single reference state. *J. Phys. Chem.* **1996**, 100, 9485-94.

183 Song, L. F.; Lee, T.-S.; Zhu, C.; York, D. M.; Merz, K. M. Jr. Using AMBER18 for Relative Free Energy Calculations. *J. Chem. Inf. Model.* **2019**, 59, 3128-35.

---

184 Vauquelin, G.; Van Liefde, I.; Swinney, D. C. Radioligand binding to intact cells as a tool for extended drug screening in a representative physiological context. *Drug Discov. Today Technol.* **2015**, 17, 28-34.

185 Legros, C.; Devavry, S.; Caignard, S.; Tessier, C. ; Delagrange, P.; Ouvry, C.; Boutin, J. A.; Nosjean, O. Melatonin MT$_1$ and MT$_2$ receptors display different molecular pharmacologies only in the G-protein coupled state. *Br. J. Pharmacol.* **2014**, 171, 186-201.

186 Nishiyama, K.; Hirai, K. In vitro comparison of duration of action of melatonin agonists on melatonin MT$_1$ receptor: possible link between duration of action and dissociation rate from the receptor. *Eur. J. Pharmacol.* **2015**, 757, 42-52.

187 Dror, R. O.; Pan, A. C.; Arlow, D. H.; Borhani, D. W.; Maragakis, P.; Shan, Y.; Xu, H.; Shaw, D. E. Pathway and mechanism of drug binding to G-protein-coupled receptors. *Proc. Natl. Acad. Sci. U. S. A.* **2011**, 108, 13118-23.

188 Bongiorno, D.; Ceraulo, L.; Feruggia, F.; Filizzola, F.; Ruggirello, A.; Liveri, V. T. Localization and interactions of melatonin in dry cholesterol/lecithin mixed reversed micelles used as cell membrane models. *J. Pineal Res.* **2005**, 38, 292-298.

189 Spadoni, G.; Bedini, A.; Furiassi, L.; Mari, M.; Mor, M.; Scalvini, L.; Lodola, A.; Ghidini, A.; Lucini, V.; Dugnani, S.; Scaglione, F.; Piomelli, D.; Jung, K.-M.; Supuran, C. T.; Lucarini, L.; Durante, M.; Sgambellone, S.; Masini, E.; Rivara, S. Identification of bivalent ligands with melatonin receptor agonist and Fatty Acid Amide Hydrolase (FAAH) inhibitory activity that exhibit ocular hypotensive effect in the rabbit.. *J. Med. Chem.* **2018**, 61, 7902-16.

190 *Schrödinger Release 2018-2: Glide 7.9*, Schrödinger, LLC, New York, NY, 2018.

191 Friesner, R. A.; Banks, J. L.; Murphy, R. B. Glide: A new approach for rapid, accurate docking and scoring. 1. Method and assessment of docking accuracy. *J. Med. Chem.* **2004**, 47, 1739-49.

192 *Schrödinger Release 2018-2: MacroModel 12.0*, Schrödinger, LLC, New York, NY, 2018.

193 Roos, K.; Wu, C.; Damm, W.; Reboul, M.; Stevenson, J. M.; Lu, C.; Dahlgren, M. K.; Mondal, S.; Chen, W.; Wang, L.; Abel, R.; Friesner, R. A.; Harder, E. D. OPLS3e: Extending force field coverage for drug-like small molecules. *J. Chem. Theory Comput.* **2019**, 15, 1863-74.

194 Wu, E. L.; Cheng, X.; Jo, S.; Rui, H.; Song, K. C.; Dávila-Contreras, E. M.; Qi, Y.; Lee, J.; Monje-Galvan, V.; Venable, R. M.; Klauda, J. B.; Im, W. CHARMM-GUI Membrane Builder toward realistic biological membrane simulations. *J. Comput. Chem.* **2014**, 35, 1997-2004.

195 Jorgensen, W. L.; Chandrasekhar, J.; Madura, J. D. Comparison of simple potential functions for simulating liquid water. *J. Chem. Phys.* **1983**, 79, 926.

196 Maier, J. A.; Martinez, C.; Kasavajhala, K.; Wickstrom, L.; Hauser, K. E.; Simmerling, C. ff14SB: Improving the accuracy of protein side chain and backbone parameters from ff99SB. *J. Chem. Theory Comput.* **2015**, 11, 3696-713.

197 Wang, J.; Wolf, R. M.; Caldwell, J. W.; Kollman, P. A.; Case, D. A. Development and testing of a general amber force field. *J. Comput. Chem.* **2004**, 25, 1157-74.

198 Joung, I. S.; Cheatham, T. E. Determination of alkali and halide monovalent ion parameters for use in explicitly solvated biomolecular simulations. *J. Phys. Chem. B.* **2008**, 112, 9020-41.

199 *Schrödinger Release 2018-2: Jaguar 10.0*, Schrödinger, LLC, New York, NY, 2018.

200 Bochevarov, A. D.; Harder, E.; Hughes, T. F.; Greenwood, J. R.; Braden, D. A.; Philipp, D. M.; Rinaldo, D.; Halls, M. D.; Zhang, J.; Friesner, R. A. Jaguar: a high-performance quantum chemistry software program with strengths in life and materials sciences. *Int. J. Quantum Chem.* **2013**, 113, 2110-42.

201 Cornell, W. D.; Cieplak, P.; Bayly, C. I.; Kollman, P. A. Application of RESP charges to calculate conformational energies, hydrogen bond energies and free energies of solvation. *J. Am. Chem. Soc.* **1993**, 115, 9620-31.

202 Abraham, M. J.; Murtola, T.; Schulz, R.; Páll, S.; Smith, J. C.; Hess, B.; Lindahl, E. GROMACS: High performance molecular simulations through multi-level parallelism from laptops to supercomputers. *SoftwareX* **2015**, 1-2, 19-25.

---

203 Tribello, G. A.; Bonomi, M.; Branduardi, D.; Camilloni, C.; Bussi, G. PLUMED2: New feathers for an old bird. *Comp. Phys. Comm.* **2014**, 185, 604.

204 Essmann, U.; Perera, L.; Berkowitz, M. L.; Darden, T.; Lee, H.; Pedersen, L. G. A smooth particle mesh Ewald method. *J. Chem. Phys.* **1995**, 103, 8577-93.

205 Hess, B.; Bekker, H.; Berendsen, H. J. C.; Fraaije J. G. E. M. LINCS: A linear constraint solver for molecular simulations. *Comput. Chem.* **1997**, 18, 1463-72.

206 Nosé S. A Molecular Dynamics Method for Simulations in the Canonical Ensemble. *Mol. Phys.* **1984**, 52, 255-68.

207 Hoover WG. Canonical dynamics: Equilibrium phase-space distributions. *Phys. Rev. A* **1985**, 31, 1695.

208 Kearsley, S. L. On the orthogonal transformation used for structural comparisons. *Acta Cryst. A*. **1989**, 45, 208-10.

209 Catmull, E.; Rom, R. A class of local interpolating splines. In *Computer aided geometric design*, 1st ed..; New York: Academic Press. In: Barnhill R. E. & Riesenfeld R. F., **1974**; pp. 317–332.

210 Jónsson, H.; Mills, G.; Jacobsen, K. W. *Classical Dynamics in Condensed Phase Simulations*. In: B. J. Berne, G. Ciccotti, and D. F. Coker; World Scientific, Singapore, **1998**; p. 385-404.

211 Pratt, L. R. A statistical method for identifying transition states in high dimensional problems. *J. Chem. Phys.* **1986**, 85, 5045.

212 Favia, A. D.; Masetti, M.; Recanatini, M.; Cavalli, A. Substrate binding process and mechanistic functioning of type 1 11β-hydroxysteroid dehydrogenase from enhanced sampling methods. *PLoS One* **2011**, 6, e25375.

213 Laidler, K. J.; King, M. C., Development of transition-state theory. *J. Phys. Chem.* **1983**, 87, 2657-64.

214 Lu, H.; Martí, J. Binding and dynamics of melatonin at the interface of phosphatidylcholine-cholesterol membranes. PLoS One. 2019, 14, e0224624.

215 Lu, H.; Martí, J. Cellular absorption of small molecules: free energy landscapes of melatonin binding at phospholipid membranes. *Sci. Rep.* **2020**, 10, 9235.

216 Vauquelin, G. On the 'micro'-pharmacodynamic and pharmacokinetic mechanisms that contribute to long-lasting drug action. *Expert Opin. Drug Discov.* **2015**, 10, 1085−98.

217 Warne, T.; Edwards, P. C.; Doré, A. S.; Leslie, A. G. W.; Tate, C. G. Molecular basis for high-affinity agonist binding in GPCRs. *Science* **2019**, 364, 775-78.

218 Karamitri, A.; Sadek, M. S.; Journé, A.-S.; Gbahou, F.; Gerbier, R.; Osman, M. B.; Habib, S. A. M. ; Jockers, R.; Zlotos, D. P. O-linked melatonin dimers as bivalent ligands targeting dimeric melatonin receptors. Bioorg. Chem. 2019, 85, 349-56.

219 Fu, C.-F.; Tian, S. X. Different aggregation dynamics of benzene-water mixtures. *Phys. Chem. Chem. Phys.* **2014**, 16, 21957.

220 Cammarota, M.; Ferlenghi, F.; Vacondio, F.; Vincenzi, F.; Varani, K.; Bedini, A.; Rivara, S.; Mor, M.; Boscia, F. Combined targeting of fatty acid amide hydrolase and melatonin receptors promotes neuroprotection and stimulates inflammation resolution in rats. *Br. J. Pharmacol.* **2022** Dec. 16. Doi: 10.1111/bph.16014. Online ahead of print.

221 Tarzia, G.; Duranti. A.; Tontini, A.; Piersanti, G.; Mor, M.; Rivara, S.; Plazzi, P. V.; Park, C.; Kathuria, S.; Piomelli, D. Design, synthesis, and structure-activity relationships of alkylcarbamic acid aryl esters, a new class of fatty acid amide hydrolase inhibitors. *J. Med. Chem.* **2003**, 46, 2352–60.

222 Hanson, M. A.; Roth, C. B.; Jo, E.; Griffith, M. T.; Scott, F. L.; Reinhart, G.; Desale, H.; Clemons, B.; Cahalan, S. M.; Schuerer, S. C.; Germana Sanna, M.; Han, G. W.; Kuhn, P.; Rosen, H.; Stevens, R. C. Crystal structure of a lipid G Protein−Coupled Receptor. *Science*. **2012**, 335, 851-5.

223 Shao, Z.; Yin, J.; Chapman, K.; Grzemska, M.; Clark, L.; Wang, J.; Rosenbaum, D. M. High-resolution crystal structure of the human CB_1 cannabinoid receptor. *Nature.* **2016**, 540, 602-6.

---

224 Lu, J.; Byrne, N.; Wang, J.; Bricogne, G.; Brown, F. K.; Chobanian, H. R.; Colletti, S. L.; Di Salvo, J.; Thomas-Fowlkes, B.; Guo, Y.; Hall, D. H.; Hadix, J.; Hastings, N. B.; Hermes, J. D.; Ho, T.; Howard, A. D.; Josien, H.; Kornienko, M.; Lumb, K. J.; Miller, M. W.; Patel, S. B.; Pio, B.; Plummer, C. H.; Sherborne, B. S.; Sheth, P.; Souza, S.; Tummala, S.; Vonrhein, C.; Webb, M.; Allen, S. J.; Johnston, J. M.; Weinglass, A. B.; Sharma, S.; Soisson, S. M. Structural basis for the cooperative allosteric activation of the free fatty acid receptor GPR40. *Nat. Struct. Mol. Biol.* **2017**, 24, 570-7.

225 Cao, D.; Yu, J.; Wang, H.; Luo, Z.; Liu, X.; He, L.; Qi, L.; Fan, L.; Tang, L.; Chen, Z.; Li, J.; Cheng, J.; Wang, S. Structure-based discovery of nonhallucinogenic psychedelic analogs. *Science*. **2022**, 375, 403-411.

226 Fronik, P.; Gaiser, B. I.; Sejer Pedersen, D. Bitopic ligands and metastable binding sites: opportunities for G Protein-Coupled Receptor (GPCR) Medicinal Chemistry. *J. Med. Chem.* **2017**, 60, 4126-34,

227 Lane, J. R.; Sexton, P. M.; Christopoulos, A. Bridging the gap: bitopic ligands of G-protein-coupled receptors. *Trends Pharmacol. Sci.* **2013**, 34, 59-66.

228 Kruse, A. C.; Hu, J.; Pan, A. C.; Arlow, D. H.; Rosenbaum, D. M.; Rosemond, E.; Green, H. F.; Liu, T.; Chae, P. S.; Dror, R. O.; Shaw, D. E.; Weis, W. I.; Wess, J.; Kobilka, B. K. Structure and dynamics of the M_3 muscarinic acetylcholine receptor. *Nature*. **2012**, 482, 552-6.

229 Gaiser, B.; Danielsen, M.; Marcher-Rørsted, E.; Røpke Jørgensen, K.; Wróbel, T. M.; Frykman, M.; Johansson, H.; Bräuner-Osborne, H.; Gloriam, D. E.; Mathiesen, J. M.; Sejer Pedersen, D. Probing the existence of a metastable binding site at the β_2-adrenergic receptor with homobivalent bitopic ligands. *J. Med. Chem.* **2019**, 62, 7806-39.

230 Gado, F.; Ferrisi, R.; Polini, B.; Mohamed, K. A.; Ricardi, C.; Lucarini, E.; Carpi, S.; Domenichini, F.; Stevenson, L. A.; Rapposelli, S.; Saccomanni, G.; Nieri, P.; Ortore, G.; Pertwee, R. G.; Ghelardini, C.; Di Cesare Mannelli, L.; Chiellini, G.; Laprairie, R. L.; Manera, C. Design, synthesis, and biological activity of new CB_2 receptor ligands: from orthosteric and allosteric modulators to dualsteric/bitopic ligands. *J. Med. Chem.* **2022**, 65, 9918-38.

231 Morales, P.; Navarro, G.; Gómez-Autet, M.; Redondo, L.; Fernández-Ruiz, J.; Pérez-Benito, L.; Cordomí, A.; Pardo, L.; Franco, R.; Jagerovic, N. Discovery of homobivalent bitopic ligands of the Cannabinoid CB_2 receptor. *Chemistry*. **2020**, 26, 15839-42.

232 Casajuana-Martin, N.; Navarro, G.; Gonzalez, A.; Llinas del Torrent, C.; Gómez-Autet, M.; Quintana García A, Franco R, Pardo L. A single point mutation blocks the entrance of ligands to the Cannabinoid CB_2 receptor via the lipid bilayer. *J. Chem. Inf. Model.* **2022**, 62, 5771-9.

233 Payandeh, J.; Volgraf, M. Ligand binding at the protein-lipid interface: strategic considerations for drug design. *Nat. Rev. Drug Discovery* **2021**, 20, 710-22.

234 Tian, H.; Gunnison, K. M.; Kazmi, M. A.; Sakmar, T. P.; Huber, T. FRET sensors reveal the retinal entry pathway in the G protein-coupled receptor rhodopsin. *iScience*. **2022**, 25, 104060.

235 Papa, A.; Pasquini, S.; Contri C.; Gemma, S.; Campiani, G.; Butini, S.; Varani, K., Vincenzi, F. Polypharmacological Approaches for CNS Diseases: Focus on Endocannabinoid Degradation Inhibition. *Cells*. **2022**, 11, 471.

236 Jansen, J. M.; Copinga, S.; Gruppen, G.; Molinari, E. J.; Dubocovich, M. L.; Grol, C. J. The high affinity melatonin binding site probed with conformationally restricted ligand--I. Pharmacophore and minireceptor models. *Bioorg. Med. Chem.* **1996**, 4, 1321-32.

237 Spadoni, G.; Balsamini, C.; Diamantini, G.; Di Giacomo, B.; Tarzia, G.; Mor, M.; Plazzi, P. V.; Rivara, S.; Lucini, V.; Nonno, R.; Pannacci, M.; Fraschini, F.; Stankov, B. M. Conformationally restrained melatonin analogs: synthesis, binding affinity for the melatonin receptor, evaluation of the biological activity, and molecular modeling study. *J. Med. Chem.* **1997**, 40, 1990-2002.

238 Tsotinis, A.; Vlachou, M.; Papahatjis, D. P.; Calogeropoulou, T.; Nikas, S. P.; Garratt, P. J.; Piccio, V.; Vonhoff, S.; Davidson, K.; Teh, M. T.; Sugden, D. Mapping the melatonin receptor. 7. Subtype selective ligands based on β-substituted N-acyl-5-methoxytryptamines and N-acyl-5-methoxy-1-methyl-tryptamines. *J. Med. Chem.* **2006**, 49, 3509-19.

239 Ettaoussi, M.; Sabaouni, A.; Pérès, B.; Landagaray, E.; Nosjean, O.; Boutin, J.A.; Caignard, D.-H.; Delagrange, P.; Berthelot, P.; Yous, S. Synthesis and pharmacological evaluation of a series of the agomelatine analogues as melatonin MT_1 /MT_2 agonist and 5-HT_{2C} antagonist. *ChemMedChem.* **2013**, 8, 1830-45.

240 Ettaoussi, M.; Pérès, B.; Jarry, C.; Nosjean, O.; Boutin, J.A.; Gohier, A.; Mannoury la Cour, C.; Caignard, D.-H.; Delagrange, P.; Berthelot, P.; Yous, S. Synthesis, chiral resolution, absolute configuration assignment and pharmacological evaluation of a series of melatoninergic ligands. *Med. Chem. Commun.* **2014**, 5, 1303-8.

241 Spadoni, G.; Balsamini, C.; Bedini, A.; Diamantini, G.; Di Giacomo, B.; Tontini, A.; Tarzia, G.; Mor, M.; Plazzi, P.V.; Rivara, S.; et al. 2-[N-Acylamino(C1-C3)alkyl]indoles as MT1 melatonin receptor partial agonists, antagonists, and putative inverse agonists. *J. Med. Chem.* **1998**, 41, 3624-34.

242 Bartoccini, F.; Venturi, S.; Retini, M.; Mari, M.; Piersanti, G. Total synthesis of (-)-clavicipitic acid via γ,γ-dimethylallyltryptophan (DMAT) and chemoselective C–H hydroxylation. *J. Org. Chem.* **2019**, 84, 8027-34.

243 Y. Cheng, W.H. Prusoff. Relationship between the inhibition constant (Ki) and the concentration of inhibitor which causes 50% inhibition (IC_{50}) of an enzymatic reaction. *Biochem. Pharmacol.* **1973**, 22, 3099-108.

244 Evans D. A., Britton T. C., Ellman J. A. Contrasteric carboximide hydrolysis with lithium hydroperoxide. *Tetrahedron Letters*, **1987**, 28, 6141-4.

245 Tsotinis, A. Afroudakis, P. A.; Papanastasiou, I. P. ; Sakellaropoulou, A. ; Boniakou, M.; Komiotis, D.; Garratt, P. J.; Delagrange, P.; Bocianowska-Zbrog, A.; Sugden, D. Mapping the Melatonin Receptor. 8. Selective MT_2 Agonists Derived from 5,6-Dihydroindolo[2,1-*a*]isoquinolines and Related Systems. *ChemMedChem*. **2022**, e202200129

246 *Schrödinger Release 2018-2: Maestro 11.6*; Schrödinger, LLC: New York, NY, USA, 2018.

247 Still, W.C.; Tempczyk, A.; Hawley, R.C.; Hendrickson, T. Semianalytical treatment of solvation for molecular mechanics and dynamics. *J. Am. Chem. Soc.* **1990**, 112, 6127-9.

248 *Schrödinger Release 2018-2: Prime 5.2*, Schrödinger, LLC, New York, NY, 2018.

249 Hassan-Mohamed, I.; Giorgio, C.; Incerti, M.; Russo, S.; Pala, D.; Pasquale, E. B.; Zanotti, I.; Vicini, P.; Barocelli, E.; Rivara, S.; Mor, M.; Lodola, A.; Tognolini, M. UniPR 129 is a competitive small molecule Eph-ephrin antagonist blocking in vitro angiogenesis at low micromolar concentrations. *Br. J. Pharmacol.* **2014**, 171, 5195-208.

250 Polak, E.; Ribière, G. Note sur la convergence de méthodes de directions conjuguées. *ESAIM Math. Model. Numer. Anal. Modél. Math. Anal. Numér.* **1969**, 3, 35-43.

251 *Schrödinger Release 2018-2: Desmond 5.4*, Schrödinger, LLC, New York, NY, 2018.

252 Kräutler, V.; Van Gunsteren, W. F.; Hünenberger, P. H. A fast SHAKE algorithm to solve distance constraint equations for small molecules in molecular dynamics simulations. *J. Comput. Chem.* **2001**, 22, 501-8.

253 Essmann, U.; Perera, L.; Berkowitz, M. L.; Darden, T.; Lee, H.; Pedersen, L. G. A smooth particle mesh Ewald method. *J. Chem. Phys.* **1995**, 103, 8577-93.

254 Tuckerman, M.; Berne, B. J.; Martyna, G. J. Reversible multiple time scale molecular dynamics. *J. Chem. Phys.* **1992**, 97, 1990-2001.

255 Feller, S. E.; Zhang, Y.; Pastor, R. W.; Brooks, B. R. Constant pressure molecular dynamics simulation: The Langevin piston method. *J. Chem. Phys.* **1995**, 103, 4613-21.

---

256 Klauda, J. B.; Venable, R. M.; Freites, J. A.; O'Connor, J. W.; Tobias, D. J.; Mondragon-Ramirez, C.; Vorobyov, I.; MacKerell, A. D.; Pastor, R. W. Update of the CHARMM all-atom Additive force field for lipids: Validation on six lipid types. *J. Phys. Chem. B* **2010**, 114, 7830-43.

257 Holst, B.; Nygaard, R.; Valentin-Hansen, L.; Bach, A.; Engelstoft, M. S.; Petersen, P. S.; Frimurer, T. M.; Schwartz, T. W. A conserved aromatic lock for the tryptophan rotameric switch in TM-VI of seven-transmembrane receptors. *J. Biol. Chem.* **2010**, 285, 3973-85.

258 Landagaray, E.; Ettaoussi, M.; Leclerc, V.; Traoré, B.; Perez, V.; Nosjean, O.; Boutin, J. A.; Caignard, D.-H.; Delagrange, P.; Berthelot, P.; Yous, S. New melatonin (MT_1/MT_2) ligands: design and synthesis of (8,9-dihydro-7*H*-furo[3,2-*f*]chromen-1-yl) derivatives. *Bioorg. Med. Chem.* **2014**, 22, 986-96.

259 Poissonnier-Durieux, S:, Ettaoussi, M.; Pérès, B.; Boutin, J. A.; Audinot, V.; Bennejean, C.; Delagrange, P.; Caignard, D.-H.; Renard, P.; Berthelot, P.; Lesieur, D.; Yous, S. Synthesis of 3-phenylnaphthalenic derivatives as new selective MT_2 melatoninergic ligands, *Bioorg. Med. Chem.* **2008**, 16, 8339-48.

260 Zlotos, D. P., Attia, M. I., Julius, J.; Sethi, S.; Witt-Enderby, P. A. 2-[(2,3-dihydro-1*H*indol-1-yl)methyl]melatonin analogues: a novel class of MT_2-selective melatonin receptor antagonists, *J. Med. Chem.* **2009**, 52, 826-33.

261 Heckman, D.; Attia, M. I.; Behnam, M. A. M.; Mohsen, A. M. Y.; Markl, C.; Julius, J.; Sethi, S.; Witt-Enderby, P. A.; Zlotos, D. P. 2-[(1,3-Dihydro-2*H*-isoindol-2-yl)methyl]-melatonin - a novel MT_2-selective melatonin receptor antagonist, *Med. Chem. Commun.* **2011**, 2, 991.

262 Markl, C.; Attia, M. I.; Julius, J.; Sethi, S.; Witt-Enderby, P. A.; Zlotos, D. P. Synthesis and pharmacological evaluation of 1,2,3,4-tetrahydropyrazino[1,2-*a*]indole and 2-[(phenylmethylamino)methyl]-1*H*-indole analogues as novel melatoninergic ligands, *Bioorg. Med. Chem.* **2009**, 17, 4583-94.

263 Larsen, M. A.; Hartwig, J. F. Iridium-catalyzed C–H borylation of heteroarenes: scope, regioselectivity, application to late-stage functionalization, and mechanism, *J. Am. Chem. Soc.* **2014**, 136, 4287-99.,

264 Couhert, A.; Delagrange, P.; Caignard, D.-H.; Chartier, A.; Suzenet, G.; Guillaumet F. Synthesis of 2-arylfuro[3,2-*b*]pyridines: effect of the C2-aryl group on melatoninergic activity. *Eur. J. Med. Chem.* **2016**, 109, 268-75.

265 Rivara, S.; Lorenzi, S.; Mor, M.; Plazzi, P. V.; Spadoni, G.; Bedini, A.; Tarzia, G. Analysis of Structure−Activity Relationships for MT_2 Selective Antagonists by Melatonin MT_1 and MT_2 Receptor Models. *J. Med. Chem.* **2005**, 48, 4049-60.

266 Jespers, W.; Oliveira, A. Prieto-Díaz, R.; Majellaro, M.; Åqvist, J.; Sotelo, E.; Gutiérrez-de-Terán, H. Structure-Based Design of Potent and Selective Ligands at the Four Adenosine Receptors. *Molecules.* **2017**, 22, 1945.

267 Jespers, W.; Heitman, L. H.; IJzerman, A. P.; Sotelo, E.; van Westen, G. J. P.; Åqvist, J.; Gutiérrez-de-Terán, H. Deciphering conformational selectivity in the A_{2A} adenosine G protein-coupled receptor by free energy simulations. *PLoS Comput. Biol.* **2021**, 17, e1009152.

268 Dupré, C.; Bruno, O.; Bonnaud, A.; Giganti, A.; Nosjean, O.; Legros, C.; Boutin, J.A. Assessments of cellular melatonin receptor signaling pathways: β-arrestin recruitment, receptor internalization, and impedance variations. *Eur. J. Pharmacol.* **2018**, 818, 534–544.

269 Beresford, I. J.; Browning, C.; Starkey, S. J.; Brown, J.; Foord, S.M.; Coughlan, J.; North, P. C.; Dubocovich, M. L.; Hagan, R. M. GR196429: a nonindolic agonist at high-affinity melatonin receptors. *J. Pharmacol. Exp. Ther.* **1998**, 285, 1239-45.

270 Duroux, R.; Rami, M.; Landagaray, E.; Ettaoussi,M.; Caignard, D.-H.; Delagrange, P.; Melnyk, P.; Yous, S. Synthesis and biological evaluation of new naphtho-and quinolinocyclopentane derivatives as potent melatoninergic (MT_1/MT_2) and serotoninergic ($5\text{-}HT_{2C}$) dual ligands. *Eur. J. Med. Chem.* **2017**, 141, 552-66.

---

271 Landagaray, E.; Ettaoussi, M.; Rami, M.; Boutin, J. A.; Caignard, D. H.; Delagrange, P.; Melnyk, P.; Berthelot, P.; Yous, S. New quinolinic derivatives as melatonergic ligands: Synthesis and pharmacological evaluation. *Eur. J. Med. Chem.* **2017**, 127, 621-31.

272 Lipinski, C. A.; Lombardo, F.; Dominy, B. W.; Feeney, P. J. Experimental and computational approaches to estimate solubility and permeability in drug discovery and development settings. *Adv. Drug Delivery Rev.* **2001**, 46, 3-26.

273 Sherman, W.; Day, T.; Jacobson, M. P.; Friesner, R. A.; Farid, R. Novel procedure for modeling ligand/receptor induced fit effects. *J. Med. Chem.* **2006**, 49, 534-53.

274 Jacobson, M. P.; Friesner, R. A.; Xiang, Z.; Honig, B. On the role of the crystal environment in determining protein side-chain conformations. *J. Mol. Biol.* **2002**, 320, 597-608.

275 Xie, D.; Schlick, T. Efficient implementation of the truncated-Newton algorithm for large-scale chemistry applications. *SIAM J. Optim.* **1999**, 10, 132-54.

276 He, X.; Liu, S.; Lee, T.-S.; Ji, B.; Manm V. H.; York, D. M.; Wang, J. Fast, accurate, and reliable protocols for routine calculations of protein-ligand binding affinities in drug design projects using AMBER GPU-TI with ff14SB/GAFF. *ACS Omega*. **2020**, 5, 4611-9.

277 Loncharich, R. J.; Brooks, B. R.; Pastor, R. W. Langevin dynamics of peptides: the frictional dependence of isomerization rates of *N*-acetylalanyl-*N'*-methylamide. *Biopolymers*. **1992**, 32, 523-35.

278 Faller, R.; de Pablo, J. J. Constant pressure hybrid Molecular Dynamics-Monte Carlo simulations. *J. Chem. Phys.* **2002**, 116.

279 Cherezov, V.; Rosenbaum, D. M.; Hanson, M. A.; Rasmussen, S. G. F.; Thian, F. S.; Kobilka, T. S.; Choi, H.-J.; Kuhn, P.; Weis, W. I.; Kobilka, B. K.; Stevens, R. C. High-resolution crystal structure of an engineered human beta2-adrenergic G protein-coupled receptor. *Science*. **2007**, 318, 1258-65.

280 Manglik, A.; Kruse, A. C. Structural basis for G Protein-Coupled Receptor activation. *Biochemistry*. **2017**, 56, 5628-34.

281 Dror, R. O.; Arlow, D. H.; Maragakis, P.; Mildorf, T. J.; Pan, A. C.; Xu, H. Borhani, D. W.; Shaw, D. E. *Proc. Natl. Acad. Sci. U. S. A.* **2011**, 108, 18684-9.

282 Latorraca, N. R.; Venkatakrishnan, A. J.; Dror, R. O. GPCR Dynamics: Structures in Motion. *Chem. Rev.* **2017**, 117, 139-55.

283 Salas-Estrada, L.; Fiorillo, B.; Filizola, M. Metadynamics simulations leveraged by statistical analyses and artificial intelligence-based tools to inform the discovery of G protein-coupled receptor ligands. *Front. Endocrinol.* **2022**, 13, 1099715.

284 Fleetwood, O.; Matricon, P.; Carlsson, J.; Delemotte, L. Energy landscapes reveal agonist control of G protein-coupled receptor activation via microswitches. *Biochemistry*. **2020**, 59, 880-91.

285 Fleetwood, O.; Carlsson, J.; Delemotte, L. Identification of ligand-specific G protein-coupled receptor states and prediction of downstream efficacy via data-driven modeling. *Elife*. **2021**, 10, e60715.

286 Provasi, D.; Filizola, M. Putative active states of a prototypic G-protein-coupled receptor from biased molecular dynamics. *Biophys. J.* **2010**, 98, 2347-55.

287 Provasi, D.; Camacho Artacho, M.; Negri, A.; Mobarec, J. C.; Filizola, M. Ligand-induced modulation of the free-energy landscape of G protein-coupled receptors explored by adaptive biasing techniques. *PLoS Comput. Biol.* **2011**, 7, e1002193.

288 Meral, D.; Provasi, D., Filizola, M. An efficient strategy to estimate thermodynamics and kinetics of G protein-coupled receptor activation using metadynamics and maximum caliber. *J. Phys. Chem.* **2018**, 149, 224101.

289 Mattedi, G.; Acosta-Gutiérrez, S.; Clark, T.; Gervasio, F. L. A combined activation mechanism for the glucagon receptor. *Proc. Natl. Acad. Sci. U. S. A.* **2020**, 117, 15414-22.

---

290 Hauser, A. S.; Kooistra A. J.; Munk, C.; Heydenreich, F. M. ; Veprintsev, D. B. ; Bouvier, M. ; Babu, M. M. ; Gloriam, D. E. GPCR activation mechanisms across classes and macro/microscales. *Nat. Struct. Mol. Biol.* **2021**, 28, 879-88.

291 Nygaard, R.; Zou, Y. Z.; Dror, R. O.; Mildorf, T. J.; Arlow, D. H.; Manglik, A.; Pan, A. C.; Liu, C. W.; Fung, J. J.; Bokoch, M. P. The dynamic process of β_2-adrenergic receptor activation. *Cell.* **2013**, 152, 532-42.

292 Weis, W. W.; Kobilka, B. K. The molecular basis of G protein–coupled receptor activation. *Annu. Rev. Biochem.* **2018**, 87, 897-919.

293 Huang, W.; Manglik, A.; Venkatakrishnan, A. J.; Laeremans, T.; Feinberg, E. N.; Sanborn, A. L.; Kato, H. E.; Livingston, K. E.; Thorsen, T. S.; Kling, R. C. Structural insights into μ-opioid receptor activation. *Nature*. **2015**, 524, 315-21.

294 Yuan, S.; Filipek, S.; Palczewski, K.; Vogel, H. Activation of G-protein-coupled receptors correlates with the formation of a continuous internal water pathway. *Nat. Commun.* **2014**, 5, 4733.

295 Ibrahim, P.; Wifling, D.; Clark, T. Universal activation index for class A GPCRs. *J. Chem. Inf. Model.* **2019**, 59, 3938-45.

296 Ranganathan, A.; Dror, R. O.; Carlsson, J. Insights into the role of Asp79$^{2.50}$ in β_2 adrenergic receptor activation from molecular dynamics simulations. *Biochemistry*. **2014**, 53, 7283-96.

297 Mailman, R. B. GPCR functional selectivity has therapeutic impact. *Trends Pharmacol Sci.* **2007**, 28, 390-6.

298 *Schrödinger Release 2022-1: Glide 9.0*, Schrödinger, LLC, New York, NY, 2022.

299 Lu, C.; Wu, C.; Ghoreishi, D.; Chen, W.; Wang, L.; Damm, W.; Ross, G.; Dahlgren, M.; Russell, E.; Von Bargen, C.; Abel, R.; Friesner, R.; Harder, E.; OPLS4: Improving force field accuracy on challenging regimes of chemical space. *J. Chem. Theory Comput.* **2021**, 17, 4291-300.

300 Kolossváry, I.; Guida, W. C. Low-mode conformational search elucidated. Application to $C_{39}H_{80}$ and flexible docking of 9-deazaguanine inhibitors to PNP. *J. Comput. Chem.* **1999**, 20, 1671.

301 *Schrödinger Release 2022-1: MacroModel 13.1*, Schrödinger, LLC, New York, NY, 2022.

302 Piana, S.; Robustelli, P.; Tan, D; Chen, S.; Shaw, D. E. Development of a force field for the simulation of single-chain proteins and protein–protein complexes. *J. Chem. Theory Comput.* **2020**, 16, 4, 2494-507.

303 Piana, S.; Donchev, A. G.; Robustelli, P.; Shaw, D. E. Water dispersion interactions strongly influence simulated structural properties of disordered protein states. *J. Phys. Chem. B*, **2015**, 119, 5113-23.

304 *Schrödinger Release 2022-1: Jaguar 11.1*, Schrödinger, LLC, New York, NY, 2022.

305 Bussi, G.; Donadio, D.; Parrinello, M. Canonical sampling through velocity rescaling. *J. Chem. Phys.* **2007**, 126, 014101.

306 Bernetti, M.; Bussi, G. Pressure control using stochastic cell rescaling. *J. Chem. Phys.* **2020**, 153, 114107.

307 Daura, X.; Gademann, K.; Jaun, B.; Seebach, D.; van Gusteren, W. F.; Mark, A. E. Peptide folding: when simulations meets experiments. *Angew. Chem. Int. Ed.* **1999**, 38, 236-40.

308 Šali, A.; Blundell, T. L. Comparative protein modelling by satisfaction of spatial restraints. *J. Mol. Biol.* **1993**, 234, 779-815.

309 Fiser, A.; Do, R.K.; Šali, A. Modeling of loops in protein structures. *Protein Sci.* **2000**, 9, 1753-73.

310 Shen, M.; Šali, A. Statistical potential for assessment and prediction of protein structures. *Protein Sci.* **2006**, 15, 2507-24.

311 Sastry, M.G.; Adzhigirey, M.; Day, T.; Annabhimoju, R.; Sherman, W. Protein and ligand preparation: parameters, protocols, and influence on virtual screening enrichments. *J. Comput. Aided. Mol. Des.* **2013**, 27, 221-34.

312 *Schrödinger Release 2022-1: Prime 6.3*, Schrödinger, LLC, New York, NY, 2022.

313 Banks, J.L.; Beard, H.S.; Cao, Y.; Cho, A.E.; Damm, W.; Farid, R.; Felts, A.K.; Halgren, T.A.; Mainz, D.T.; Maple, J.R.; Murphy, R.; Philipp, D.M.; Repasky, M.P.; Zhang, L.Y.; Berne, B.J.; Friesner, R.A.; Gallicchio, E.; Levy. R.M. Integrated Modeling Program, Applied Chemical Theory (IMPACT). *J. Comp. Chem.* **2005**, 26, 1752

314 *Schrödinger Release 2022-1: Impact 9.0*, Schrödinger, LLC, New York, NY, 2022.